NASA/TP-2019-220302

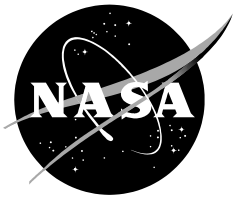

Haystack Ultra-Wideband Satellite Imaging Radar Measurements of the Orbital Debris Environment: 2014-2017

Orbital Debris Program Office

J. Murray
C. Blackwell
J. Gaynor
T. Kennedy

National Aeronautics and
Space Administration

Lyndon B. Johnson Space Center
Houston, Texas 77058

July 2019

NASA STI Program Office ... in Profile

Since its founding, NASA has been dedicated to the advancement of aeronautics and space science. The NASA scientific and technical information (STI) program plays a key part in helping NASA maintain this important role.

The NASA STI program operates under the auspices of the Agency Chief Information Officer. It collects, organizes, provides for archiving, and disseminates NASA's STI. The NASA STI program provides access to the NTRS Registered and its public interface, the NASA Technical Report Server, thus providing one of the largest collections of aeronautical and space science STI in the world. Results are published in both non-NASA channels and by NASA in the NASA STI Report Series, which includes the following report types:

- TECHNICAL PUBLICATION. Reports of completed research or a major significant phase of research that present the results of NASA Programs and include extensive data or theoretical analysis. Includes compilations of significant scientific and technical data and information deemed to be of continuing reference value. NASA counter-part of peer-reviewed formal professional papers but has less stringent limitations on manuscript length and extent of graphic presentations.

- TECHNICAL MEMORANDUM. Scientific and technical findings that are preliminary or of specialized interest, e.g., quick release reports, working papers, and bibliographies that contain minimal annotation. Does not contain extensive analysis.

- CONTRACTOR REPORT. Scientific and technical findings by NASA-sponsored contractors and grantees.

- CONFERENCE PUBLICATION. Collected papers from scientific and technical conferences, symposia, seminars, or other meetings sponsored or co-sponsored by NASA.

- SPECIAL PUBLICATION. Scientific, technical, or historical information from NASA programs, projects, and missions, often concerned with subjects having substantial public interest.

- TECHNICAL TRANSLATION. English-language translations of foreign scientific and technical material pertinent to NASA's mission.

Specialized services also include organizing and publishing research results, distributing specialized research announcements and feeds, providing information desk and personal search support, and enabling data exchange services.

For more information about the NASA STI program, see the following:

- Access the NASA STI program home page at *http://www.sti.nasa.gov*

- E-mail your question to help@sti.nasa.gov

- Phone the NASA STI Information Desk at 757-864-9658

- Write to:
  NASA STI Information Desk
  Mail Stop 148
  NASA Langley Research Center
  Hampton, VA 23681-2199

NASA/TP-2019-220302

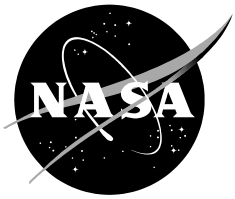

Haystack Ultra-Wideband Satellite Imaging Radar Measurements of the Orbital Debris Environment: 2014-2017

Orbital Debris Program Office

J. Murray
C. Blackwell
J. Gaynor
T. Kennedy

National Aeronautics and
Space Administration

Lyndon B. Johnson Space Center
Houston, Texas 77058

July 2019

ACKNOWLEDGEMENTS

The authors would like to thank Phillip Anz-Meador and Eugene Stansbury for a very thorough technical review of this report. We would like to thank Debra Shoots for her editing contributions. Finally, the authors would like to thank Melissa Ward, Rossina Miller, Quanette Juarez, and Brent Buckalew for their contributions to the data processing and data quality control efforts.

Available from:

NASA STI Program
Mail Stop 148
NASA Langley Research Center
Hampton, VA 23681-2199

National Technical Information Service
5285 Port Royal Road
Springfield, VA 22161

This report is also available in electronic form at http://www.sti.nasa.gov/ and http://ntrs.nasa.

TABLE OF CONTENTS

SECTION **PAGE**

FIGURES

FIGURE **PAGE**

TABLES

TABLE **PAGE**

Acronyms

CLDT	Calibrated Lincoln Data Tape
CW	Continuous Wave
dB	Decibels
dBsm	One over square meters measured in decibels
DRADIS	Debris Radar Automated Data Inspection System
EL	Elevation
FFT	Fast Fourier Transform
FSPL	Free Space Path Loss
FY	Fiscal Year
GUI	Graphical User Interface
HUSIR	Haystack Ultra-Wideband Satellite Imaging Radar
I	In-phase
IF	Intermediate Frequency
ISS	International Space Station
JSC	Johnson Space Center
LEO	Low Earth Orbit
MIT/LL	Massachusetts Institute of Technology/Lincoln Laboratory
NaK	Sodium-Potassium
NASA	National Aeronautics and Space Administration
ODAS	Orbital Debris Analysis System
ODPO	Orbital Debris Program Office
OP	Orthogonal Polarization
PACS	Processing and Control System
POPACS	Polar Orbiting Passive Calibration Spheres
PP	Principal Polarization
Q	Quadrature, Quadrature-phase
RCS	Radar Cross Section (usually in dBsm)
RDI	Range Doppler Image
RFI	Radio Frequency Interference
RORSAT	Radar Ocean Reconnaissance SATellites
RTDR	Real Time Data Record
SEM	Size Estimation Model
SENS	Sensitivity File

SSEM	Statistical Size Estimation Model
SNR	Signal-to-Noise Ratio
SSN	U.S. Space Surveillance Network
TWT	Traveling-wave Tube
WFC	Waveform Code
WGS	World Geodetic System
σ	Sigma

(This page intentionally left blank)

1.0 Introduction

1.1. BACKGROUND

Since the founding of the NASA Orbital Debris Program Office (ODPO) in 1979, the knowledge that orbital debris poses a risk to operational satellites and human spaceflight has been publically available. Services that rely on satellite-based technology such as communications, internet, navigation, and weather forecasting, to name a few, are ubiquitous in modern society. The International Space Station (ISS) has been continuously inhabited by a crew of up to six astronauts since November 2000 and makes, on average, approximately one debris avoidance maneuver per year to avoid objects that are large enough to be tracked by ground-based radars [1]. This places an increased need for understanding the current status of the debris environment (measurements), for the ability to predict the future environment (modeling), and for understanding risk factors for debris creating events (mitigation). For NASA, the measurements, modeling, and mitigation aspects of orbital debris are led by the NASA ODPO at the Johnson Space Center (JSC) in Houston, Texas.

1.2. SCOPE

This report summarizes radar measurement data from the Haystack Ultra-wideband Satellite Imaging Radar (HUSIR) operated by the Massachusetts Institute of Technology Lincoln Laboratory (MIT/LL) and provided to the NASA ODPO. The time period covered by this report includes data collected during the U.S. government fiscal year (FY) 2014 through FY2017. The U.S. government FY begins on 1 October and lasts through 30 September of a given year (*i.e.*, FY2014 lasts from 1 October 1 2013 through 30 September 30 2014). At this report's release, processed data was unavailable from the Haystack Auxiliary Radar (HAX) due to errors in the calibration data for the radar and limited transmit power; a decision was made by NASA not to collect low-power HAX radar data. This is being resolved by NASA and MIT/LL and data collected during this time period will be released in a separate report.

1.3. OVERVIEW

The ODPO relies primarily on ground-based radar measurements to characterize the distribution of small debris in low Earth orbit (LEO). MIT/LL has been collecting radar measurements for the NASA ODPO for nearly three decades under memorandums of agreement with the U.S. Department of Defense. Beginning with the Haystack radar in October 1990 and supplemented by the HAX radar in March 1994, the NASA ODPO nominally receives 1000 hours of data collected per fiscal year. Of those hours, approximately 600 are collected by HUSIR and 400 by HAX. The data is collected in a staring mode for statistical sampling purposes and no effort is made to track the objects detected. The HUSIR and HAX radars generate very narrow beams, which although extremely sensitive, only observe a small volume of space at a given time. Due to the sensitivity of these radars, NASA ODPO is able to sample the orbital debris environment down to approximately 3 cm with HAX and 5 mm with HUSIR to an altitude of up to 1000 km. NASA ODPO uses data collected by HUSIR and HAX to characterize the orbital debris environment in altitude, inclination, and size for a large fraction of LEO (altitude < 2000 km) and orbits traversing LEO.

This report includes an overview of the radar systems, radar signal processing, radar measurements, and environment characterization.

2.0 Radar System Overview

The HUSIR and HAX radars are high-powered, sensitive sensors used for a variety of applications including space situational awareness. Sensors of this caliber are necessary for orbital debris radar observations due to the small size of the orbital debris of interest – less than 10 cm and often less than 1 cm for HUSIR – and the short duration of a debris detection while in beam-park mode. This section provides an overview of these radar systems, including information on the upgrade from Haystack to HUSIR that was completed prior to collection of the first data sets summarized in this report.

The HUSIR and HAX radars are of Cassegrain configuration. Located in Tyngsborough, Massachusetts, each radar has a Cassegrain focus at the following coordinates [2]:

Table 2-1: HUSIR and HAX Location with Respect to the 1984 World Geodetic System (WGS 84) Earth Model

	Latitude	Longitude	Elevation
HUSIR	42.623287° N	288.511846° E	115.69 m
HAX	42.622835° N	288.511709° E	101.11 m

The HUSIR radar consists of a 36.6 meter-diameter parabolic reflector transmitting right-handed circularly-polarized waveforms and receiving both right- and left-handed circularly-polarized returns – representing the orthogonal polarization (OP) and principal polarization (PP) channels, respectively, of the radar. For orbital debris measurements, the radar transmits a pulsed continuous wave (CW) signal at X-band with a center frequency of 10 GHz. Additional details of the radar waveforms will be discussed in section 3. HUSIR has a monopulse feed horn capable of determining object position in the beam with a single pulse using amplitude comparison monopulse techniques. While traditionally used for maintaining tracked objects on boresight, instead the NASA ODPO uses monopulse to measure an object's path through the beam while the radar remains stationary (beam-park mode). HUSIR has a two-sided half-power, 3 decibel (dB)-beamwidth of 0.058°. Shown in Figure 2-1 is a block diagram of the HUSIR transmit and receive system, which is useful in understanding how the raw in-phase (I) and quadrature (Q) components of the received signal are obtained, as well as how test signals may be injected for calibration purposes.

Starting in 2010, the Haystack radar underwent a significant upgrade to incorporate a W-band transmitter and receiver. The upgrade also included a new radome, quadrupod, backstructure, azimuth bearings, and other items to enable Haystack's operation as a world-class sensor for years to come. Additional in-depth information regarding the upgrade may be found in [3].

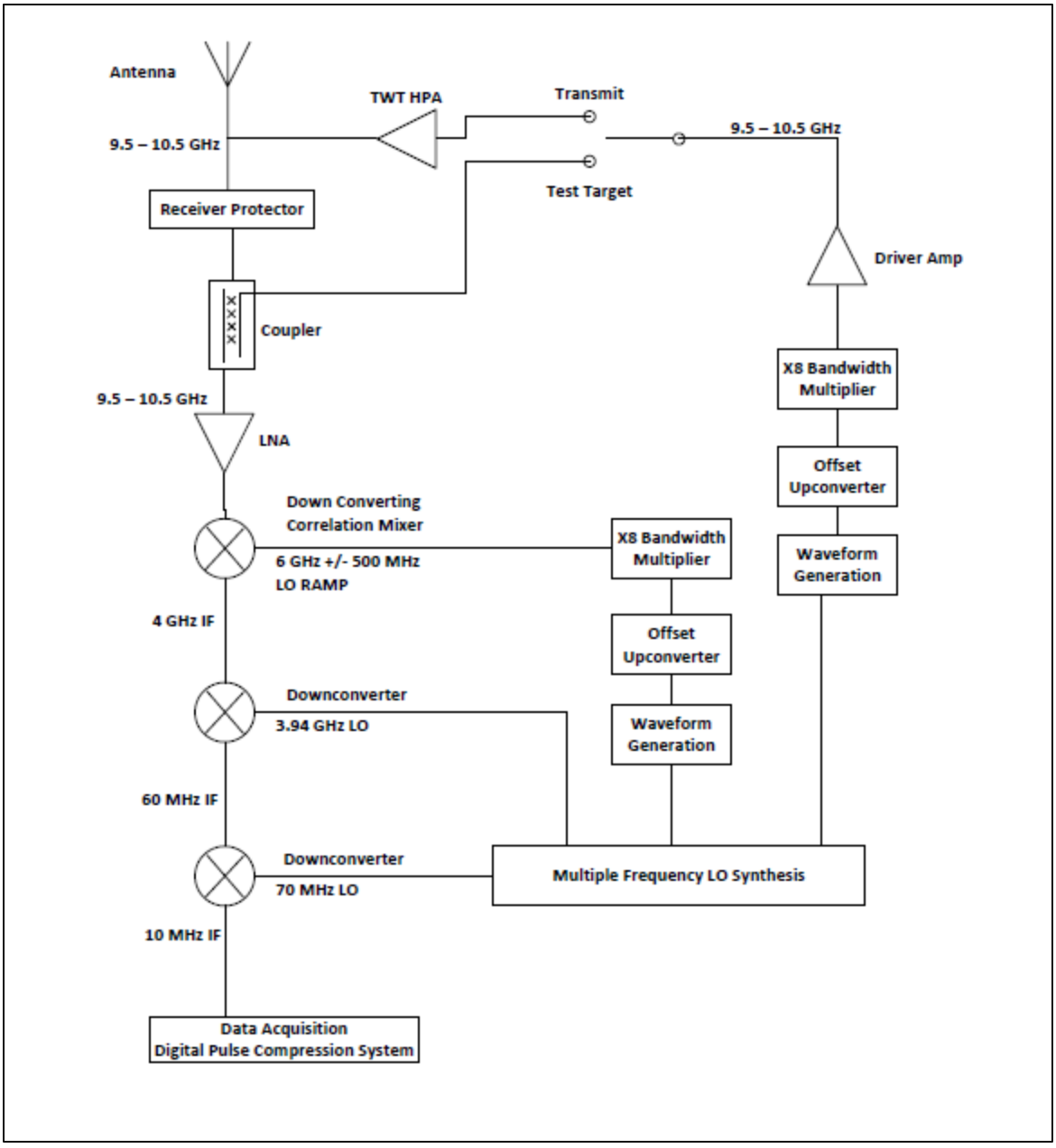

Figure 2-1. Block diagram of the HUSIR Transmit and Receive system.

The HAX radar consists of a 12.2 meter-diameter parabolic reflector transmitting right-handed circularly-polarized waveforms and receiving both right and left-handed circularly-polarized returns – comprising the OP and PP channels respectively. For orbital debris measurements, the radar transmits a pulsed CW signal at Ku-band with a center frequency of 16.7 GHz. HAX also has a monopulse feed horn, similar to HUSIR, and uses amplitude comparison monopulse techniques for measuring position in the beam. HAX has a much smaller antenna diameter than HUSIR, which in spite of a higher center frequency, leads to a wider two-sided, half-power beamwidth of 0.10°. This wider beam width provides a larger collection area for debris flux measurements and hence, better counting statistics for larger debris objects. The loss of sensitivity with HAX relative to HUSIR is offset by the increased collection area from the wider

beam and different operating frequency, making HAX a complementary sensor to HUSIR for orbital debris measurements. A block diagram of the HAX transmit and receive system is shown in Figure 2-2. Note that aside from the frequency band differences, operation is similar to HUSIR.

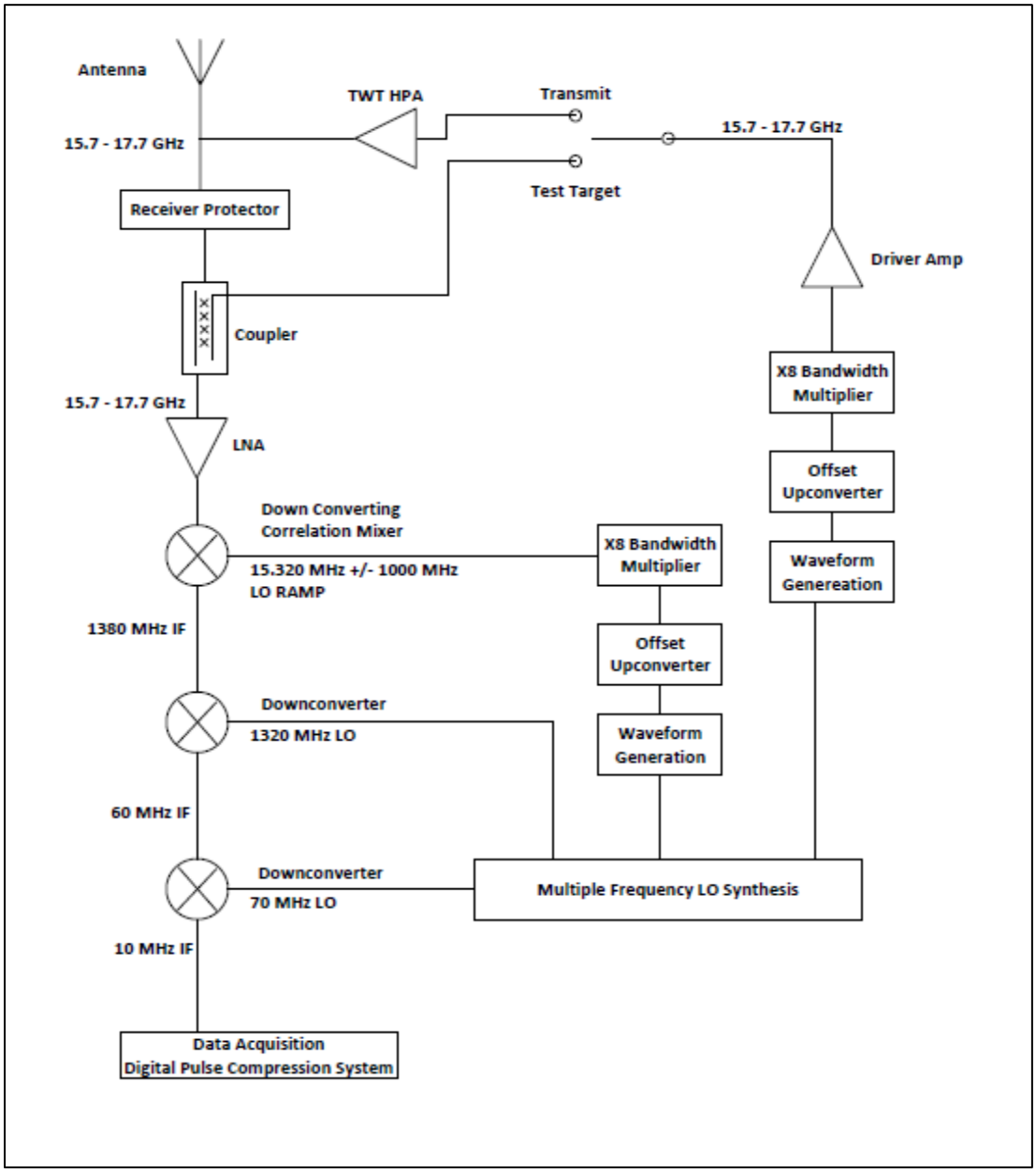

Figure 2-2. Block diagram of the HAX transmit and receive system.

Table 2-2 contains the radar debris mode – waveform code 4 – operating parameters for HUSIR and HAX. Other waveforms of interest are waveform codes 1 and 11, which are used to calibrate the radars. Additional details are in section 3.0.

Table 2-2: Radar Debris Mode Operating Parameters

Operating Parameter	HUSIR	HAX
Peak Power (kW)	250	50
Transmitter Frequency (GHz)	10.0	16.7
Transmitter Wavelength (cm)	3.0	1.8
Antenna Diameter (m)	36.6	12.2
Antenna Half-power beam width (deg)	0.058	0.10
Antenna Gain (dB)	67.23	63.64
System Temperature (K)	186	161
Total System Losses (dB)	3.9	4.5
Waveform Code	4	4
Range Gates	16	16
Intermediate Frequency Bandwidth (KHz)	1250	1250
Independent Range/Doppler Samples	15158	15158
FFT Size	16384	16384
Number of non-coherently integrated pulses used for detection	16	16
Pulse Width (msec)	1.6384	1.6384
Receive Window (msec)	12.1264	12.1264
Pulse repetition frequency (Hz)	60	60
Nominal Sensitivity (dB)	59.2	40.6
Average Power (kW)	24.6	4.9
Doppler Extent (km/s)	±7.5	±4.5

The 16 range gates, referenced in Table 2-2, refer to the number of range gates used in the initial detections performed by MIT/LL using their real time processor. A discussion of moving NASA ODPO processing from 16 to 32 range gates and motivations for the change are presented in section 3.5.

2.1. RADAR PERFORMANCE

One way to assess radar performance over time is to calculate the sensitivity. The ODPO and MIT/LL define sensitivity as the single pulse signal-to-noise ratio (SNR) for an object with a 1 square meter-radar cross section (RCS) at 1000 km slant range. Typically, all variables of the radar range equation are held constant in this calculation, since they typically do not change, except for the transmit power. The nominal values are in Table 2-2. An example calculation, which is useful in establishing the lower bound for an object's RCS – and hence size estimate for detected orbital debris – that may be observed with HUSIR, is described below:

$$\begin{aligned} Sensitivity\ (dB) &= SNR(R = 1000km, \sigma = 0dBsm)(dB) \\ &= 10\log_{10}\left(\frac{P_t G^2 \lambda^2 \sigma}{(4\pi)^3 R^4 k_B T\ B\ L}\right) \\ &= P_t(dBW) + 5.2264\ dB \end{aligned} \qquad 2\text{-}1$$

In the final expression in Equation 2-1, transmit power P_t is expressed in units of decibel watt (dBW), and all other variables have been reduced to a constant using the nominal operating parameters presented in Table 2-2. Using Equation 2-1 and a nominal transmitter power of 250 kW, HUSIR has a sensitivity of 59.2 dB. Figure 2-3 illustrates the sensitivity history of HUSIR from FY2014 through FY2017. There are several time periods where sensitivity was lost due to issues with the traveling-wave tube (TWT) transmitters, which will be discussed later in this section.

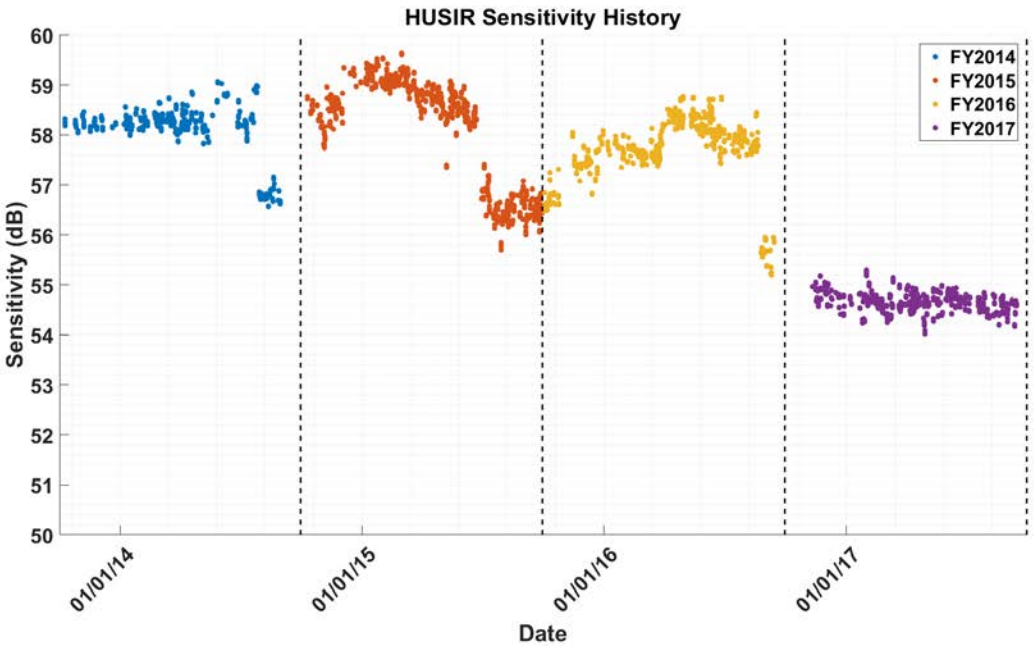

Figure 2-3. Sensitivity history for HUSIR from the beginning of FY2014 through the end of FY2017.

The vertical dashed lines represent the boundaries between U.S. Government fiscal years (FYs). For the time period covered in this report, HAX was only operational for orbital debris data collection during FY2014. This was due to an issue with its TWT amplifiers, which necessitated that HAX operate at a power level too low to have the sensitivity required to make useful orbital debris measurements. Figure 2-4 illustrates the sensitivity history of HAX during FY2014.

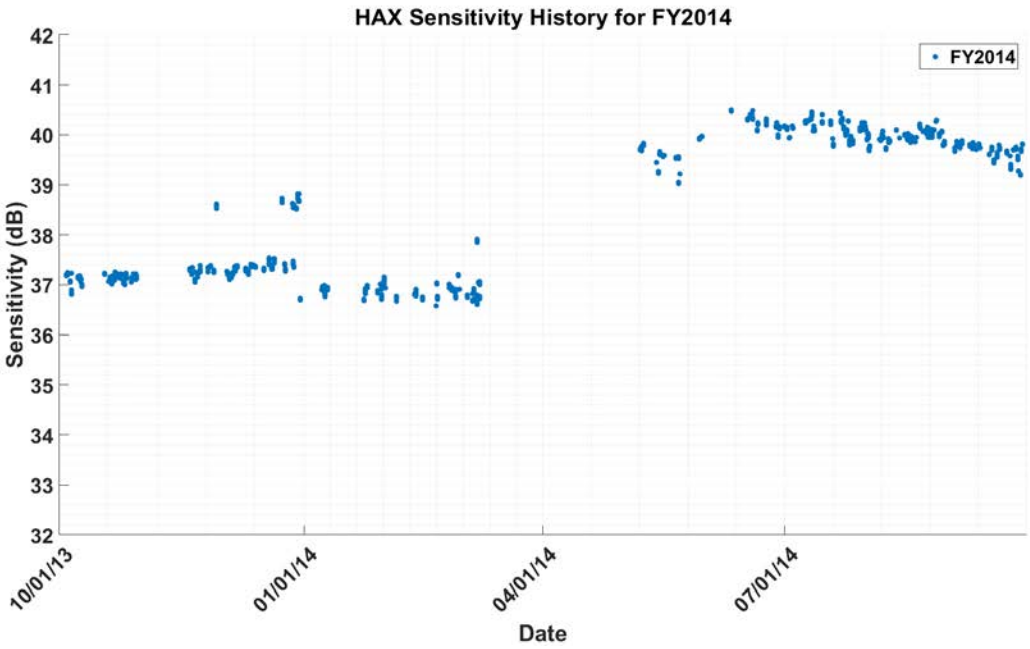

Figure 2-4. HAX Sensitivity history for FY2014.

The low transmit power issue for HAX was present during most of FY2014 as well, as shown in Figure 2-6. In June 2014, a refurbished tube was installed bringing the radar close to nominal operating sensitivity. This tube, however, experienced a failure in FY2015 and HAX has ceased orbital debris data collection activities until such time as the transmit power can be returned to a nominal status.

As seen in Equation 2-1, the sensitivity is assumed to be a function of transmit power, with all other variables being held constant. As a regular measure of radar health, MIT/LL delivers a sensitivity (SENS) file derived from data regularly collected on known calibration spheres. Among other things, the SENS file reports the transmitter power. Plots of transmit power versus time can be seen in Figures 2-5 and 2-6 and serve as the foundation for the sensitivity, maximum detectable range, and minimum-detectable size plots that follow.

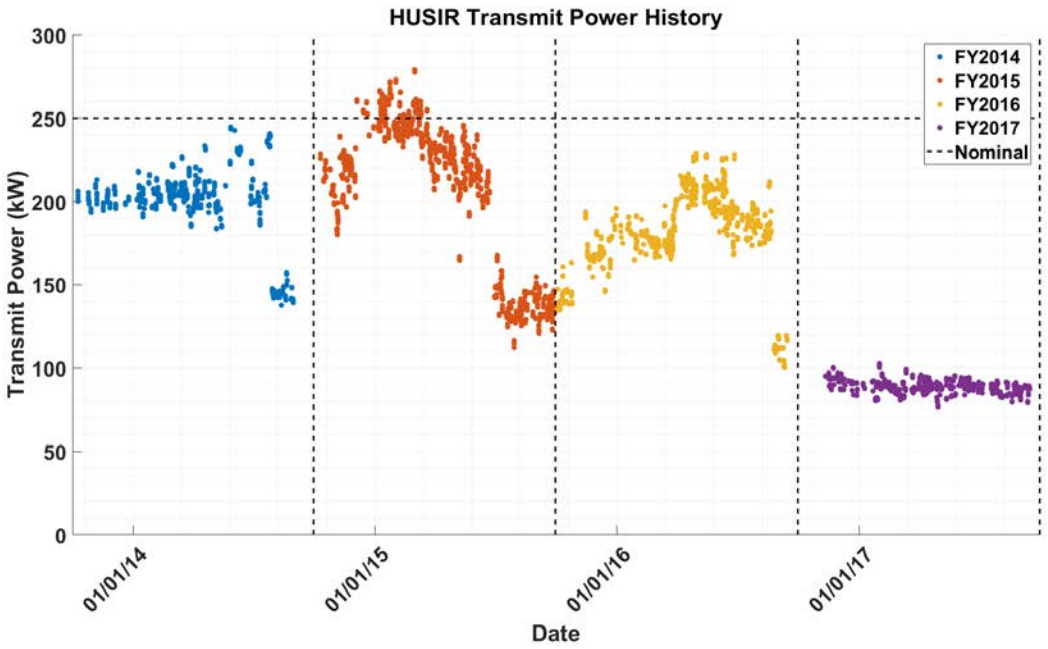

Figure 2-5. Transmit power history for HUSIR from the beginning of FY2014 through the end of FY2017. The vertical dashed lines represent the boundaries between U.S. Government FYs. The horizontal dashed line represents the nominal HUSIR transmit power.

The data gaps in Figure 2-5, around the transition between FYs (denoted by the vertical, black-dashed line), correspond to periods where the HUSIR Radio Frequency box is taken offline for maintenance. Sharp drops in transmit power, like the one seen above shortly before the end of FY2014, are a result of TWT failures. August 2016 saw the radar go from four operating TWTs to three and approximately a month later, another TWT failed, leading to a two-TWT configuration. For the entirety of FY2017, the radar operated at just under half power with two functioning TWTs.

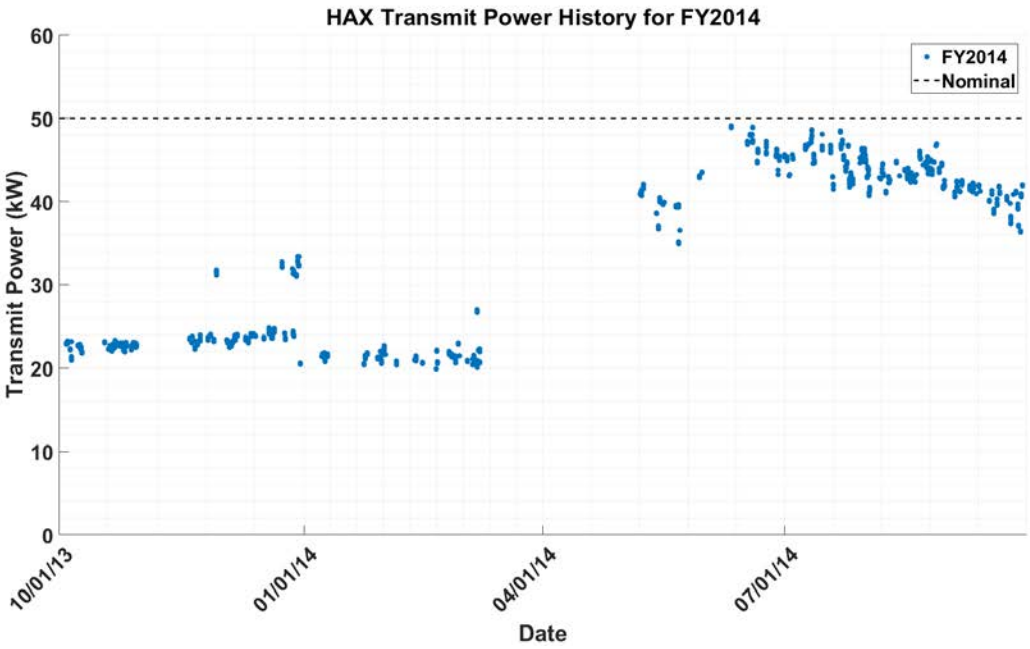

Figure 2-6. HAX Transmit Power history for FY2014. The horizontal dashed line represents the nominal HAX transmit power.

Another way to interpret the power history is to determine a maximum detectable range for an object of a given size. The size or characteristic length of an object can be translated to and from RCS via the NASA Size Estimation Model (SEM) [4], then input into the radar range equation to determine at what range the object would have sufficient SNR to be detected. Figure 2-7 presents the maximum detectable range of both a 1 cm- and a 1 mm-sized particle for HUSIR from FY2014 through FY2017. Figure 2-8 presents the maximum detectable range of both a 1 cm- and a 2 cm-sized particle for HAX during FY2014.

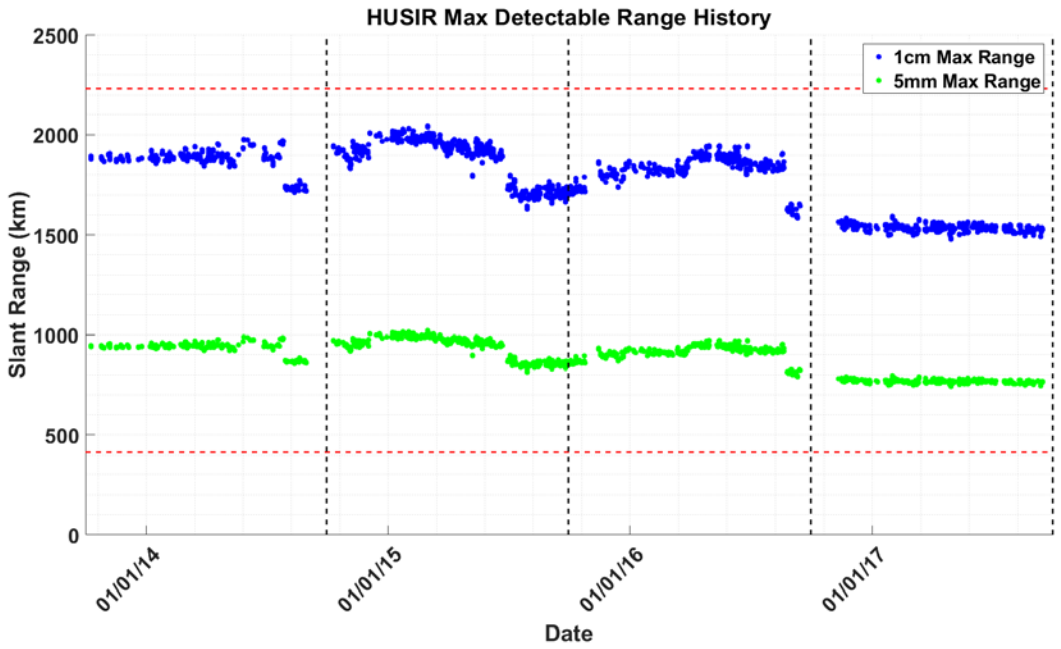

Figure 2-7. Maximum Detectable Range History for HUSIR showing the maximum detectable range for a 1 cm and a 5 mm object from FY2014 through FY2017. The vertical, dashed lines represent the boundaries between U.S. Government FYs. The horizontal dashed lines represent the range window boundaries of HUSIR.

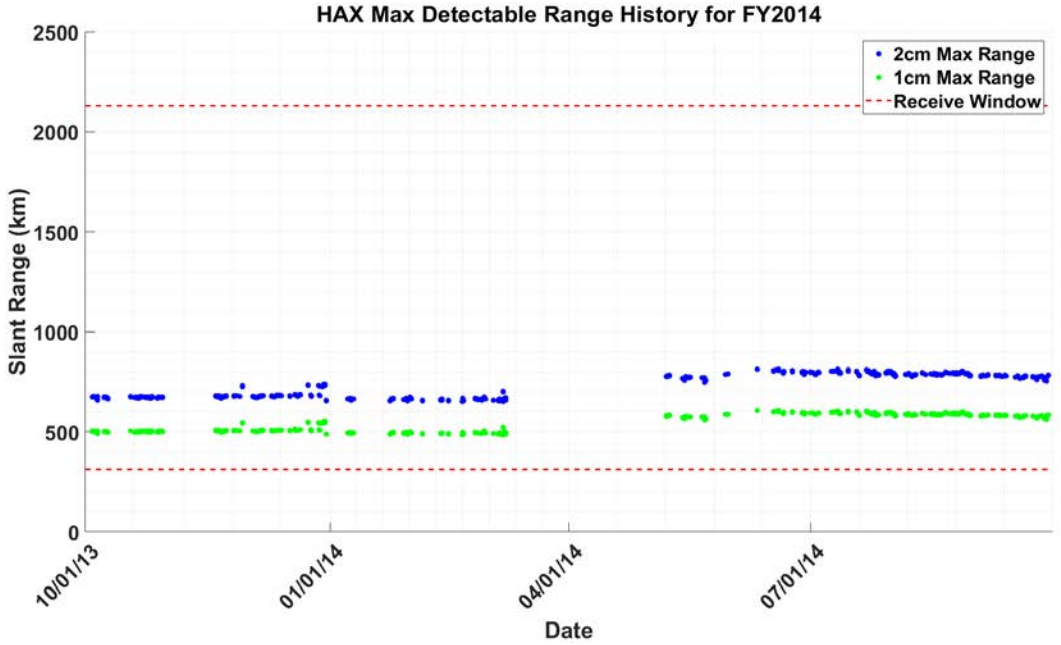

Figure 2-8. HAX Maximum Detectable Range History for FY2014. The horizontal dashed lines represent the range window boundaries of HAX.

Similarly, we can calculate a minimum detectable RCS based on the radar's operating parameters, an SNR threshold, and a given range (altitude). The minimum-detectable size plots in Figures 2-9 and 2-10 take that minimum detectable RCS and use the NASA SEM to convert it to a characteristic size. This allows us to determine an approximate limiting size for our population at particular altitudes of interest. In the plots in Figures 2-9 and 2-10 we calculate the theoretical, minimum detectable size for the ISS altitude, A-train constellation altitude, 1000 km altitude, and at the maximum range for the radar's receive window.

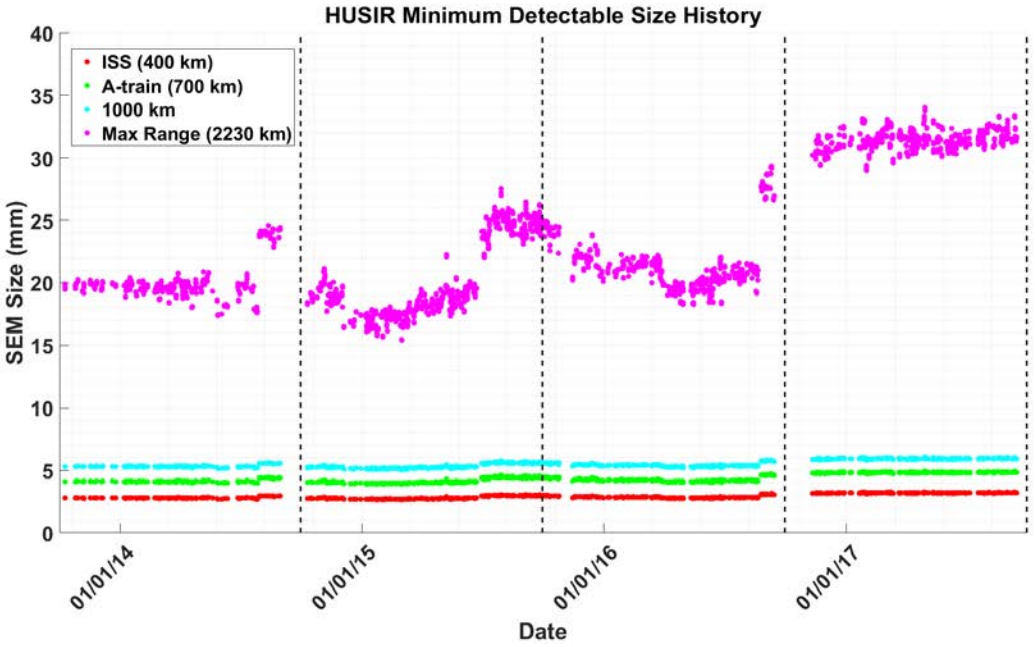

Figure 2-9. Minimum-Detectable Size History for HUSIR from FY2014 through FY2017. The vertical, dashed lines represent the boundaries between U.S. Government FYs.

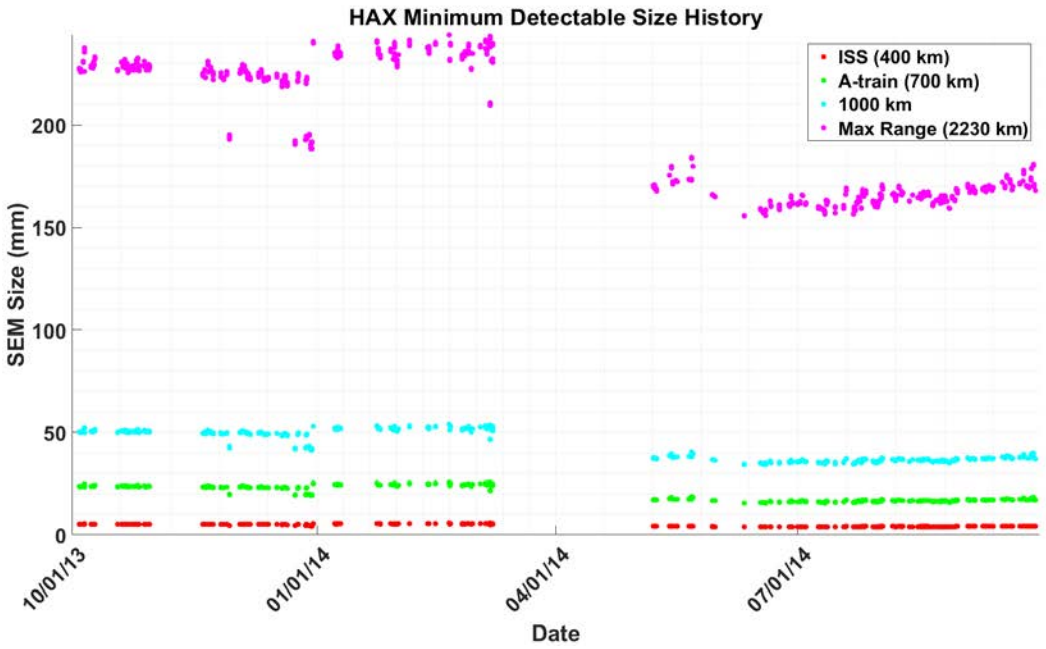

Figure 2-10. Minimum Detectable Size History for FY2014.

Notice in the minimum-detectable size plot in Figure 2-10 that at the maximum range extent of the receive window, HAX can only detect down to approximately 20 cm in characteristic size. The publicly available U.S. Space Surveillance Network (SSN) Satellite Catalog has been estimated to be complete down to approximately 20 cm in characteristic size in LEO and contains objects as small as approximately 10 cm. Figure 2-11 presents the cumulative distribution of cataloged objects in LEO (orbital period < 127.2 minutes). The diameter estimates are generated by converting the RCS time histories of the objects, provided by the Combined Space Operations Center, into size histories using the NASA SEM and calculating either the mean or median of the resulting distribution. The resulting cumulative size curves appear to be complete down to approximately 12 cm. This result led ODPO to cease collecting orbital debris radar data using HAX until it could be returned to nominal transmit power.

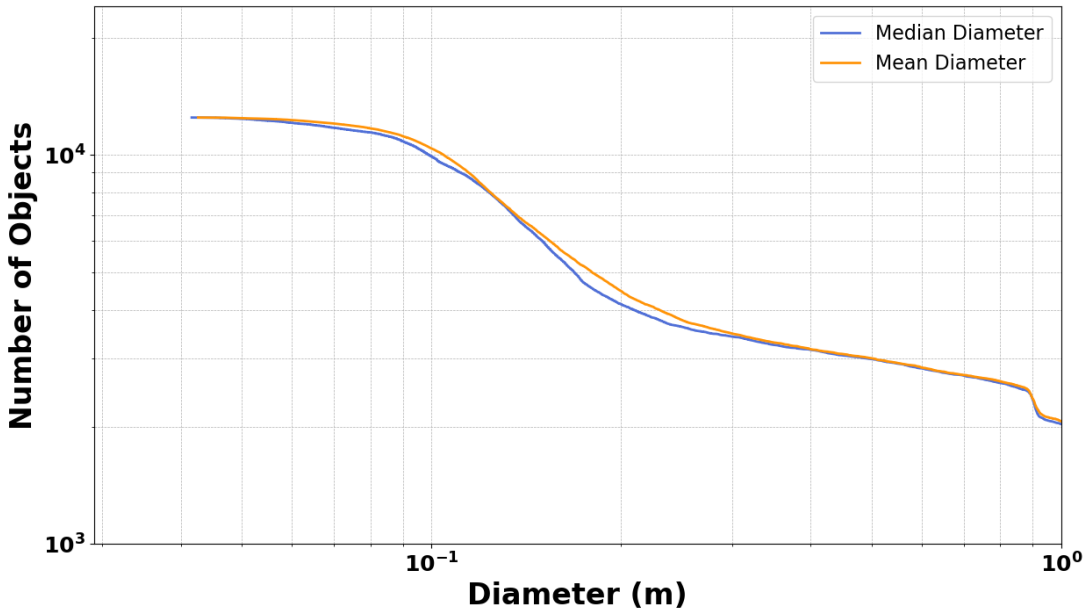

Figure 2-11. Cumulative Number of Objects in LEO (Orbital Period < 127.2 minutes). Launch and Reentry cutoff – 1 January 2019.

3.0 Radar Processing and Data Collection

For orbital debris radar data collection, both the HUSIR and HAX radars operate in a "beam-park" mode in which the radar antenna is pointed at a fixed elevation and azimuth, allowing the debris environment to randomly pass through the radar beam. This provides a fixed detection volume that simplifies calculations of the debris flux, or number of objects detected per unit area, per unit time. The tradeoff of the beam-park mode is that it limits precise measurement of a given object's orbital parameters, due to the short observation time for each object.

Typically, orbital debris radar data is collected in one of three staring geometries. This data, approximately, consists of: 1) 75° elevation, due East (75E), two-thirds; 2) 20° elevation, due South (20S), one-sixth; and 3) 10° elevation, due South (10S), the remaining one-sixth of the data collected. On occasion, special data collection campaigns are requested to observe objects of interest or breakup events. By staring just off-zenith, the 75E staring geometry allows the radar to measure Doppler shifts that give meaningful orbital information for orbital inclinations between approximately 40° inclination and 140° inclination – assuming a circular orbit. The high-elevation angle of the 75E staring geometry also minimizes atmospheric attenuation, allowing the radar to detect very small debris objects in orbit. The south-staring geometries (20S and 10S) allow the radar to see lower orbital inclinations down to approximately 20° inclination – again assuming a circular orbit.

However, the shallow elevation angle of these staring geometries suffers from decreased sensitivity due to increased slant range and atmospheric attenuation for a given altitude. A

breakdown of the individual contributions of free space path loss (FSPL) and atmospheric attenuation, assuming clear skies and a standard altitude of 1000 km, are shown in Table 3-1.

Table 3-1: Estimated Losses Associated with Staring Geometries

Pointing	Altitude	Slant Range	FSPL (relative to 75E)	Atmospheric Loss
75E	1000 km	1030 km	0.0 dB	0.53 dB
20S	1000 km	2120 km	12.54 dB	1.68 dB
10S	1000 km	2760 km	17.12 dB	3.96 dB

The atmospheric attenuation estimates were calculated using recommendations found in [5].

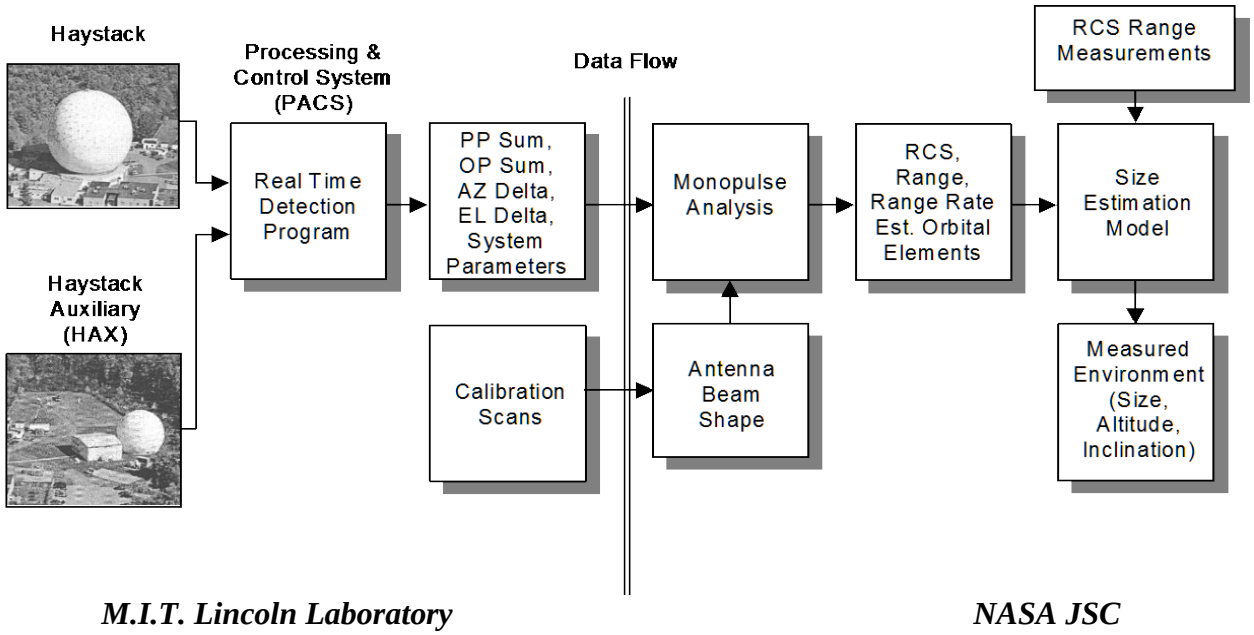

Figure 3-1. An overview of the data collection and analysis.

The radar produces six channels as outputs from the monopulse receiver network; these are the PP sum, OP sum, PP traverse difference, PP elevation difference, OP traverse difference, and OP elevation difference channels. The OP traverse and elevation difference channels are terminated at this point under the current configuration. Further processing demodulates the signal and develops digital in-phase (I) and quadrature-phase (Q) signals. Historically, MIT/LL has post-processed this data generating 16 range gates with 2048 samples in each gate and an approximate 40% overlap between gates. The data is Fast Fourier Transformed (FFT) into the frequency domain and recorded to a file for transfer to JSC. This format, referred to as the Calibrated Lincoln Data Tape or CLDT, is a special format provided to the ODPO by MIT/LL. However, due to recent upgrades to the signal processing software used by the ODPO (described later in this report), it is now possible to take the raw 15158 time samples for each channel and perform the range-gate processing at NASA JSC. This format, with data recorded in the time domain, is

referred to as Real Time Data Record or RTDR and is the standard data file provided by MIT/LL to its customers. In December 2017, MIT/LL ceased delivering CLDT files to NASA and will only deliver orbital debris radar data in RTDR format.

To avoid recording and transferring hours of radar I and Q data without any potential valid detections in it, MIT/LL operates a Processing and Control System (PACS) onsite that is programmed to record data in a buffer, or snippets of data, which are saved only when the integrated SNR exceeds a predetermined threshold. As long as the threshold is exceeded, the buffer will continue to record pulses to memory for transfer to the ODPO. In addition, several pulses from before and after the threshold was exceeded are recorded to minimize the loss of useful data and define the noise background. An example of how these snippets of data appear during processing can be seen below in Figure 3-2. The threshold for recording data at MIT/LL intentionally is set lower than in subsequent processing at JSC. This leads to a higher false alarm rate but more importantly, a higher probability of detection for low-SNR debris detections. The higher false alarm rate is mitigated in the signal processing performed at JSC using a higher SNR threshold requirement.

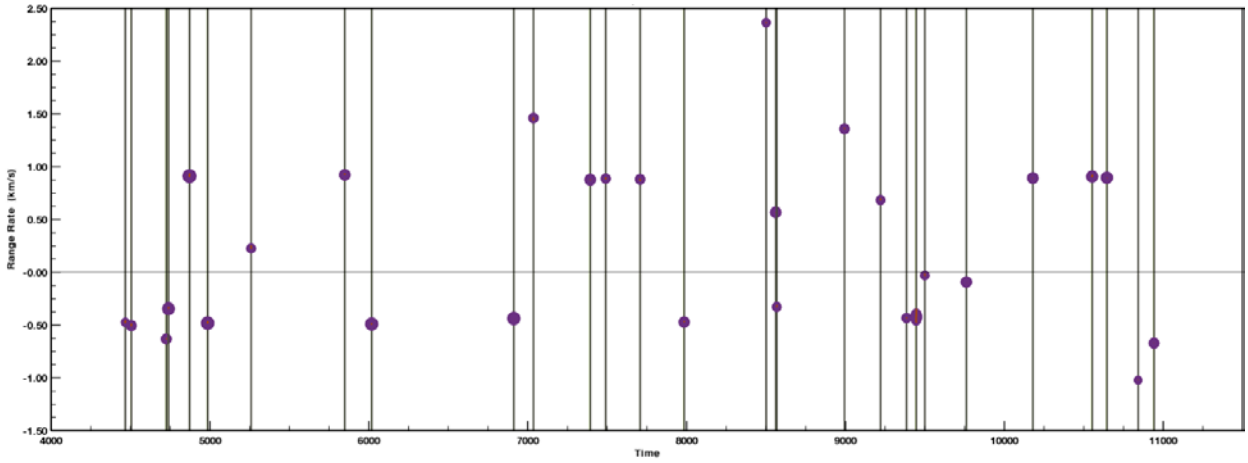

Figure 3-2. DRADIS screenshot of a detection map for an example HUSIR orbital debris file. Each vertical line represents a “snippet” of pulses that were dumped from the data buffer upon exceeding a specified threshold. The x-axis is coordinated universal time in seconds and the y-axis is Range-Rate in km/s. The circles represent where in Doppler space and time the detection was identified. The circles’ sizes are proportional to RCS.

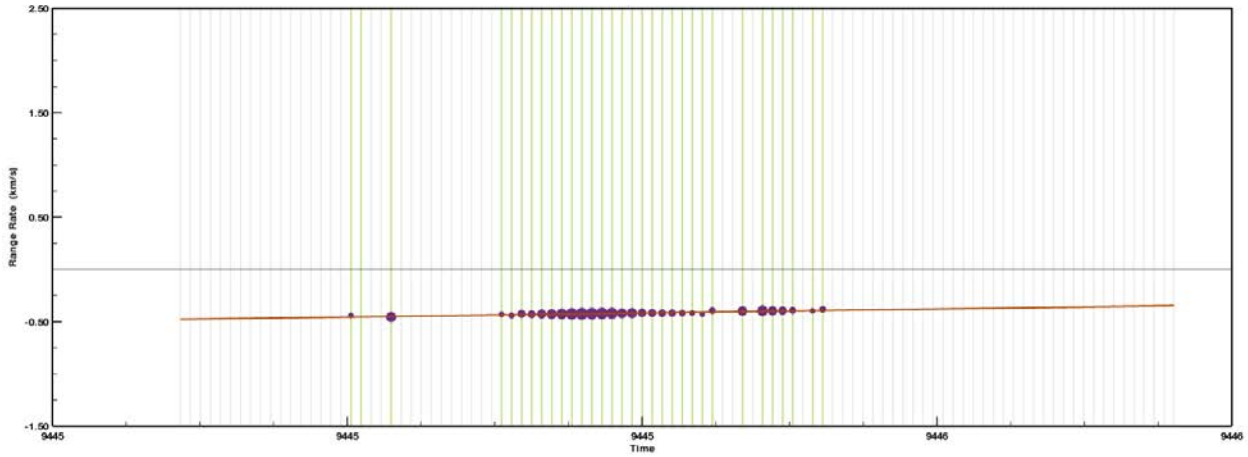

Figure 3-3. DRADIS screenshot of a zoomed in view from the detection map in Figure 3-2 showing a snippet of pulses. Each dot indicates a pulse whose SNR exceeded the detection threshold. The grayed out pulses were recorded to file but only contain noise.

3.1. RADAR SIGNAL PROCESSING AT JSC

Starting in 2015, the NASA ODPO began developing a new signal processing software to replace the legacy Orbital Debris Analysis System (ODAS) that had been the office workhorse for over two decades. The NASA ODPO contracted with Brilligent Solutions, Inc. and Sidlux Systems, LLC to develop the successor to ODAS known as the Debris Radar Automated Data Inspection System (DRADIS). In February of 2018, DRADIS (v1.2.5) achieved initial operating capability and was used to process the data presented in this report.

DRADIS was designed to make use of modern programming techniques, advances in radar signal processing, and the increased computing power afforded by today's modern computers. DRADIS implementations of several signal processing paradigms, which were not present in ODAS, result in higher quality datasets for this report. As of report publication, DRADIS is undergoing development of additional capabilities and progressing towards full operating capability – defined as having all of the original ODAS software capabilities plus increased flexibility in signal processing.

With this flexibility, the user can specify various signal processing parameters via a Graphical User Interface (GUI), as well as execute batch runs of multiple files in sequence. DRADIS also allows the user to process and visualize both spiral scan calibration files and noise calibration files; these are discussed later in this section. The table below lists the relevant signal processing parameters and the values used for the data presented in this report.

Table 3-2: DRADIS Signal Processing Parameters

Processing Parameter	Value
Range Doppler Image	
FFT Size	Zero-padded to 16384 samples
Observation Length	2048 samples
Number of Range Gates	32
Weighting	None/Rectangle
Detection	
Detector Type	Non-coherent Integration
Detection Channel	PP
Number of pulses integrated	16
Detection SNR Threshold	5.65 dB
Monopulse Threshold	11 dB
FFT Peak Interpolation	False
Measurement	
Measurement FFT Size	Zero-padded to 16384 samples
FFT Peak Interpolation	True
Monopulse Mode†	Clamped (±1)
Matched Filter Least Squares Fit	False
Use Integrated Range	True
Validation	
Valid SNR Threshold	5.65 dB

†There are currently two monopulse modes; clamped and legacy. When calculating the monopulse ratio of the sum and difference channels, clamped mode forces the phase between the channels to either 0° or 180°. Legacy mode replicates ODAS behavior and uses the measured phase in the calculation of the monopulse ratio.

In addition to DRADIS, a number of other post-processing techniques have been implemented to improve the quality and consistency of data from year to year. As a general overview, the steps involved in producing a final data set are as follows:

1) MIT/LL collects orbital debris radar data, producing debris, spiral scan, and sphere track data, which are recorded using the MIT/LL PACS and transferred to JSC. Additional details regarding the orbital debris radar data collection are in Figure 3-4.

2) Debris data files are batch processed with DRADIS using spiral scans as calibration inputs.

3) Sphere track files are processed through DRADIS calibration routines to independently produce SENS files that contain calibration constants (delta RCS) for the data set.

    a) These are compared to SENS files provided by MIT/LL to ensure consistency.

4) Individual detection files produced by DRADIS are compiled into FY detection lists – MIT/LL datasets are taken on a U.S. Government FY basis – and include all pointing geometries for the radar.

5) Manual Radio Frequency Interference (RFI) review is performed on all valid detections via Range Doppler Image (RDI) inspection; individual RFI detections are removed from the detection list and placed on a separate "removed" list.

6) The FY detection list is split into separate detection lists for each pointing geometry.

    a) Subsequent processing is dependent on pointing-specific parameters.

7) Data for each detection list is screened for anomalous Doppler/range-rate measurements. The anomalous Doppler will be discussed later in this section; it often indicates RFI that was not picked up in the manual RFI review process.

8) A polarization filter for Sodium-Potassium (NaK) discrimination is defined based on PP RCS/polarization scatterplots and identification of the clustering of NaK objects that are observable from two-dimensional projections involving altitude, Doppler-derived inclination, and polarization.

9) Calibration quality is checked using the PP RCS clustering characteristics of the NaK debris population, which are nominally electrically conductive, sphere-shaped particles related to the peak in the resonance region for the monostatic RCS from a conducting sphere. Data of insufficient calibration quality is removed from the dataset and placed on the "removed" list.

10) A standard set of charts illustrating the behavior of the data set over relevant radar and environment parameters including range, range-rate, RCS, SEM-estimated size, SNR, inclination, and altitude are generated for inspection by orbital debris subject matter experts.

11) Standard chart sets are compared with previous FY data to ensure behavior is consistent and/or differences are understood.

12) Once all differences are understood, a final detection list is placed under configuration management such that it may be used by teams involved in modeling the orbital debris environment.

Additional details about the individual steps outlined above are presented in the following sections.

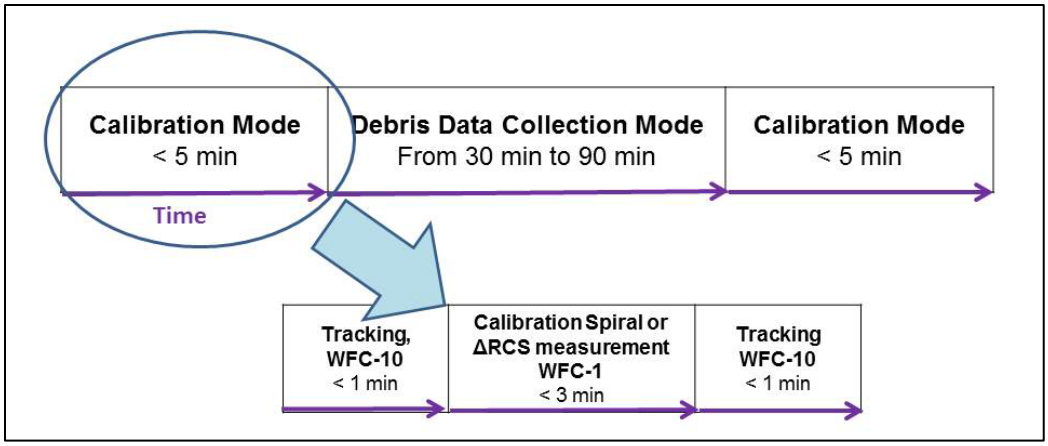

Figure 3-4. Orbital debris data collection and pre- and post-data collection timeline. Object track is conducted by MIT LL using the narrow band WFC-10. The beam shape calibration spiral is conducted by MIT LL using the CW WFC-1. One or more calibration mode segments may be conducted before and after each data validation mode segment.

3.2. DRADIS PROCESSING

A high-level overview of the operations conducted by DRADIS in processing data files delivered by MIT/LL is described in Figure 3-5. As can be observed in the figure, DRADIS conducts multiple passes for detection and then measurement of parameters for objects passing through the beam of both HUSIR and HAX. The first pass is an initial detection pass, whereby the I and Q samples from the radar, along with user-specified signal processing parameters, are used to identify whether an object was present (or not). The steps involved in making the decision regarding a detection are described in Figure 3-6.

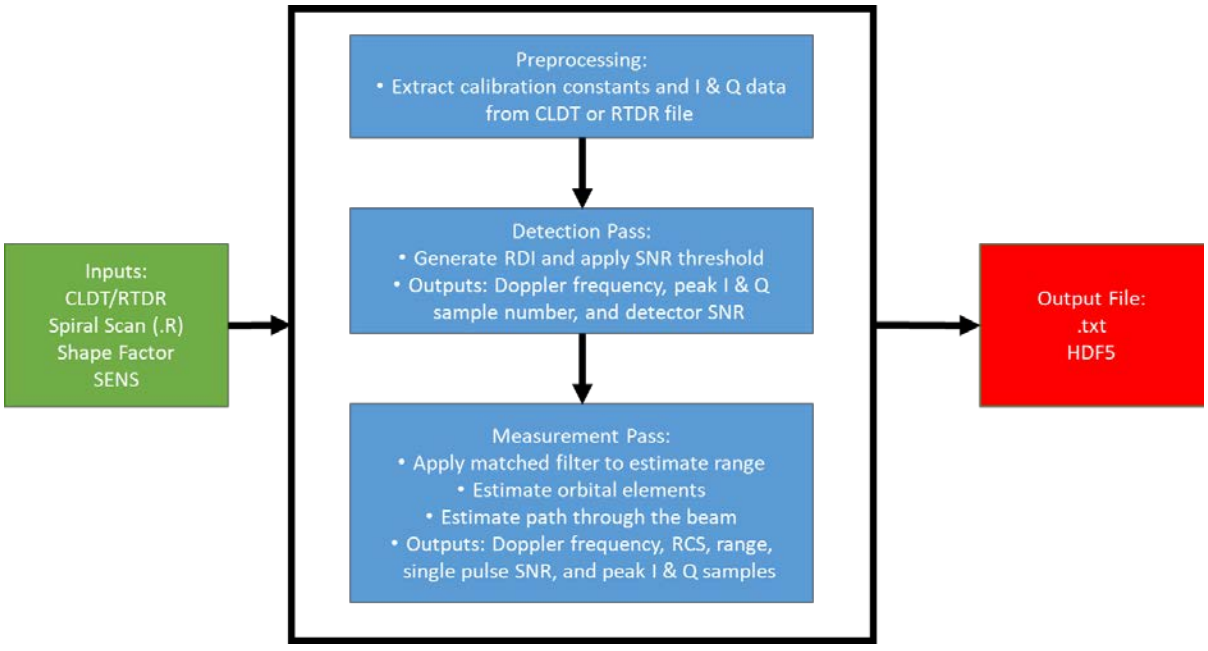

Figure 3-5. Overview of the radar data processing conducted by DRADIS.

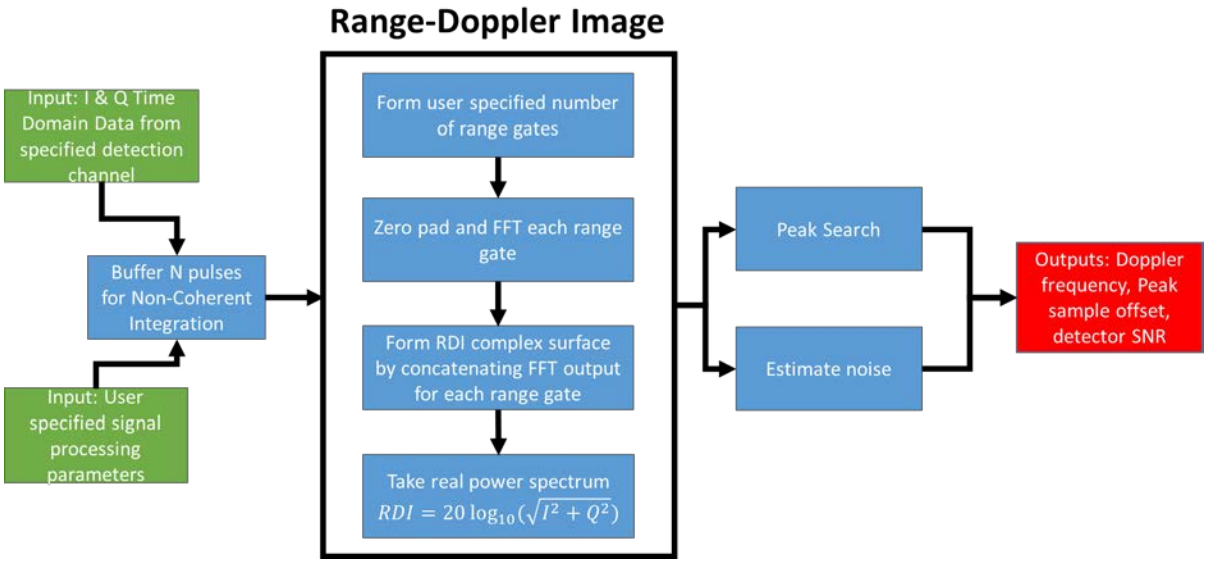

Figure 3-6. Detection pass algorithm employed by DRADIS.

If a detection is identified, DRADIS outputs initial estimates for the Doppler frequency, SNR, and approximate sample offset in the range gate containing the detection, which are then used as inputs to the first measurement pass. A description of the steps taken in the first measurement pass is shown in Figure 3-7. The measurement passes produce the actual detected object information from the four-channel radar pulse data. At the end of the second measurement pass, depicted in Figure 3-8, the Doppler frequency, PP and OP SNR, Doppler-derived orbit inclination, path-through-the-beam corrected RCS, and NASA SEM-generated size estimate are output for a detected object.

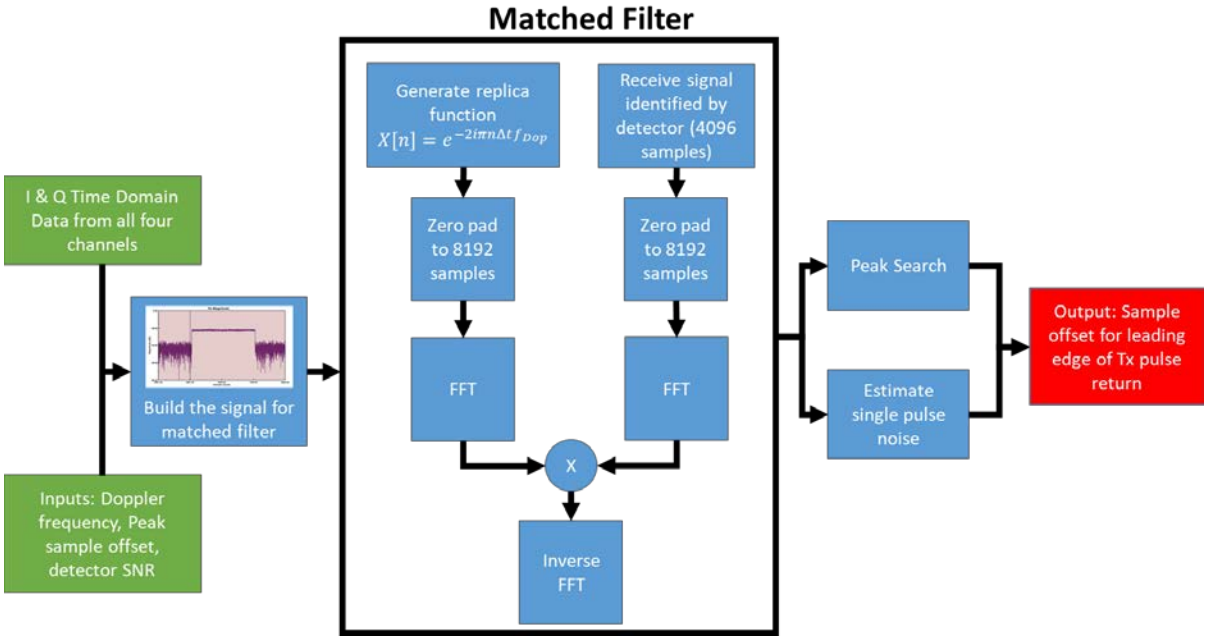

Figure 3-7. First measurement pass algorithm employed by DRADIS.

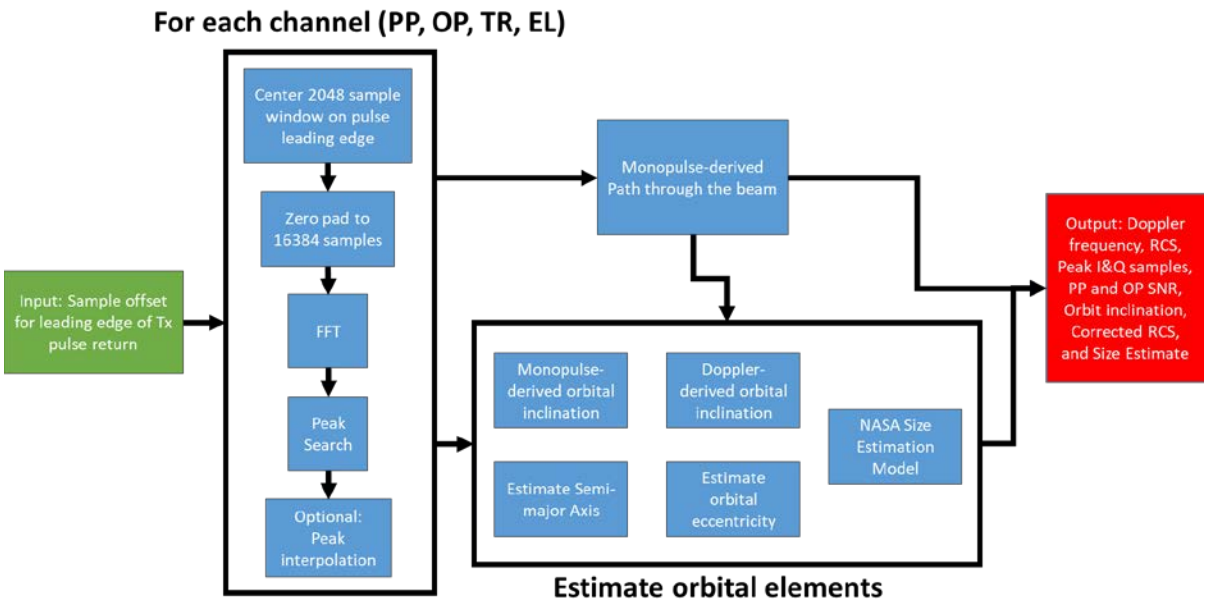

Figure 3-8. Second measurement pass algorithm conducted by DRADIS.

During the second measurement pass, DRADIS estimates a detected object's path through the beam using information derived from the monopulse traverse and elevation channels. This path is then estimated using a linear least squares fit to correct for the beam roll-off that would otherwise assign an incorrect RCS estimate to a detected object that does not pass exactly through boresight. High-level details of the monopulse-derived path through the beam algorithm are shown in Figure 3-9. At the end of this stage, the corrected RCS, as well as information on whether the object went through the 3 dB-beamwidth of the radar is available for the detected object.

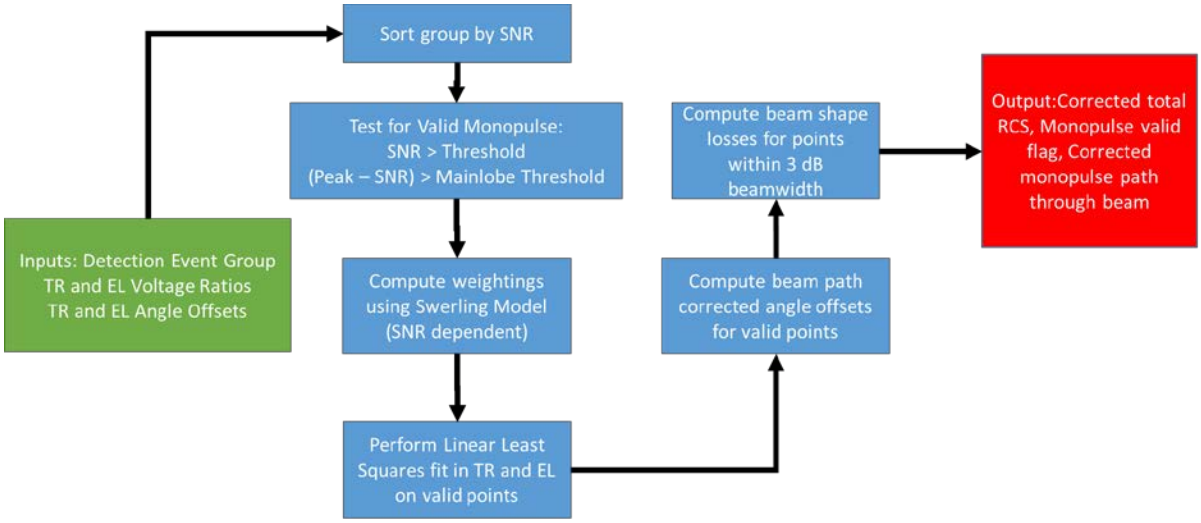

Figure 3-9. Algorithm for estimating monopulse-derived path through the beam.
TR = traverse and EL = elevation.

Verification and validation of algorithm implementation within DRADIS initially was conducted using several on-orbit calibration sphere passes. In addition to the typical calibration spheres that MIT/LL employs to calibrate the radar, additional data collects on the Polar Orbiting Passive Calibration Spheres (POPACS) was conducted. POPACS (SSN 39268, 39269, and 39270) are 10 cm calibration spheres, originally in a 325 x 1500 km and 81 degree-inclined elliptical orbit, that provide a lower SNR object to test the radar signal processing chain within DRADIS against the typical set used by MIT/LL.

Satellite Trajectory and Attitude Kinetics (SATRAK) was used to calculate expected values of range and range-rate for each pass. The expected RCS was calculated from the theoretical size-to-RCS of a sphere using the published diameters of the calibration spheres. Of the ten planned calibration sphere passes, eight passed through the 3 dB-beamwidth of HUSIR. A summary of the test results from those eight passes, where good agreement with theoretical results for most of the sphere tracks was obtained, is shown in Table 3-3 and Table 3-4.

Table 3-3. Calibration Sphere Pass Results with DRADIS v1.2.5

Sphere SSN # (day_pass)†	39490 (075_1)	1520 (076_1)	902 (076_1)	5398 (076_1)	1512 (076_1)	1521 (076_2)
Range Error (km)	-14.88326	0.845432	0.999124	1.03913	0.138952	1.20143
Range-rate Error (m/s)	0.309414	2.496965	2.141141	2.200455	-0.059207	1.25037
Doppler Frequency Error (Hz)	20.6276	166.4643	142.7427	146.6970	-3.9471	83.3580
Total RCS Error (dBsm)	0.383768	0.287915	1.253155	0.928994	1.466997	0.535878

†Day is the day of year in which the data was taken. For some spheres, multiple data collects were conducted on the same day. A "pass" number is used to distinguish the datasets.

Table 3-4. Theoretical and DRADIS v1.2.5 Calculated RCS Values for Standard Calibration and POPACS Conducting Spheres

Sphere	Theoretical RCS	Measured RCS	RCS Error (dB)
39490 (DOY 075)	-2.467	-2.083	0.384
1520 (DOY 076)	-9.9893	-9.7013	0.288
902 (DOY 076)	-9.9893	-8.7363	1.253
5398 (DOY 076)	-0.0653	0.8637	0.929
1512 (DOY 076)	-9.9893	-8.5223	1.467
1512 (DOY 076)	-9.9893	-9.4533	0.536
POPACS 2 (Up)	-21.0791	-19.4172	1.661
POPACS 2 (Down)	-21.0791	-20.357	0.721

3.3. SPHERE TRACK CALIBRATION

The operators at MIT/LL regularly perform end-to-end calibration of the radar system to minimize measurement errors. Several times a day the operators track and measure the RCS of known calibrations spheres, such as SSN 900, 902, 1520, 1512, and 5398, as they pass through the radar field of view. The measured RCS is compared with the known RCS of the given sphere and a correction factor is calculated using the following equation:

$$delta\_RCS = RCS_{measured} - RCS_{theoretical}$$

This process is carried out before every orbital debris radar data collection and the correction factor, known as the delta RCS, is applied in post-processing to the data collected. Below is a plot of the delta RCS versus elevation collected for FY2017.

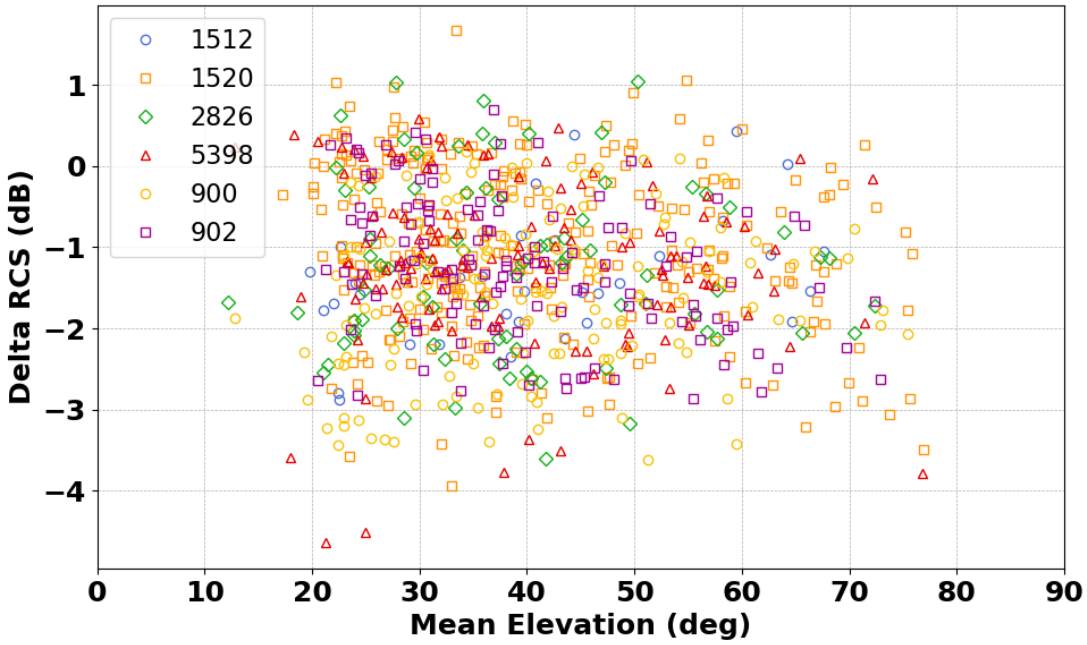

Figure 3-10. Delta RCS versus Elevation for FY2017 with calibration objects identified.

During the processing and validation of HUSIR FY2016 – FY2017 data files, NASA and MIT/LL determined that the original delta RCS files MIT/LL provided were incorrect. The issue was discovered during an investigation of an apparent bias in the cumulative RCS distributions in FY2017 with respect to the other years. In the course of the investigation, an ability to process sphere track files was added to DRADIS to independently calculate the calibration offset using this software. When comparing the delta RCS values computed by MIT/LL and NASA for the same sphere track, the two were in good agreement until the last quarter of FY2016. The differences in delta RCS values computed by each organization were consistent with an error in the computed range, which affects the measured RCS. MIT/LL data processing software began using the leading edge of a range gate as the range in its calculations whereas the true range includes the additional distance from the start of the range gate to the location of the returned signal within the range gate. This additional distance is referred to as the range window offset.

Figure 3-11 shows the delta RCS residual, defined as the delta RCS calculated by DRADIS minus the delta RCS calculated by MIT/LL, as a function of the mean measured range for sphere track files from FY2014-FY2017. The dashed line represents the expected residual, assuming the range window offset error. Although it is unclear how this change was introduced into the processing software of MIT/LL, it has been confirmed as the cause and was subsequently corrected. Radar data from FY2016 and FY2017 are processed using delta RCS values calculated by DRADIS from the calibration sphere tracks provided by MIT/LL.

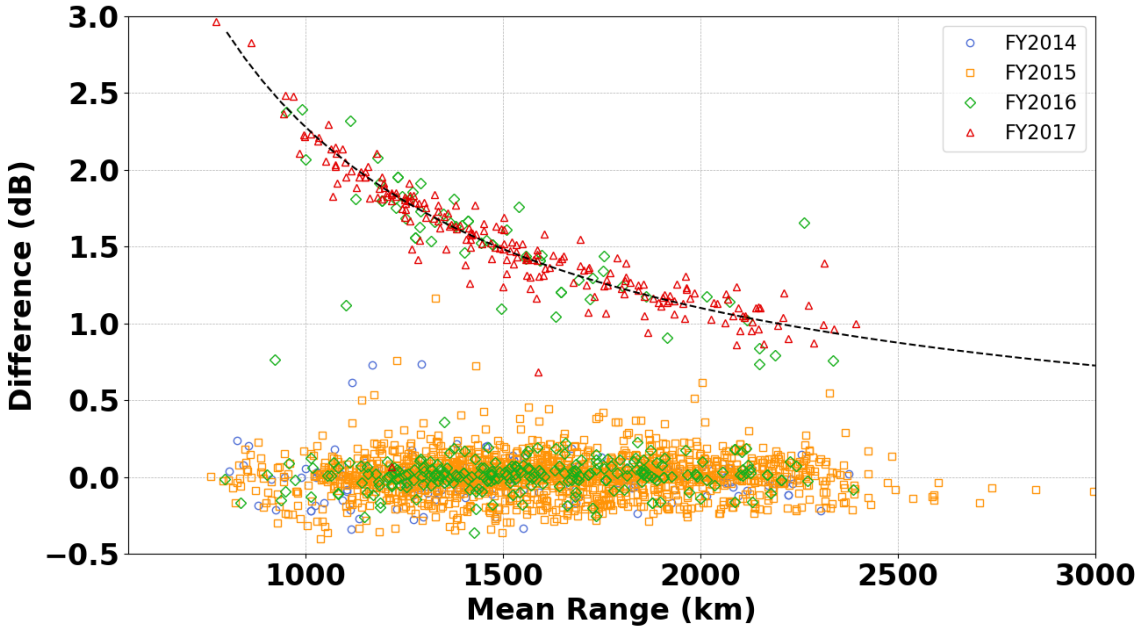

Figure 3-11. DRADIS-derived delta RCS residuals versus the mean range for sphere track files from FY14-FY17. The dashed line represents the expected correction due to range window offset. All residuals from FY14 and FY15 are centered near zero. All residuals from FY17 lie along the dashed line. The residuals from FY16 are split between the two, indicating a change in FY16.

3.4. SPIRAL SCAN CALIBRATION

To calibrate the antenna beam gain pattern, MIT/LL performs spiral scan calibrations before an orbital debris radar data collection period. As the name implies, a spiral scan calibration involves tracking a known object, preferably a calibration sphere, on boresight and then slowly spiraling outwards so that the 3-dB beam width is sufficiently sampled and a beam shape can be fit to the resulting data. This process can be carried out on LEO objects, which requires the antenna to maintain track across the sky while scanning the object in a manner that results in a spiral pattern centered on the object. It is also possible, and preferable, to perform a spiral scan on an object in GEO that acts like a point source, which allows for a smoother and tighter spiral pattern since the object is stationary in the sky. Shown in Figure 3-12 below is the output data from a spiral scan in DRADIS. Such plots are used when evaluating the quality of the spiral scan and beam shape calibration thereby obtained.

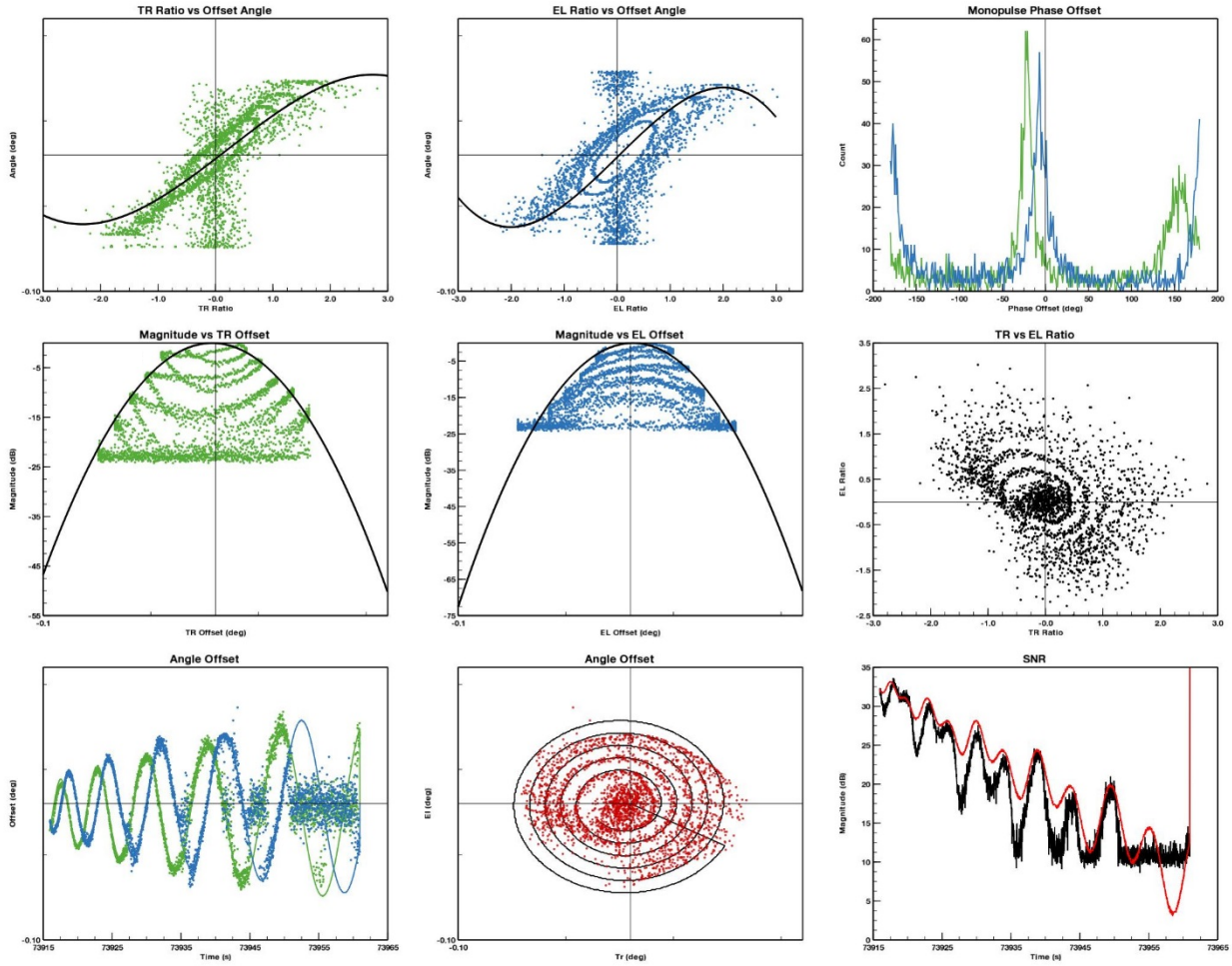

Figure 3-12. Data visualization (screenshot) in DRADIS of a spiral scan on a GEO satellite.

Since the spiral scans are conducted with the radar returns from metallic spheres, only the PP channel can be directly calibrated with this method. The OP beam shape is assumed to be the same as the PP beam shape. Periodically, MIT/LL uses intermediate frequency (IF) test signal injection in both the PP and OP channels to calibrate the magnitude and phase errors of the OP channel relative to the PP channel.

3.5. 16- VERSUS 32-RANGE GATE PROCESSING

Historical radar data processing was conducted with ODAS, which was limited to processing CLDT-formatted files. Data in these files was, for historical hardware and software reasons, pre-formatted into 16 range gates and the software did not have the capability to reconstruct the original receive window. DRADIS does not have this restriction and allows for a user-specified number of range gates for both RTDR- and CLDT-formatted files. During analysis of the FY2015 HUSIR data, it was noted there was noticeable banding of detections in range/altitude that did not have a physical justification. This banding was present in ODAS-processed data as well, and can be seen in previous radar reports published by NASA ODPO. Further analysis confirms that this banding corresponds with the spacing of the default 16 range gates, as can be seen in Figure 3-13. While several of these spikes correspond to regions of high debris

populations, such as 700 km to 1000 km, there were also increased detection counts at even longer slant ranges where the only correlation seemed to be with the range gate overlap and not debris populations.

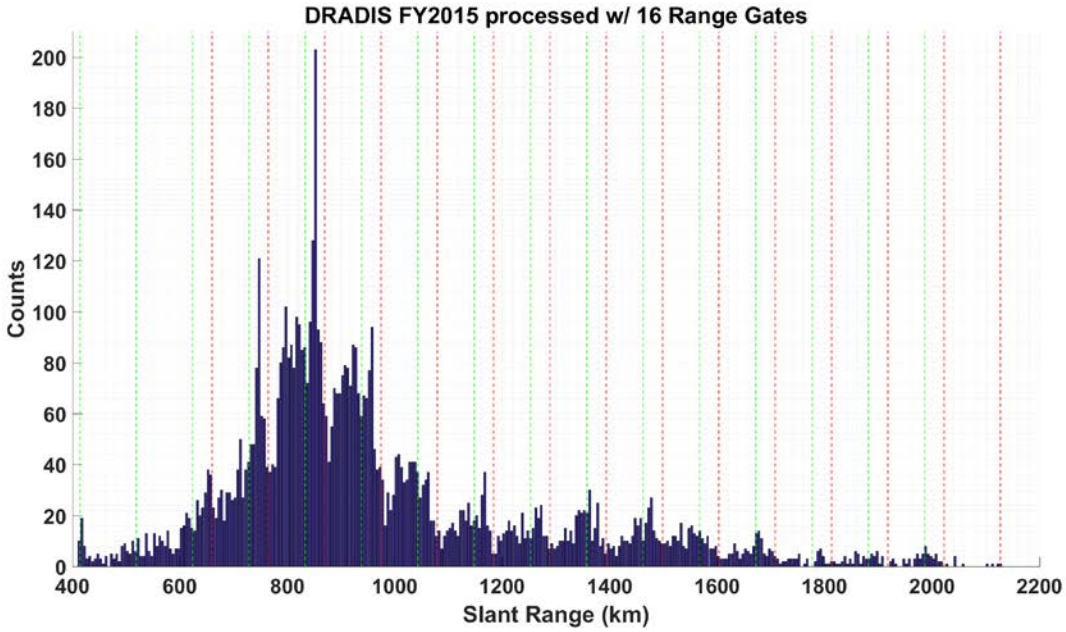

Figure 3-13. Counts versus slant range with 10 km bins for 16 range gates. The green and red vertical lines correspond with the start and stop ranges, respectively, of each range gate. The spikes in detections correspond with overlap between range gates.

Initially, it was decided to reprocess the FY2015 data using 32 range gates as an experiment to see what effect the increased number of range gates would have on the distribution of detections – the finer sampling in range was reasoned to produce a smoother distribution. In Figure 3-14, is the comparison between 16-gate processing and 32-gate processing. As hypothesized, the 32-range-gate processing led to a smoother and more physical distribution of detections in range. Because of this analysis, all of the data presented in this report was processed with 32 range gates, which is shown in Table 3-2.

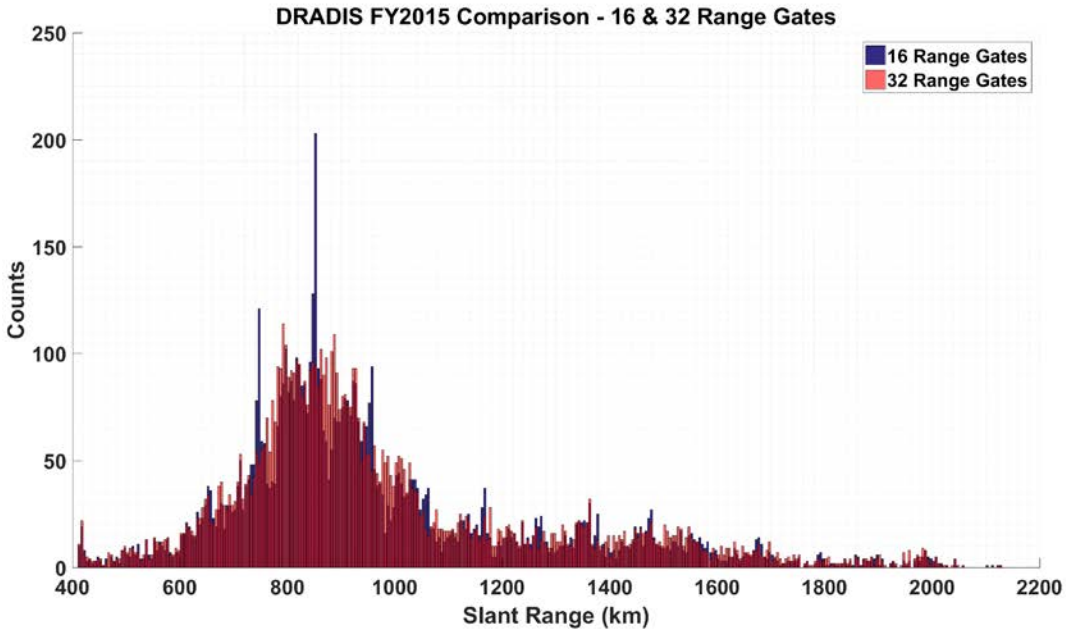

Figure 3-14. Comparison of distributions of detections in 16 range gates versus 32 range gates.

3.6. RFI REVIEW

During the analysis phase of DRADIS testing, a subset of detections was discovered, which had an SNR history that featured transient spikes and fluctuations of 30 dB or more within a detection group. Further investigation revealed these detections were not from orbital debris traversing the beam but instead were from RFI. Based on current estimates, RFI accounts for 5% to 15% of detections in a given fiscal year dataset. The percentages for FY2014-FY2017 are in Table 3-5.

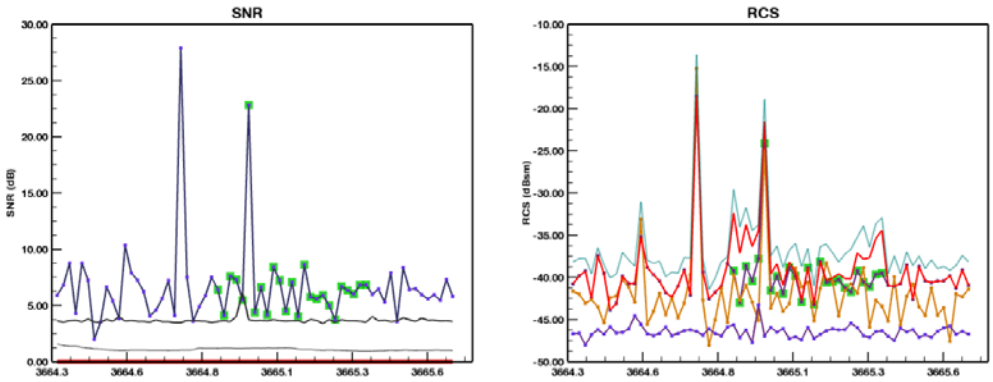

Figure 3-15. SNR and RCS time history of a detection determined to be RFI (DRADIS screenshot).

The procedure for collecting radar data at MIT/LL is for the radar operator to cease debris data collection when repeated RFI contamination is observed. As a result, the bulk of RFI contamination occurs randomly throughout the year at the end of dataset collection and therefore, is concentrated in a handful of days.

Table 3-5: Percentage of Detections Determined to be RFI for FY14-FY17

Fiscal Year	FY2014	FY2015	FY2016	FY2017
RFI Percentage	4.67%	5.68%	6.65%	14.2%

Figure 3-16 shows the RCS distributions of the FY2017 data before RFI was removed, the FY2017 data after RFI was removed, and the detections determined to be RFI. The RFI appears to have a roughly uniform distribution, using one over square meters measured in decibels (dBsm), from -20 dBsm to -60 dBsm. The net effect of the RFI on the cumulative size distributions can be seen in Figure 3-17. The presence of RFI tends to raise the cumulative curve starting at approximately 30 cm. The greatest effect happens at approximately 7 cm, where the presence of RFI doubles the cumulative count rate of objects measured to be 7 cm or larger.

The discovery of RFI in the FY2014-2017 datasets implies the existence of RFI in historical datasets. Although Figure 3-17 shows the potential effects of the presence of RFI, it should be noted that when compared to FY2014-FY2016, FY2017 had a much higher percentage of RFI. An additional investigation would be necessary to determine the full effect of the presence of RFI in historical datasets and its effect on environmental models.

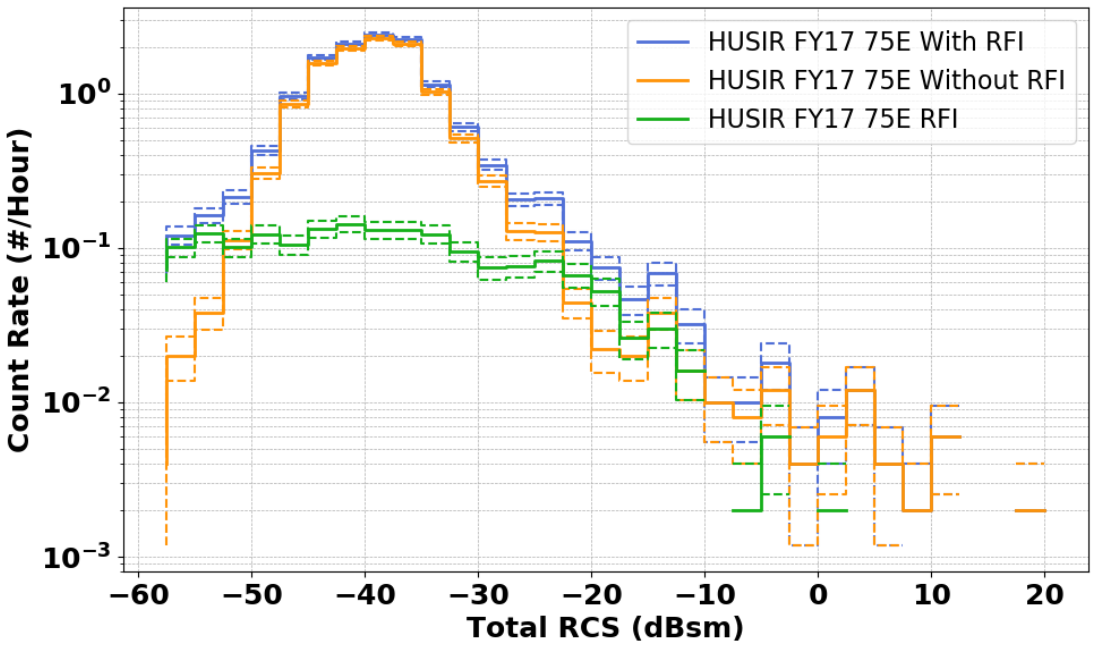

Figure 3-16. Total RCS distributions for the data and RFI from FY2017. Dashed lines represent 1σ uncertainty bounds.

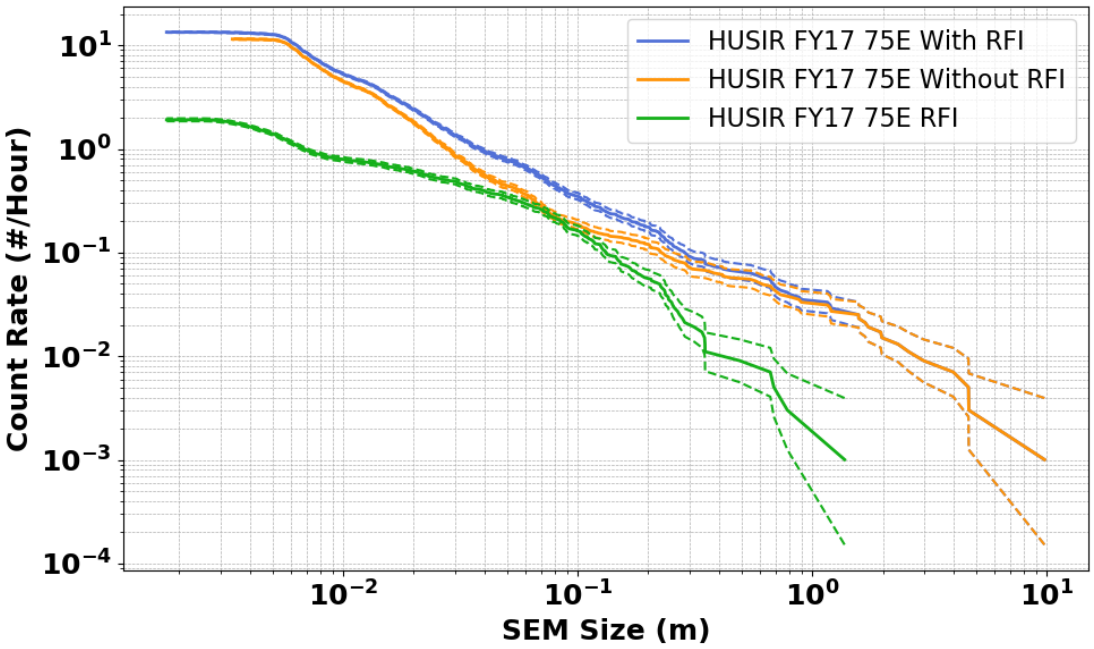

Figure 3-17. Cumulative size distributions of the data and RFI from FY2017, showing the effect of RFI on the cumulative size distributions. Dashed lines represent 1σ uncertainty bounds.

3.6.1. *Manual RFI Review*

Currently, DRADIS does not provide an automated way to flag or remove RFI from the data set; instead, this requires a manual review of the detection range-Doppler image (RDI) to look for RFI signatures. Figure 3-19 shows a set of RDIs for all four channels of a detection that has been determined to be RFI. The most common form of RFI identified to-date persists through multiple range gates and is present at multiple frequencies across the downconverted IF band – see Figures 2-1 and 2-2 for reference. This creates a striping effect that is readily identifiable in an RDI.

To perform a thorough screening of the data to remove RFI, a post-processing step has been implemented in which a set of RDIs, as shown below, were created for each valid detection within a data set. An analyst manually reviewed the set of RDI plots and flagged all detections determined to be RFI. Then these individual detections were removed from the final detection list and placed on the “removed” list, as described previously. For comparison, Figure 3-18 shows a set of RDIs for all four channels of a typical, high-SNR debris detection. The signal is present in only a small number of adjacent Doppler bins and range gates with a single, readily identifiable peak.

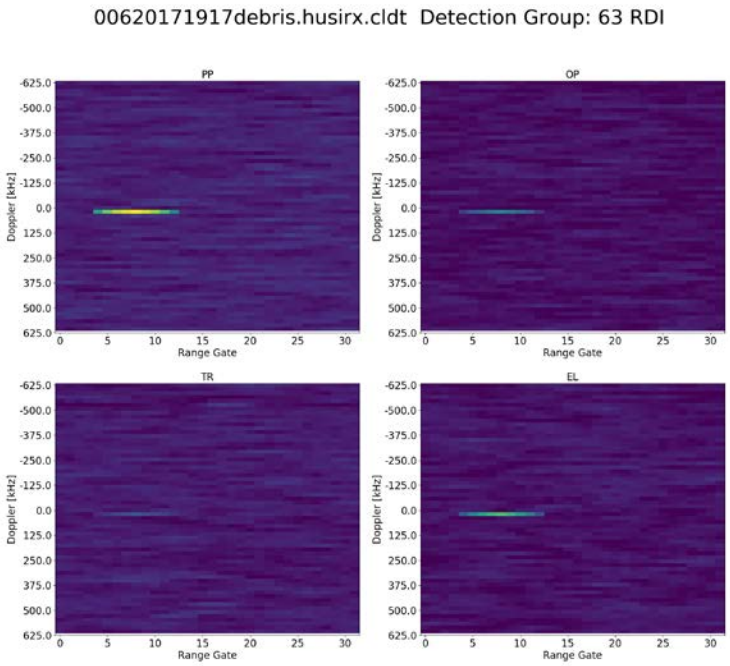

Figure 3-18. Single-pulse RDI illustrating the characteristic signature of a high-SNR debris detection. The debris detection will have a single, readily identifiable feature in each of the four plots, which is isolated to a single Doppler bin and persists through only a few range gates.

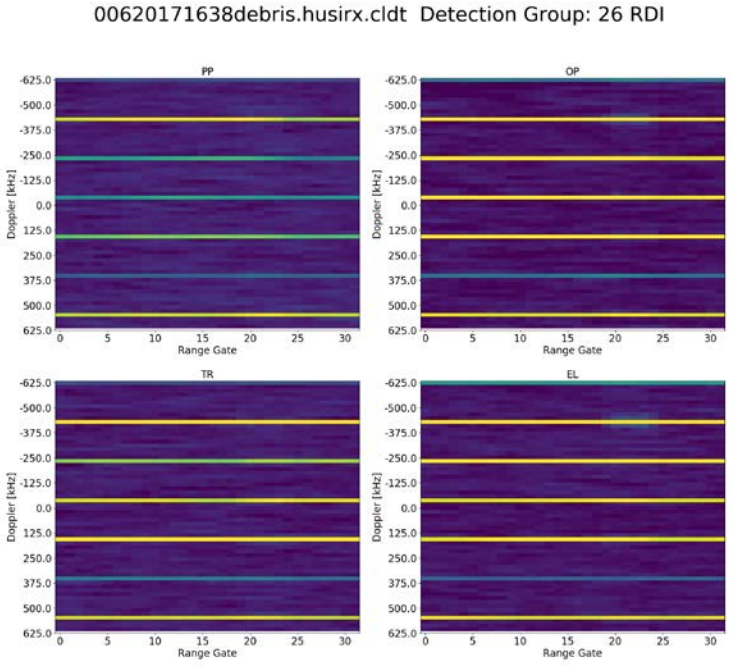

Figure 3-19. Single-pulse RDI illustrating the characteristic signature of RFI in orbital debris datasets. The RFI detection will have multiple, horizontal linear features that persist across many range gates.

3.6.2. *Anomalous Doppler Identification*

Another common feature of RFI signals present in orbital debris radar data sets is the distribution of measured range-rates or Doppler changes for RFI relative to orbital debris detections. These may arise from the carriers or subcarriers of various communication systems, or be due to harmonics of the frequencies employed in a communication system due to the sensitivity of the radar. Additionally RFI is usually concentrated in a short period of time, which results in detection rates higher than the mean detection rate of orbital debris. These features lend themselves to another method for identifying RFI in which the range-rate is plotted as a function of time, usually day of year. Although orbital debris detections can have range-rates as large as ±7 km/s in LEO, a significant number of these detections with debris objects having nearly circular orbits is unlikely, and the majority of detections for the primary observation geometry have range-rates in the ±2 km/s range. Since RFI is uniformly distributed in range-rate, this leads to large vertical stripes in range-rate versus time plots. Figure 3-20 shows an example of such striping from the HUSIR FY2017 75° elevation data. Once identified, all detections from the affected time period are removed from the detection list. Additionally, the hours of observation associated with the time period are removed from the total number of hours observed.

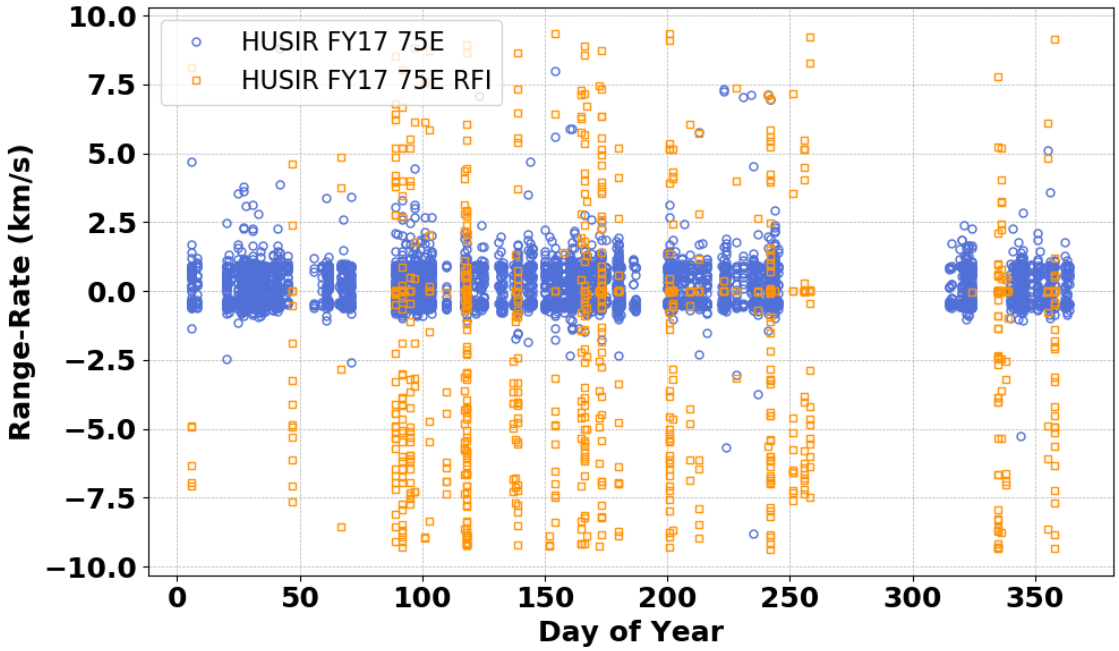

Figure 3-20. Range-rate versus day of year for FY2017 75E data with RFI identified.

3.6.3. *NaK PP RCS Clustering*

In previous studies, highly polarized debris with inclinations near 65° and an altitude between 700 km and 1000 km were identified as spherical, eutectic, NaK nuclear reactant coolant droplets from ejected cores of the Soviet/Russian Radar Ocean Reconnaissance Satellites (RORSAT). This stable population, which is discussed in greater detail in Section 4, has proven to be a useful secondary calibration check. Due to the scattering characteristics of the NaK droplets, one expects to see a clustering of detections with PP RCS values around -35 dBsm for the center

frequency of HUSIR. Data that clusters around a different PP RCS value is indicative of a potential calibration issue including, but not limited to, data taken in the rain, hardware calibration errors or DSP timing offsets, and bad sphere-track calibrations.

Inspection of a plot of PP RCS versus day of year, filtering on the characteristic altitude, inclination, and polarization criteria for NaK, has been added to the processing procedures. Figure 3-22 shows an example of such a plot for the HUSIR FY2017 75° elevation data. When a time period is identified as being poorly calibrated, an attempt is made to remediate the data. If the data is not recoverable, it is removed from the final detection list, and again, the hours of observation associated with the time period are removed from the total number of hours observed. A clearer illustration of the difference between accepted and rejected time windows can be seen in Figure 3-21, where the cumulative PP RCS count rate distributions of NaK can be seen for both the accepted and rejected (removed) data. NaK PP RCS distributions, as measured by HUSIR, are expected to have a sharp rise detection rate at -35 dBsm. This inflection point for the removed data is offset from the expected value by approximately 2 dB.

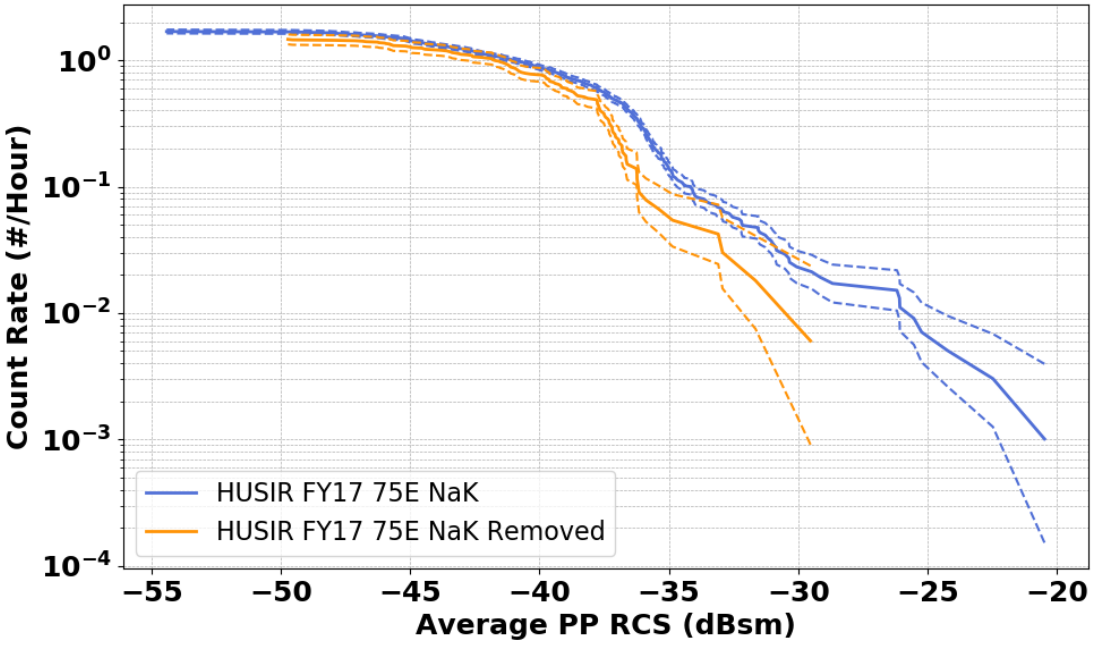

Figure 3-21. Cumulative PP RCS distributions for NaK in FY2017 75E data in accepted and rejected time windows

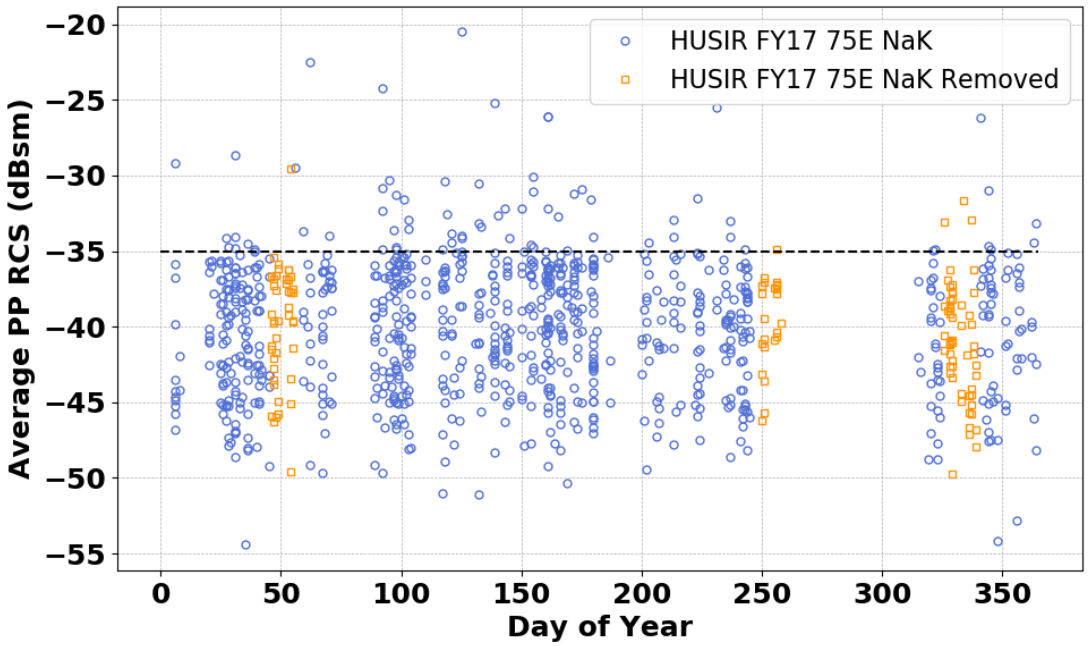

Figure 3-22. PP RCS versus day of year for NaK in FY2017 75E data with data removed due to poor calibration identified. The dotted line represents the expecting RCS clustering value for HUSIR.

3.7. THE NASA SIZE ESTIMATION MODEL

NASA commissioned a study by XonTech, Inc to develop an SEM to relate RCS to physical size. Representative debris objects were selected from two hypervelocity impacts of simulated satellites conducted at the Arnold Engineering Development Complex by the U.S. Department of Defense [6, 7]. Some artificial, debris-like objects also were included in the sample to better represent the postulated orbital debris environment at the time. The RCS values for these 39 debris objects were measured at a controlled RCS radar range operated by the System Planning Corporation. These objects were measured over 4 radar frequency bands (S-band: 2.5647-3.9111 GHz, C-band: 4.116-7.986 GHz, X-band: 8.1544-12.7684 GHz, and Ku-band: 12.924-17.538 GHz) with 8 steps in the lowest frequency band, with 16 steps in the other frequency bands, and with hundreds of source-object orientations [8-10]. These frequencies were chosen since they represent radar frequencies often used for orbital debris observations.

The characteristic length of an object is defined as the average of the largest dimensions for an object measured along three orthogonal axes. The first axis was chosen to coincide with the largest dimension, the second axis to coincide with the largest dimension in a plane orthogonal to the first axis, and the third axis to be orthogonal to the plane defined by the first two axes. In this report, the characteristic length of an object is referred to interchangeably as size or diameter.

Consistent with Maxwell's equations of electromagnetics, radar data from different wavelengths can be compared by normalizing the size by the wavelength of the measuring frequency and the RCS by the wavelength squared. This results in a size parameter x=size/wavelength and an RCS parameter z=RCS/wavelength^2. In [6], the relationship between the measured RCS parameter

and the object's physical size parameter are shown. Each of the 2072 points on this plot is a weighted average for a single object over hundreds of different orientations at a single frequency. The data was weighted to account for non-uniform sampling of the object orientations as the data was collected [6-10].

From this plot a scaling curve (smooth solid line) was developed, which represents the mean of the measured RCS for each size/wavelength. For debris sizes much smaller or larger than the radar wavelength, the scaling curve approaches the Rayleigh or optics region curves, respectively. Between the Rayleigh and optics region curves is the Mie resonance region. The scaling curve may be expressed as:

$$x = \sqrt{\frac{4z}{\pi}} \text{ , for } z>5, \text{ Optical Regime}$$

$$x = \sqrt[6]{\frac{4z}{9\pi^5}} \text{ , for } z<0.03, \text{ Rayleigh Regime}$$

$$x = g(z) \text{ , in between, Mie Resonance Regime}$$

where z=RCS/λ^2, x=diameter/λ, and λ is wavelength. In the above equations, the quantity z is expressed on a linear scale and not in dB. The smooth function g(z) is determined from a linear fit in log space to the 23 points in Table 3-6.

Table 3-6: Details of the SEM in the Mie Resonance Region

x=diameter/λ	z=RCS/λ²
0.10997	0.001220
0.11685	0.001735
0.12444	0.002468
0.13302	0.003511
0.14256	0.004993
0.15256	0.007102
0.16220	0.01010
0.17138	0.01437
0.18039	0.02044
0.18982	0.02907
0.20014	0.04135
0.21237	0.05881
0.22902	0.08365
0.25574	0.1190
0.30537	0.1692
0.42028	0.2407
0.56287	0.3424
0.71108	0.4870
0.86714	0.6927
1.0529	0.9852
1.2790	1.401
1.5661	1.993
1.8975	2.835

Note that most of the debris observed by HUSIR is in the Rayleigh region, which allows size estimates that are relatively insensitive to errors in the RCS measurements.

For comparison, the oscillating RCS-to-size curve for Mie scattering from a spherical conductor is shown, in blue, in Figure 3-23. The NASA SEM is not applicable to estimated sizes of spherical conductors (such as NaK droplets) in the Mie Resonance region – due to the one-to-many mapping of a given RCS to size in this regime. The oscillations result from constructive and destructive interference of electromagnetically-induced surface waves on the exterior of the conducting sphere.

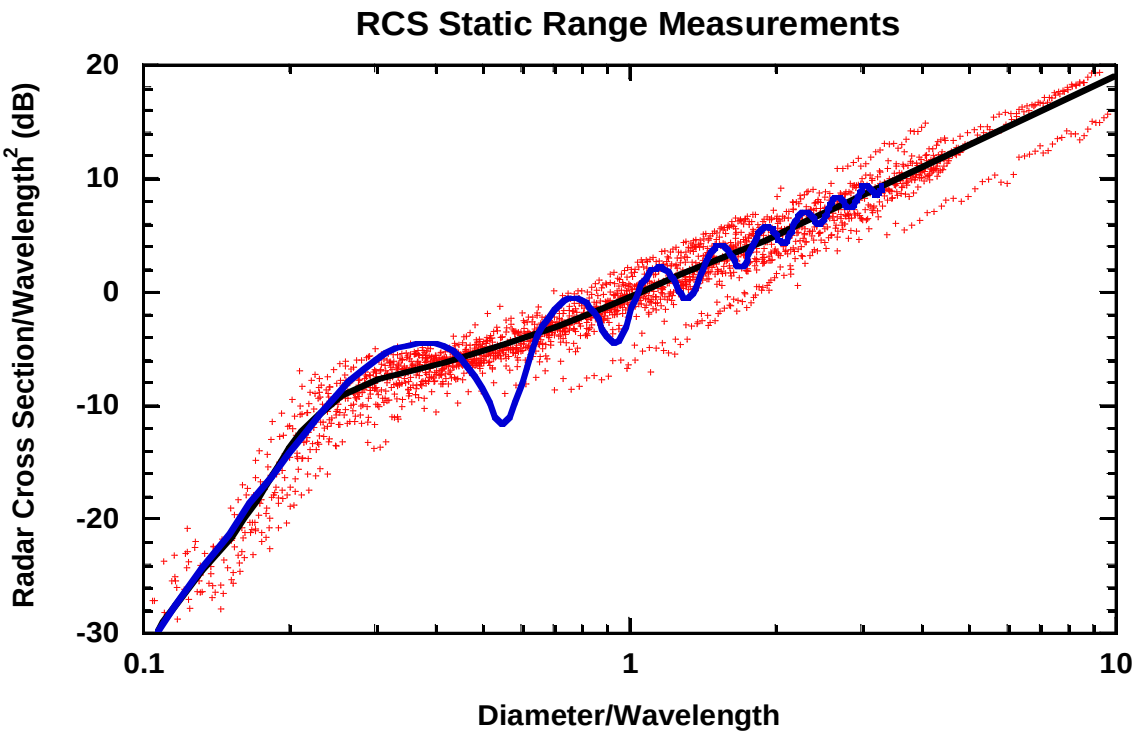

Figure 3-23. Results of RCS-to-physical size measurements on 39 representative debris objects over the frequency range 2.0 to 18 GHz (15 cm to 1.67 cm wavelength). Each point represents an average RCS for a single object measured at a single frequency over many orientations. The oscillating line is the RCS for a spherical conductor while the smooth line is the polynomial fit to the data.

4.0 Results

4.1. DATA COLLECTION OVERVIEW

The majority of data from FY2014 through FY2017 was collected in a 75° elevation, east-staring geometry. The 75° east geometry provides enough Doppler discrimination to estimate some orbital parameters of the detected debris objects such as inclination, if a circular orbit is assumed. In this configuration, detected objects are in orbits with inclinations equal to or greater than the latitude of the radar. Observations were also performed at 10° and 20° elevations in south-staring geometries. Although this increases the slant range for a given altitude, which impacts sensitivity, it allows the radar to measure debris in orbits as low as 28° or higher.

Table 4-1 shows the number of observation hours at 75°, 20°, and 10° elevations and the total number of detections in each configuration, by year.

- The 75° elevation observations were conducted with a minimum range of 415 km and a maximum range of 2232 km, which corresponds to orbital altitudes from 392 km to 2166 km.

- The 20° elevation observations were conducted with a minimum range of 835 km and a maximum range of 2654 km, which corresponds to orbital altitudes from 325 km to 1321 km.

- The 10° elevation observations were conducted with a minimum range of 1255 km and a maximum range of 3074 km, which corresponds to orbital altitudes from 327 km to 1168 km.

Observation hours represent the total number of hours remaining after the removal of observation windows that were determined to be contaminated with RFI. Very few hours were taken in south-staring geometries in 2017 due to the reduced sensitivity in that year. The number of detections represents the total number of events for which there were three or more pulses with an integrated SNR greater than 5.65 dB, where at least one is in the two-way, 6 dB-beamwidth (one-way, two-sided 3 dB-beamwidth). A table showing the total number of hours received from MIT/LL is provided in Appendix B.

Table 4-1: Data Collection Summary Reflecting the Final Culled Data Sets

Fiscal Year	75° East		20° South		10° South	
	Hours of Observation	Number of Detections	Hours of Observation	Number of Detections	Hours of Observation	Number of Detections
2014	268.1	4107	0	0	57.3	352
2015	288.4	4858	67.2	715	86.1	593
2016	458.5	7079	142.8	1433	139.6	904
2017	496.2	5701	1.2	6	0.5	1

4.2. RADAR MEASUREMENTS

The majority of observations performed in the 2014-2017 time frame were taken in a staring mode in which the radar is pointed at a fixed point in space performed in the 75° elevation, east-staring geometry. In this configuration, radar measurements of the debris environment are obtained in a range from 415 km to 2232 km. This corresponds to an altitude range of 392 to 2166 km.

This section uses the 75° elevation data from 2014 as an example to represent the types of information available in the dataset. A comprehensive set of plots from all years covered by this report are presented in appendices C through E. There, range versus range-rate, range versus RCS, altitude versus inclination, cumulative SEM size distributions, cumulative PP SNR distributions, cumulative RCS distributions, and polarization distributions are presented for each radar and pointing direction. Additionally, total flux versus altitude and inclination are presented for 75° elevation observation geometries.

4.3. RANGE VERSUS RANGE-RATE

As an object passes through the radar beam, two fundamental measurements are made: range and range-rate. The range is the distance between an object and the radar; it is calculated from the time of propagation of the transmitted signal from the radar to the object and back. The range-rate measures the velocity of an object along the direction of the radar beam. Velocity parallel to

the boresight direction of the radar manifests as a Doppler shift in the returned signal from which a range-rate can be calculated.

Figure 4-1 presents the range plotted against the range-rate for the 75° elevation data from 2014. Although detections with range-rates as high as ±7 km/s are present in the data, the majority of detected objects have range-rates in the ±2 km/s.

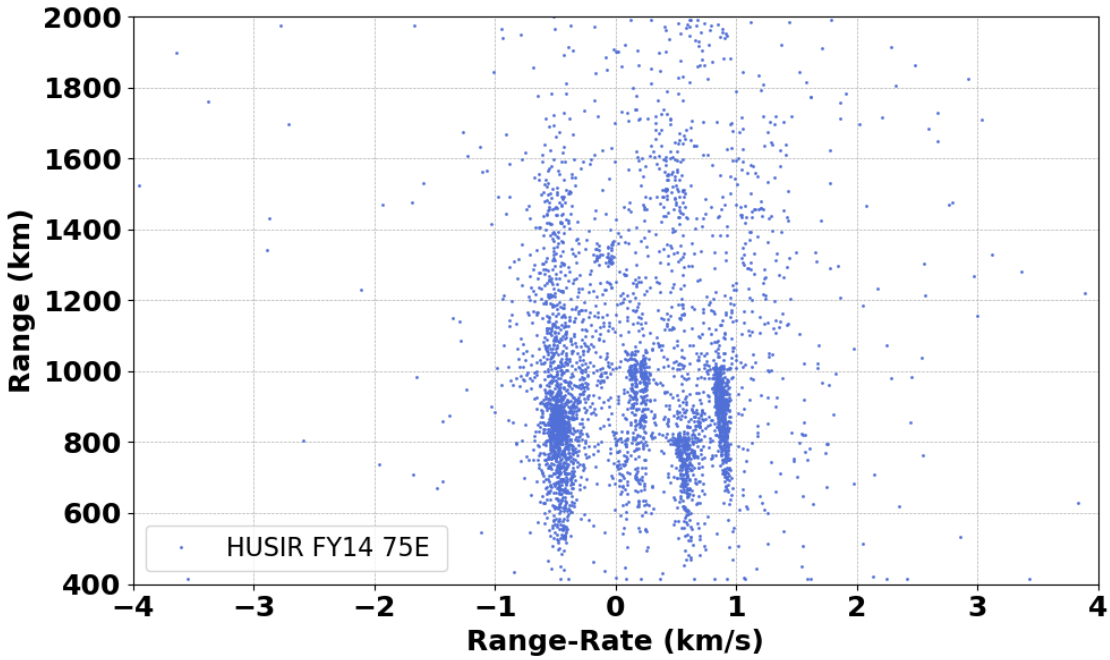

Figure 4-1. Range versus range-rate for the HUSIR 75° elevation data from 2014.

4.4. ALTITUDE VERSUS INCLINATION

There are two methods of determining the orbital inclination of an object detected by the radar in the staring mode. In a method using the radar's monopulse capabilities, the time history of the object's position through the beam is determined from the open-loop, monopulse azimuth (or traverse), and elevation voltage ratios, which are converted into direction and angular velocity across the beam. The direction and angular velocity along with the range, range-rate, and time history are transformed into the classic orbital elements, including inclination. Inclination derived using this method is referred to as the monopulse inclination. Although this method works well for large SNR values, as SNR degrades, the monopulse inclination estimates quickly become invalid. In the 75° elevation pointing, the angle between the orbit and the radar beam is sufficiently different from 90° that the range-rate measurement can identify the orbital inclination with minor ambiguity in the resulting values, if a circular orbit is assumed. Orbits on ascending (traveling south to north) passes will have slightly different range-rates than orbits with the same inclination, but on descending (traveling north to south) passes. At 75°, the ambiguity is small enough that an inclination valid to approximately a degree can be obtained by averaging the two possible inclinations [14]. Inclination estimates derived using this technique are referred to as Doppler inclinations. Since the majority of detections have moderate- to low-

SNR values, the inclinations presented herein are all Doppler inclinations and not monopulse inclinations.

The improvement in inclination estimation afforded by the Doppler method allows “families” of debris objects to be defined and studied separately. While it is impossible to say whether an individual detection is in a particular family because of the uncertainty in its eccentricity, the data in Figure 4-2 shows detections clustered into distinct families and defined by limits of inclination and altitude, which are consistent with the presumed parent bodies in the SSN cataloged population.

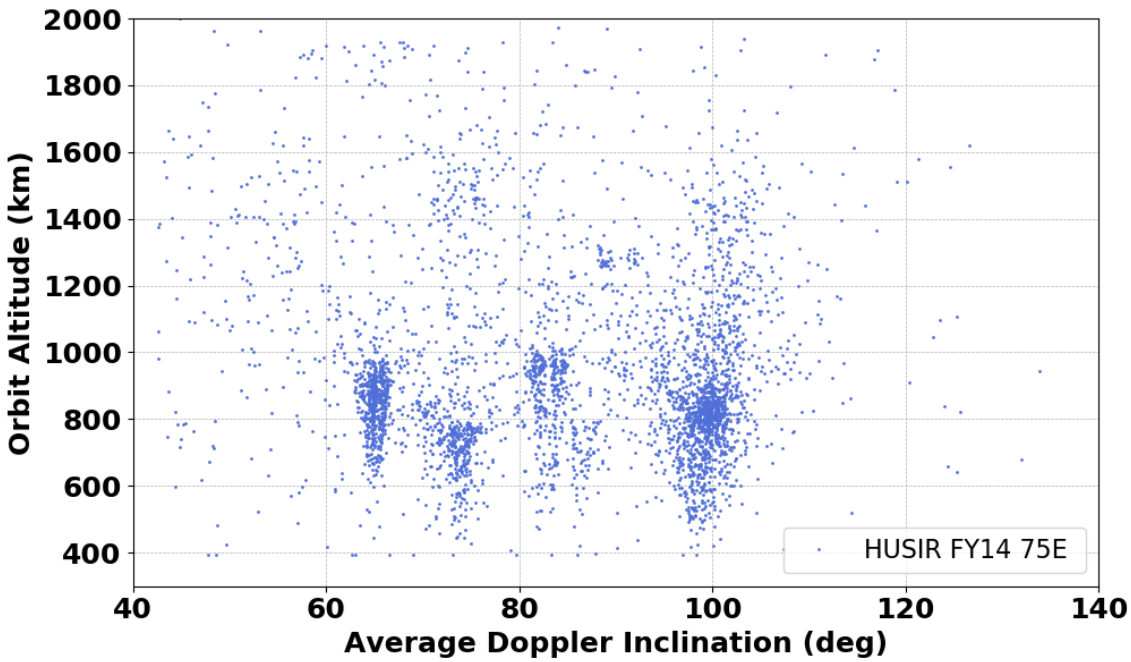

Figure 4-2. Altitude versus Doppler inclination for the HUSIR 75° elevation data from 2014.

4.4.1. *Range v. Total RCS*

In addition to range and range-rate, one of the main measurements performed by the radar is that of RCS. Shown in Figure 4-3 is a plot of total RCS versus range for the HUSIR 75° elevation data from 2014. The dashed black line represents the theoretical RCS of an object, with an integrated SNR of 5.65 dB, as a function of range using the average sensitivity of HUSIR in FY2014. Objects to the left of the curve have a much smaller probability of detection.

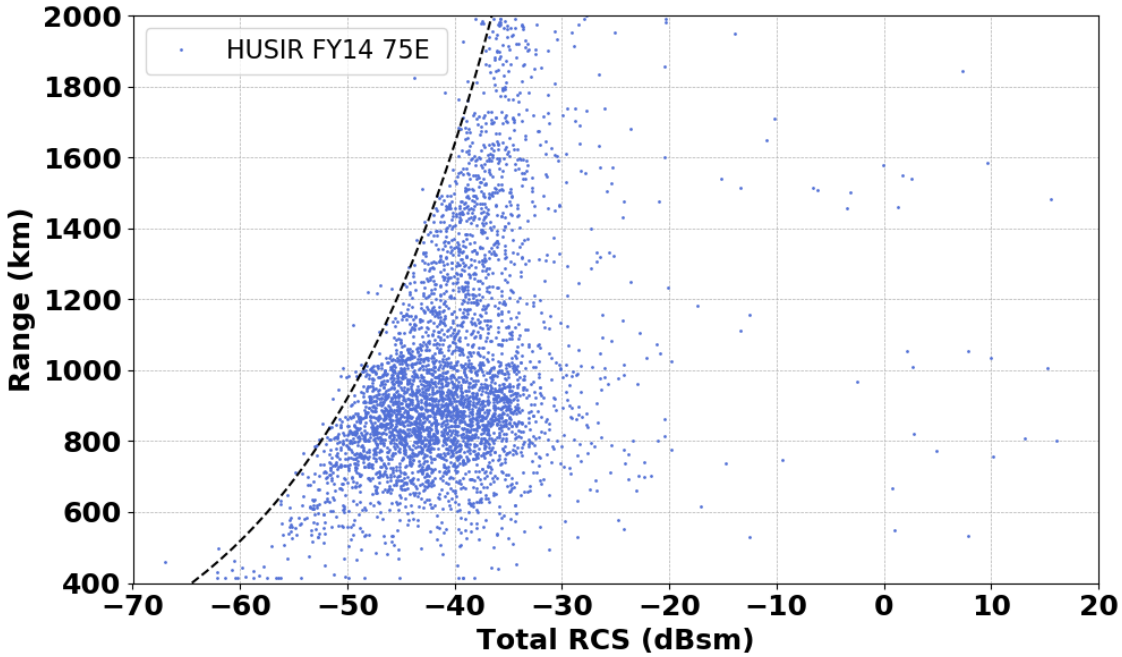

Figure 4-3. Range versus total RCS for the HUSIR 75° elevation data from 2014.

4.4.2. *Polarization Distribution*

The HUSIR radar transmits right-hand circular polarization and receives both left-hand and right-hand circularly-polarized radar returns, which are referred to as the PP and the OP, respectively. The polarization (P) is defined as:

$$P = \frac{RCS_{PP} - RCS_{OP}}{RCS_{PP} + RCS_{OP}}$$

A polarization value of +1 indicates that the object is very sphere-like, since for circularly-polarized waves, the polarization of the reflected wave is orthogonal to that of the transmitted wave. A polarization value near 0 indicates that an object is more dipole-like, since dipoles receive energy equally well from either polarization ($RCS_{PP} = RCS_{OP}$). A plot of the polarization distribution for the HUSIR 75° elevation data from 2014 is shown in Figure 4-4. As one moves from negative values of the polarization parameter toward more positive values, the detection rate increases until approximately the value of zero. The distribution then flattens out with a slightly higher detection rate for objects with polarizations greater than 0.7. This is due, in part, because the radar detector is configured only to trigger a detection on the PP channel, which leads to a deficit of detections for objects with high OP but low PP signatures.

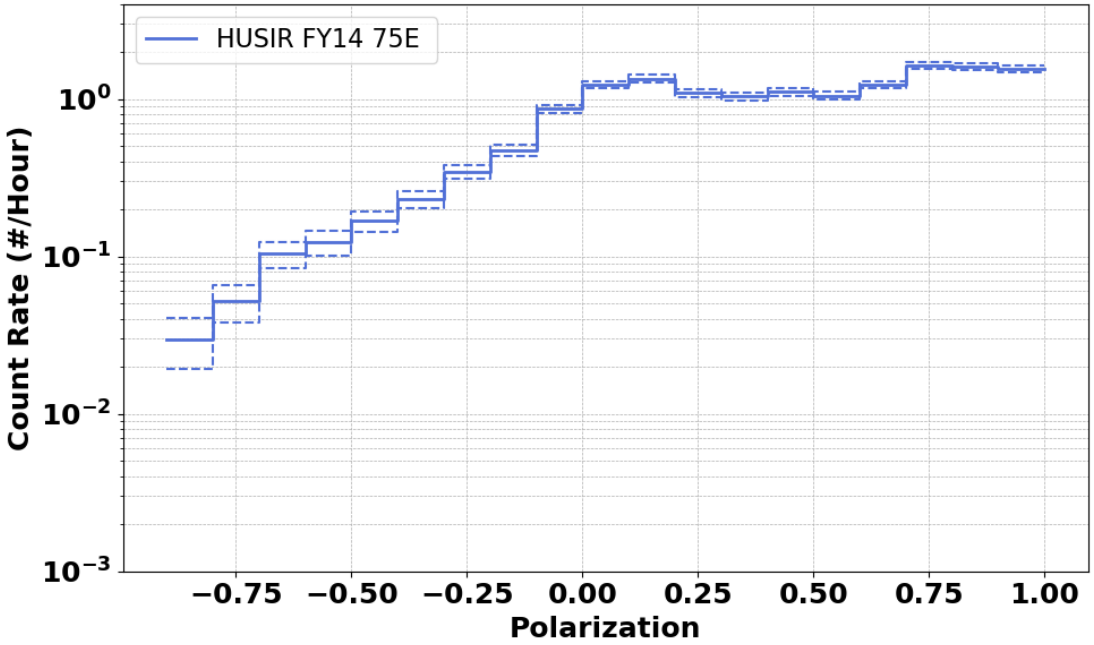

Figure 4-4. Polarization distribution for the HUSIR 75° elevation data from 2014.

4.4.3. *NaK Population*

In previous studies [15-17], highly polarized debris (P ≈ 1) with inclinations near 65° and an altitude between 700 km and 1000 km were identified as spherical, eutectic, NaK nuclear reactor coolant droplets from the ejected core of RORSATs. In contrast to debris in other altitude and inclination bands, which exhibit a wide polarization distribution, the NaK population, being composed of small metallic spheres, is highly polarized.

In the past, debris objects with an altitude from 700 km to 1000 km, with a Doppler inclination between 62° and 68°, and with a measured polarization parameter greater than 0.84 were interpreted to be NaK droplets. To increase the number of detected NaK droplets, the polarization filter has been refined. In a noiseless system, the polarization of a sphere would always be +1. In a real system, however, the RCS measured in the OP channel represents the RCS equivalent noise. As one measures smaller, lower RCS spheres, the polarization parameter is expected to decrease as the measured PP RCS becomes closer to the value of the noise equivalent RCS in the OP channel. To account for this phenomenon, a threshold was developed in PP RCS/polarization space for the discrimination of NaK droplets. Figure 4-5 shows a plot of PP RCS versus polarization for objects detected with a Doppler inclination between 62.9° and 67.0° and an altitude below 1000 km. The dotted line represents the threshold used, where all detections above the line were interpreted to be NaK droplets. Note that this line also demarcates the more tightly clustered detections in polarization and RCS space associated with the NaK population. Development of this *ad hoc* line is based on the boundary between the cluster of NaK detections and other objects in this altitude and inclination band.

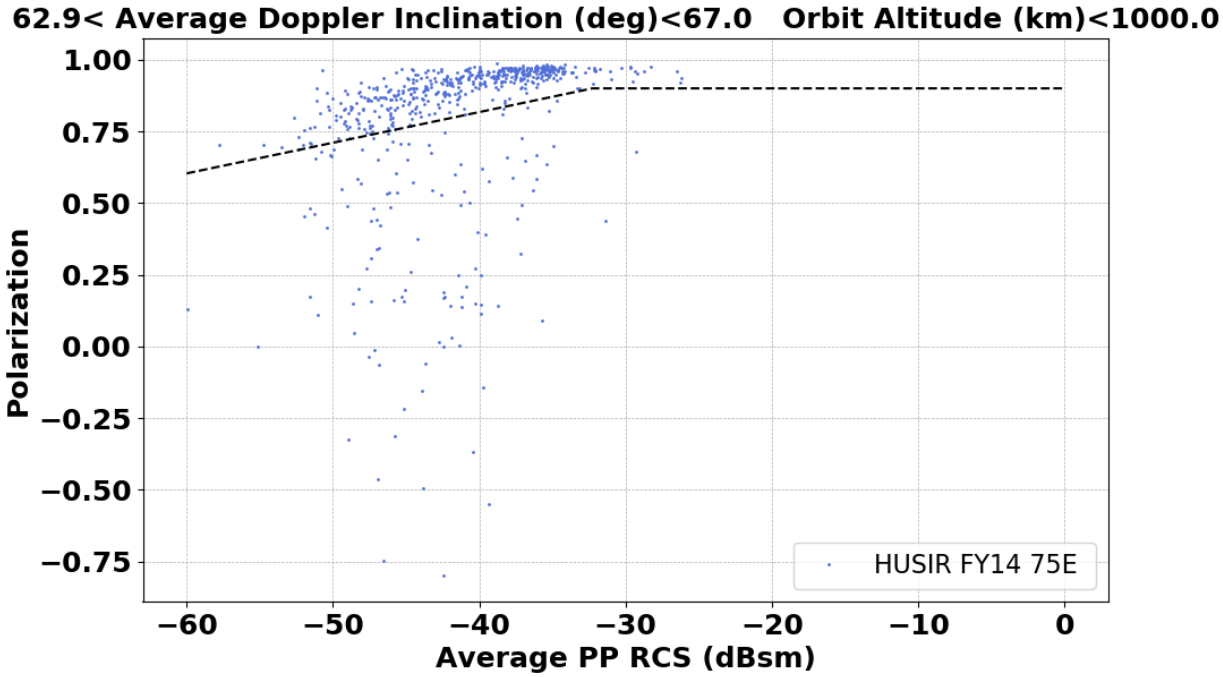

Figure 4-5. Polarization versus PP RCS for the HUSIR 75° elevation data from 2014.

In [2, 14], the NaK PP RCS distribution is shown to be very stable in the -30 to -50 dBsm region. Since the scattering characteristics of spheres is well understood, the expected distribution of NaK detections takes on a very predictable shape that is consistent from year to year, which can be seen in Figure 4-6, where the cumulative PP RCS distribution of particles identified as NaK droplets are shown for all HUSIR 75° elevation data for all years. In particular, the onset of detections at the -35 dBsm mark, which manifests as a slope change in Figure 4-6, serves as a convenient marker for whether the dataset has been properly calibrated. This feature is related to the oscillatory nature of the size-to-RCS curve for a spherical conductor, presented in Figure 3-23.

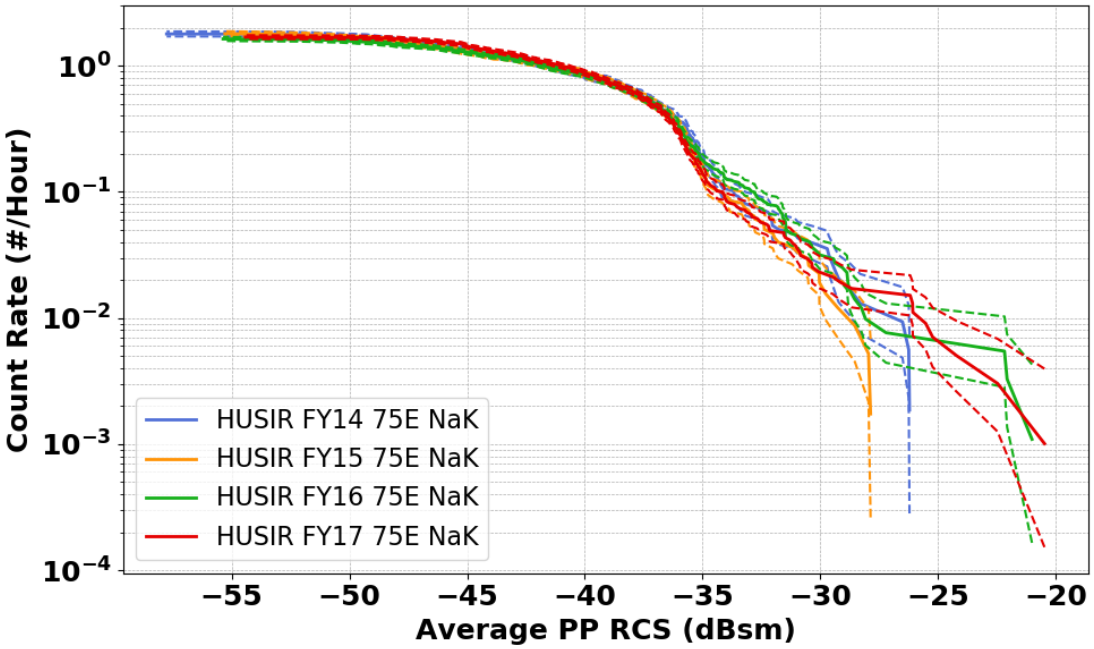

Figure 4-6. PP RCS Cumulative Distribution of the NaK population extracted from all 75° elevation data by year.

4.5. ENVIRONMENT CHARACTERIZATION SUMMARY

The radar data presented here is meant to provide a broad overview of the state of the debris environment in low Earth orbit. Since the radar sensitivity changes from year to year, flux charts presented in this section, which compare all years of data, will be presented with the flux integrated down to a limiting size. Since the sensitivity varies greatly, particularly with the FY2017 data where HUSIR operated with two TWTs for the fiscal year, additional analysis should be performed before drawing conclusions about the environment's development.

A comprehensive set of Cumulative Flux charts for each year of 75° elevation data is presented independently in appendix C. Due to an inadequate amount of well-calibrated data, flux estimates from the 10° and 20° elevation datasets are not presented in this document.

4.5.1. *Flux v. Altitude*

Flux is defined as the number of detections through the lateral surface area of the radar beam within a given period of time. Total flux represents the flux of all objects regardless of size, where size is estimated using the NASA SEM, as described in section 3.7. To aid in comparing different years, cumulative flux to a limiting size is shown. This represents the flux of objects with a size equal to or greater than the chosen limiting size. For all years, cumulative flux is presented to limiting sizes of 5.62 mm and 1 cm, depending upon altitude. To avoid presenting potentially misleading information, each flux chart is limited to altitudes where it is estimated that radars are sensitive to objects of a specific size and above, which is referred to as complete.

This corresponds to approximately 1000 km for a limiting size of 5.62 mm and 1600 km for a limiting size of 1 cm. All flux versus altitude charts are presented using 50 km-altitude bins.

Figure 4-8 shows the cumulative flux versus altitude limited to 5.62 mm for all 75° elevation data, by year. For FY2014 - FY2016, the flux distributions appear stable. The FY2017 flux of objects 5.62 mm and larger appears to diverge from earlier years at around 850 km. This divergence may be attributed to the reduced sensitivity in FY2017, which resulted in a lower "completeness" altitude, and reduced detections for higher altitudes.

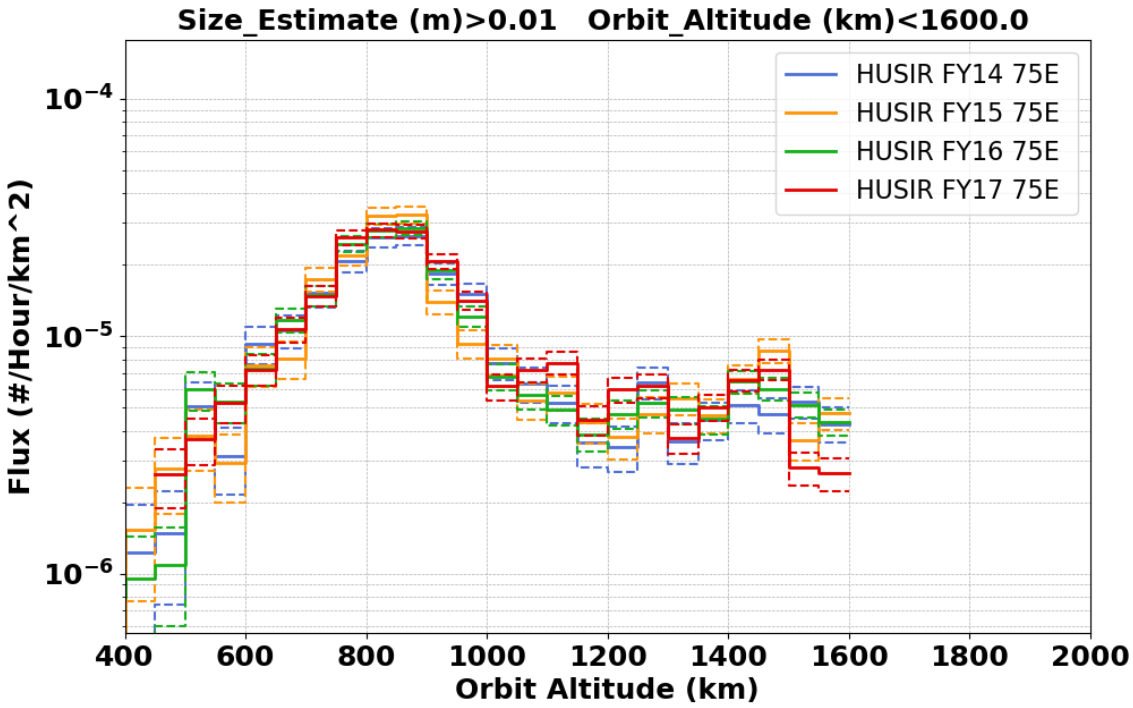

Figure 4-7. Cumulative surface area flux versus altitude limited to 1 cm for all 75° elevation data by year. The dashed lines represent 1σ uncertainty bounds.

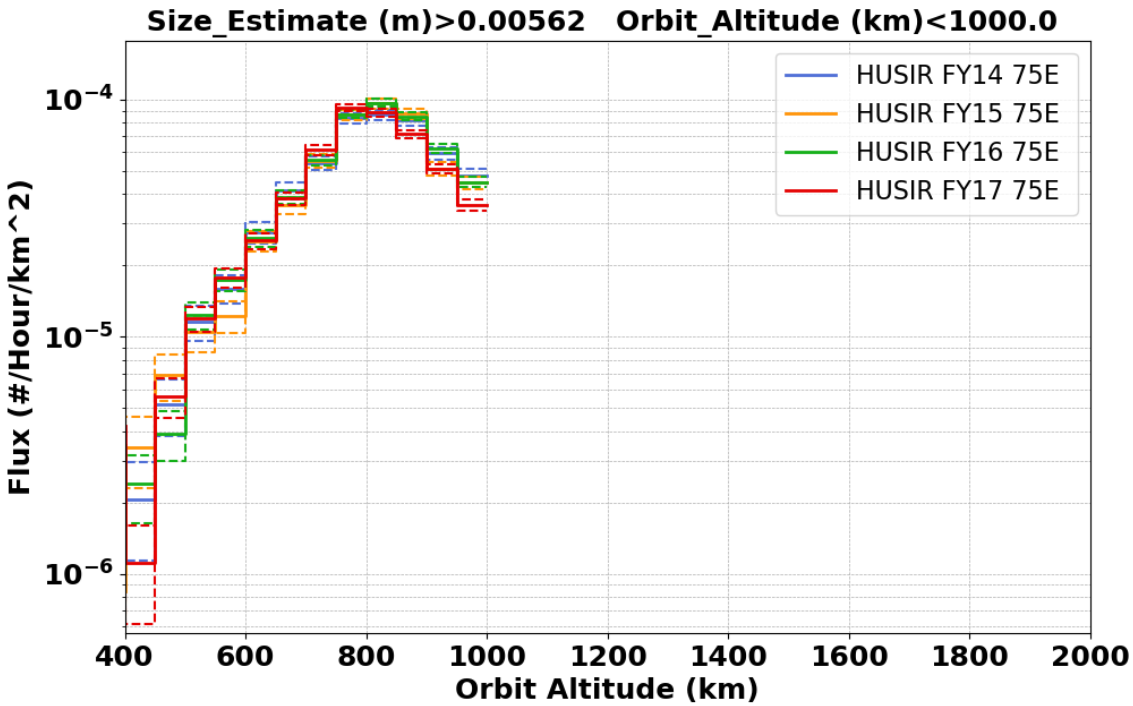

Figure 4-8:Cumulative surface area flux versus altitude limited to 5.62 mm for all 75° elevation data by year. The dashed lines represent 1σ uncertainty bounds.

4.5.2. *Flux v. Inclination*

In addition to flux versus altitude, examining flux versus inclination gives more insight to the distinct populations/families of debris. Flux is defined in the same fashion as above, except that the beam area is the total surface area of the beam from the minimum observable altitude to the maximum observable altitude, since each altitude bin can measure debris at all inclinations available to the radar in the 75° east-staring geometry. The fluxes presented in this section will be to limiting sizes of 5.62 mm and 1 cm and use 2° sized bins.

When flux is broken down by inclination, very distinct groupings become apparent. The most prominent are those between 94° and 105° associated with the sun-synchronous family of orbits, 71° and 78°, which is associated with the Iridium 33-Cosmos 2251 collision; and 63° and 67°, which is associated with the NaK coolant droplets ejected from RORSAT nuclear reactors. Additionally, an uncorrelated family of debris in the 81° to 87° inclination band has been identified and is currently under investigation to determine the source.

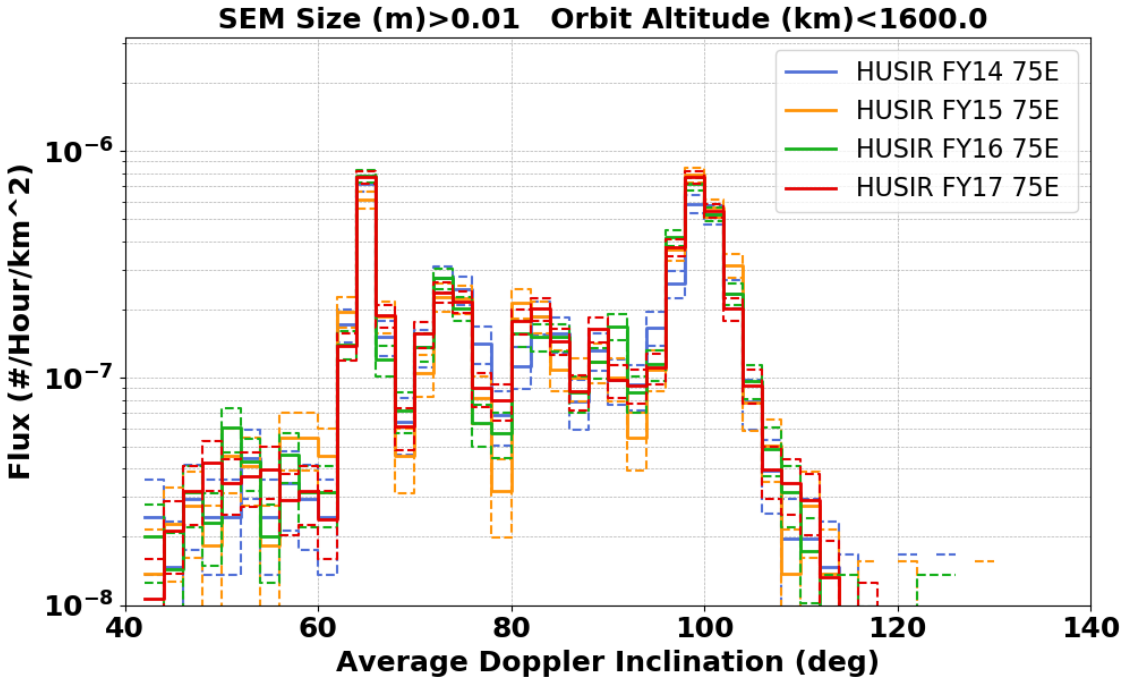

Figure 4-9. Cumulative surface area flux versus inclination limited to 1 cm for all 75° elevation data by year. The dashed lines represent 1σ uncertainty bounds.

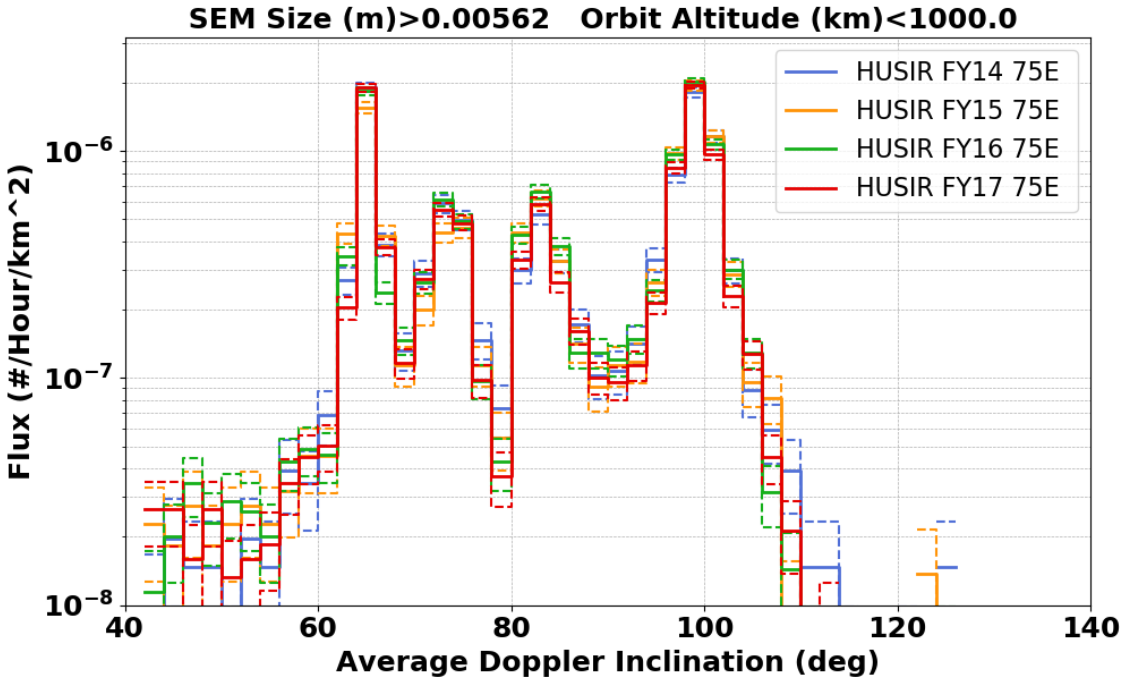

Figure 4-10. Cumulative surface area flux versus altitude limited to 5.62 mm for all 75° elevation data by year. The dashed lines represent 1σ uncertainty bounds.

4.5.3. *SEM-size Cumulative Distribution*

The total count rate of debris changes from year to year due to fluctuations in radar sensitivity. Although the flux charts from previous sections circumvent this issue by examining flux to limiting sizes, looking at the cumulative size distributions provides insight into the behavior across a greater range of sizes. For sizes down to approximately 6 mm, the size distributions each year are remarkably consistent. If one examines the behaviors at smaller sizes, it can be seen that the FY2017 distribution rolls off more quickly than in other years, which is consistent with the reduced sensitivity in FY2017. FY2017 also appears to differ from other years for objects greater than approximately 20 cm. The reason for this is currently not known. An estimate of the Poisson uncertainty in the count rate is shown using dashed lines to represent the estimated 1-sigma (σ) confidence intervals. A detailed discussion of the uncertainty estimation is found in Appendix A.

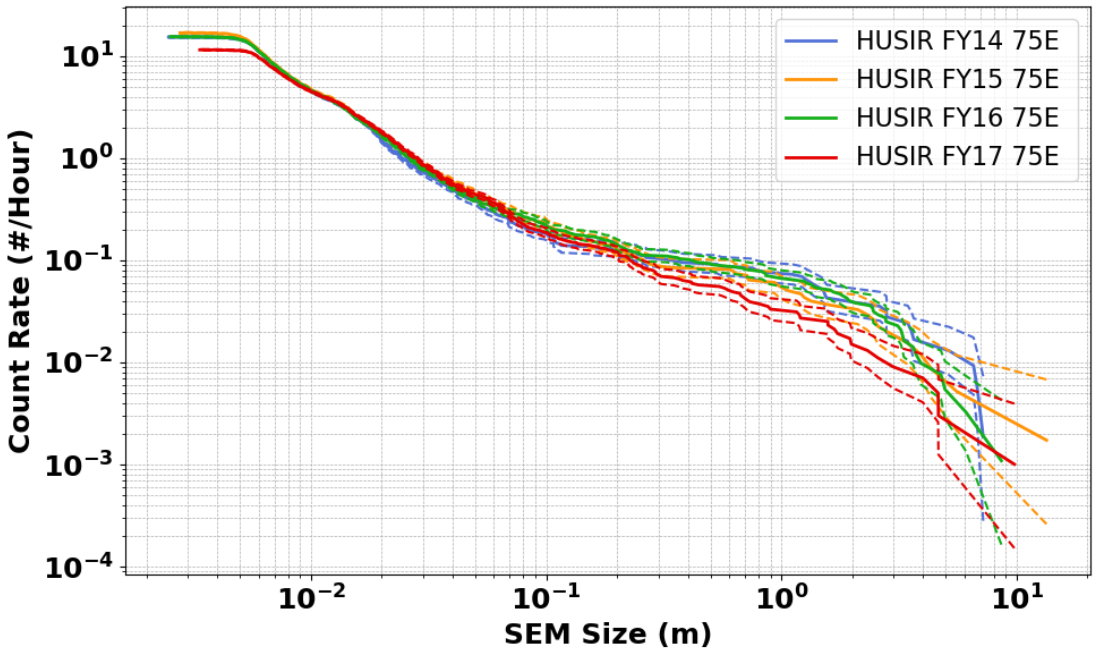

Figure 4-11. SEM-size Cumulative Distribution for all 75° elevation data by year.

5.0 Conclusion

The LEO environment was observed by the HUSIR radar and measurements from the radar were discussed and analyzed. Due to transmit power and calibration issues, HAX data was not analyzed in this report. This report covers HUSIR data for the years FY2014 - FY2017. A total of 2006 observation hours were processed and analyzed from HUSIR at 75° elevation, east-pointing; 20° elevation, south-pointing; and 10° elevation, south-pointing directions. Detected objects were measured for RCS, range, and range-rate. These data were analyzed to produce orbital altitude and inclination, size, and flux distributions.

Significant advancements in the ability to reduce and analyze data came with the radar data processing software, DRADIS, developed and used by the NASA ODPO. In the process of upgrading the software, several aspects of signal processing traditionally employed were updated as well. An artifact of historical processing associated with using 16 range gates was identified and corrected using the flexibility of DRADIS to perform detections with an arbitrary number of range gates. For the HUSIR datasets in FY2014 – FY2017, 32 gates was chosen as the new default. DRADIS also added the capability of processing RTDR-formatted data files, which are the native file format for the radars at MIT/LL, in addition to the historic CLDT format, a format which requires an additional RTDR-to-CLDT conversion process. Since the end of calendar year 2017, data delivered by MIT/LL has been and will continue to be in the RTDR format. During the testing of DRADIS, calibration sphere fly-through observations were performed – these are similar to beam-park-mode observations of orbital debris, but with calibration spheres. These were useful in characterizing DRADIS performance on objects with well-known characteristics in LEO, and are now part of the regular data products provided by MIT/LL.

New methods of visualization for orbital debris data detections were successfully employed for the discovery and removal of RFI in the radar data. Data quality control steps were implemented to ensure the removal of RFI and proper calibration of the data: (1) manual RFI review of all detections by examining the RDI plots for RFI signatures; and (2) analysis of the distribution of the range-rate detections on a day-by-day basis to remove large swathes of RFI. It was determined that the presence of RFI can inflate the measured count rates significantly and is likely contained in historical datasets. Additionally, steps to ensure proper calibration of the data were developed. This included an updated criteria for the discrimination of NaK droplets in the data, reviewing the clustering and change in slope of the count-rate or flux for RCS values near 35 dBsm (unique to the HUSIR operating frequency) as an additional calibration check, and the addition of an independent capability to reduce calibration sphere track data to verify delta RCS values provided by MIT/LL. As a result of upgrades to the process and software tools, the datasets from HUSIR in FY14 – FY17 have the appropriate pedigree to enable use in models of the orbital debris environment.

The data presented here shows the breadth and complexity of the orbital debris environment in LEO. Although this report performs a preliminary analysis of the data, new insights from the dataset are anticipated. Several known examples that bear further analysis are the origin of the 82^{o} cloud, as well as the long-term behavior and stability of the NaK population arising from initial analyses of this dataset. It is expected that these datasets will be a valuable resource for the orbital debris community.

6.0 References

1) Corley, B., "International Space Station Debris Avoidance Process," ODQN Volume 20-4, pp. 7-8.

2) Horstman, M. F., *et al*, "Haystack and HAX Radar Measurements of the Orbital Debris Environment: 2006 – 2012," NASA/TP-2014-217391, p. 3.

3) Czerwinski, M. G. and Usoff, J. M., "Development of the Haystack Ultrawideband Satellite Imaging Radar," MIT Lincoln Laboratory Journal, Volume 21, Number 1, pp. 28 – 44.

4) Lambour, R., *et al.*, Assessment of Orbital Debris Size Estimation from Radar Cross-Section Measurements, Adv. Space Res., v. 34, pp. 1013-1020, 2004.

5) "Attenuation by atmospheric gases," ITU-R, Geneva, Rec-P.676-11, 2016.

6) Dalquist, C. and Bohannon, G., "Physical Descriptions of Debris Objects Used in Static RCS Measurements," XonTech Report 910555-1978. August 1991.

7) Bohannon, G., Caampued, T., and Young, N., "First Order RCS Statistics of Hypervelocity Impact Fragments," XonTech Report 940128-BE-2305. April, 1994.

8) Barton, D. K., *et al.*, "Final Report of the Haystack Orbital Debris Data Review Panel," NASA/JSC Technical Memorandum 4809, Houston, TX, February 1998.

9) Everett, R., Caampued, T., and Chu, J., "Summary of Data Processing of September 1990 SPC Debris Data," XonTech Report 910147-1937, March 1991.

10) Everett, R., Dalquist, C., and Caampued, T., "Summary of Processing of January 1991 SPC Debris Data," XonTech Report 9100393-1965, July 1991.

11) Knott, E. F., *et al*., Radar Cross Section, Artech House, Boston, MA, 1993.

12) Xu, Y.-l and Stokely, C. L., "A Statistical Size Estimation Model for Haystack and HAX Radar Detections," 56th International Astronautical Congress, Fukuoka, Japan, 2005.

13) Vardi, Y. and Lee, D., "From Image Deblurring to Optical Investments: Maximum Likelihood Solutions for Positive Linear Inverse Problems," J. R. Statist. Soc. B 55, pp. 569-612, 1993.

14) Stokely, C. L. *et al.*, "Haystack and HAX Radar Measurements of the Orbital Debris Environment; 2003," NASA/JSC Publication JSC-62815, Houston, TX, November 2006.

15) Kessler, D. J. *et al.*, "A Search for a Previously Unknown Source of Orbital Debris; The Possibility of Coolant Leak in RORSATs," Proceedings of IAF, October 1997.

16) Grinberg, E. I., *et al.*, "Interaction of Space Debris with Liquid Metal Circuit of RORSAT Satellites," Proc. ESA, May 1997.

17) Lambour, R. and Sridharan, R., "Characteristic of an Anomalous Orbital Debris Population Inferred from Theoretical Modeling," J. of Spacecraft and Rockets, v. 36, No. 5, Sept.-Oct. 1999.

18) Hilbe, J.M., Modeling Count Data, Cambridge University Press, New York, 2014, Chapters 5 and 8.

19) Stokely, C. L. Benbrook, J. R. and Horstman, M., "On the Determination of Poisson Statistics for Haystack Radar Observations of Orbital Debris," Proceedings of the 58th International Astronautical Congress, 2007, pp. 1743 – 1750.

20) Johnson, N. L. Kemp, A. W. and Kotz, S., Univariate Discrete Distributions, 3rd Edition, Wiley, New Jersey, 2005, pp. 176 - 177

Appendix A: Uncertainty in Reported Counts

Count data from orbital debris measurement sources are assumed to follow a Poisson distribution, and Poisson-based empirical standard errors are reported with respect to uncertainty in the count values. Implicit in the assumption of a Poisson model is a constant count rate, as well as counts that occur one-at-a-time. To date, test of this model for overdispersion or underdispersion with respect to the data on a year-by-year basis has not been conducted, which would have the effect of adjusting the reported empirical standard error slightly – if the data more appropriately follows a negative binomial (overdispersed case) or the less frequently observed, generalized Poisson model (underdispersed case) [18]. Past efforts, however, have considered whether the assumptions related to use of a Poisson model are met for radar observations made by the Haystack radar [19], with good agreement with the use of this distribution obtained.

Consider the definition of the Poisson distribution, defined in Equation A-1 below. Debris counts, *k*, are assumed to follow a Poisson distribution with mean λ. The Poisson model is a single parameter model, and the variance is equal to λ as well. Figure A-1 shows several Poisson distributions with varying values for λ.

$$k \sim \text{Poisson}(\lambda) = e^{-\lambda}\frac{\lambda^k}{k!} \qquad \text{A-1}$$

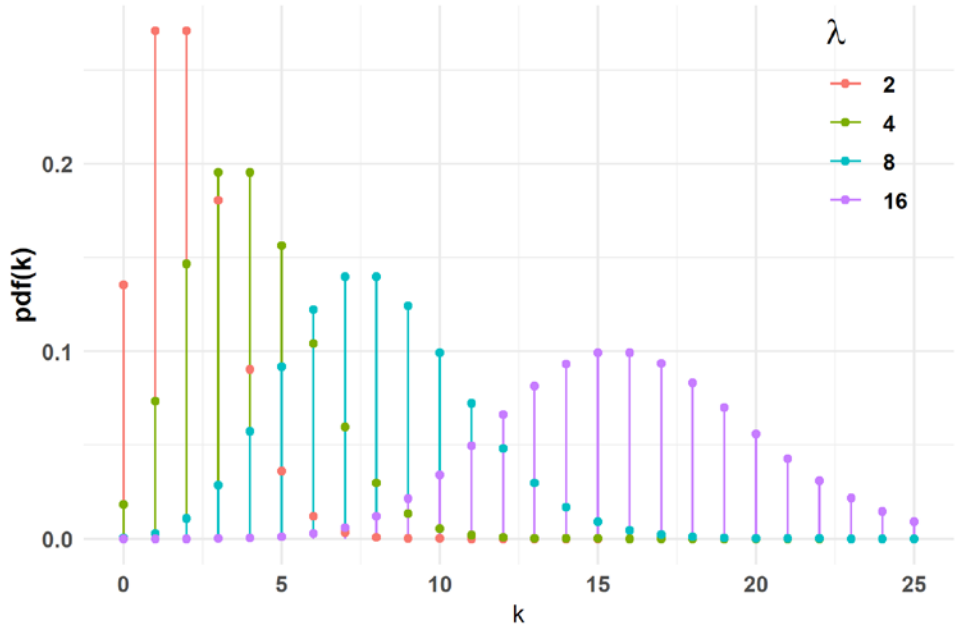

Figure A-1. Poisson distributions with λ = 2, 4, 6, 8, and 16.

The Poisson model may be rewritten in terms of the count rate as shown in Equation A-2. In this case, *r*, is the count rate and *T* is the observation time for the radar.

$$\mathrm{kT} \sim \mathrm{Poisson}(\mathrm{rT}) = e^{-\mathrm{rT}} \frac{(\mathrm{rT})^k}{k!} \qquad \text{A-2}$$

For observations arising from a Poisson distribution, empirical standard errors are calculated in a similar manner to standard errors derived from a standard normal distribution. The upper and lower bounds are determined based on their cumulative probabilities, and are such that the probability between the upper and lower points is approximately 68.2%. This is depicted in Figure A-2, where the upper and lower points are located at ± σ, which for a standard normal distribution is ± 1.

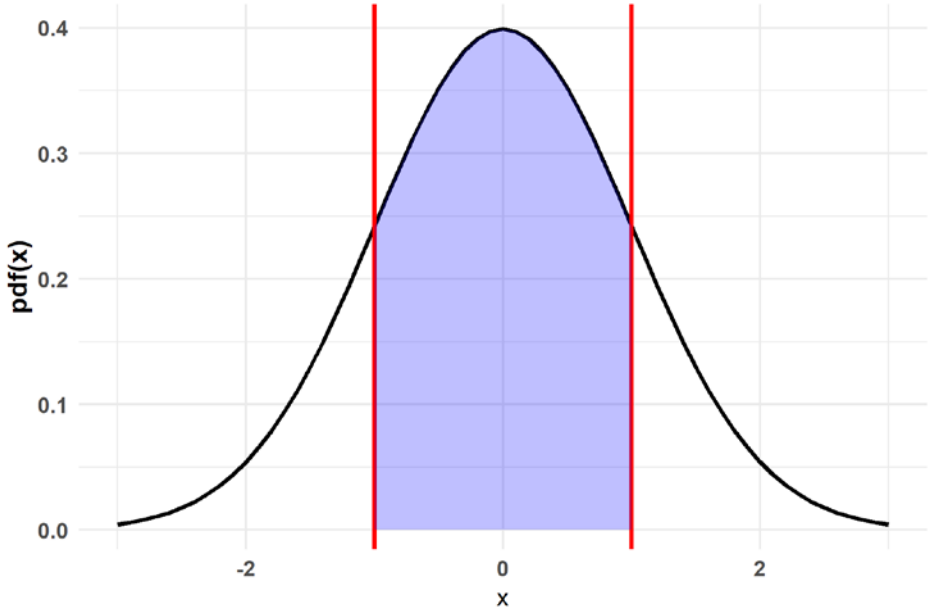

Figure A-2. Standard normal distribution with the area between ±σ highlighted.

The lower and upper values of the empirical standard errors for the Poisson distribution may be equivalently found using quantiles calculated from a Gamma distribution with shape parameters k and k+1 as shown in Equation A-3, and with scale parameter equal to 1. Alternately, the use of the quantile function for a chi-squared distribution, as shown in Equation A-4, may be used since the chi-squared distribution is a special case of the Gamma distribution [20].

$$F^{-1}(\alpha/2\,;k;1) \leq \lambda \leq F^{-1}(1-\alpha/2\,;k+1;1) \qquad \text{A-3}$$

$$\frac{1}{2}\chi^2(\alpha/2\,;2k) \leq \lambda \leq \frac{1}{2}\chi^2(1-\alpha/2\,;2k+2) \qquad \text{A-4}$$

Empirical standard errors calculated in this way for count values for the first ten counts are shown in Table A-1. Also included in Table A-1 are the upper and lower limits for the 95% ($\alpha = 0.05$) confidence intervals calculated with the same methodology. In showing comparisons between measured data in this report, use of a more restrictive "1-σ" limit is used for error bars in plots, rather than the less restrictive 95% confidence limits.

Table A-1: Lower and Upper Standard Errors for Observed Counts, k. The 95% Confidence Interval, α=0.05, is Included in the Last Two Columns

k	*lower*	*upper*	*α /2*	*1- α /2*
1	0.1727538	1.841022	0.02531781	3.688879
2	0.7081854	3.299527	0.24220928	5.571643
3	1.3672953	4.637860	0.61867212	7.224688
4	2.0856608	5.918186	1.08986537	8.767273
5	2.8403089	7.162753	1.62348639	10.241589
6	3.6200686	8.382473	2.20189425	11.668332
7	4.4185295	9.583642	2.81436305	13.059474
8	5.2316139	10.770281	3.45383218	14.422675
9	6.0565390	11.945142	4.11537310	15.763189
10	6.8913056	13.110204	4.79538870	17.084803

It should be noted that the relation in Equation A-4 produces approximate confidence limits with respect to a given α value, which is due to the discrete nature of the underlying distribution – a well-known issue [20] – and especially true for low counts. As a result, better behavior may be obtained by adjusting the upper point to have fewer degrees of freedom, 2*k* versus 2*k*+2. A comparison between the two methods and the interior probability obtained using two different methods are shown in Figures A-3 and A-4. Note that for larger values of *k*, both results asymptotically approach the 68.2% interior probability, shown as a red horizontal line, associated with ± σ for a normal distribution. The method where fewer degrees of freedom are used for the upper bound produces interior probabilities that oscillate around the 68.2% line for even and odd values of *k* and is generally closer to this value after the first few values of *k*, whereas the higher degrees of freedom asymptotically approaches 68.2% from above.

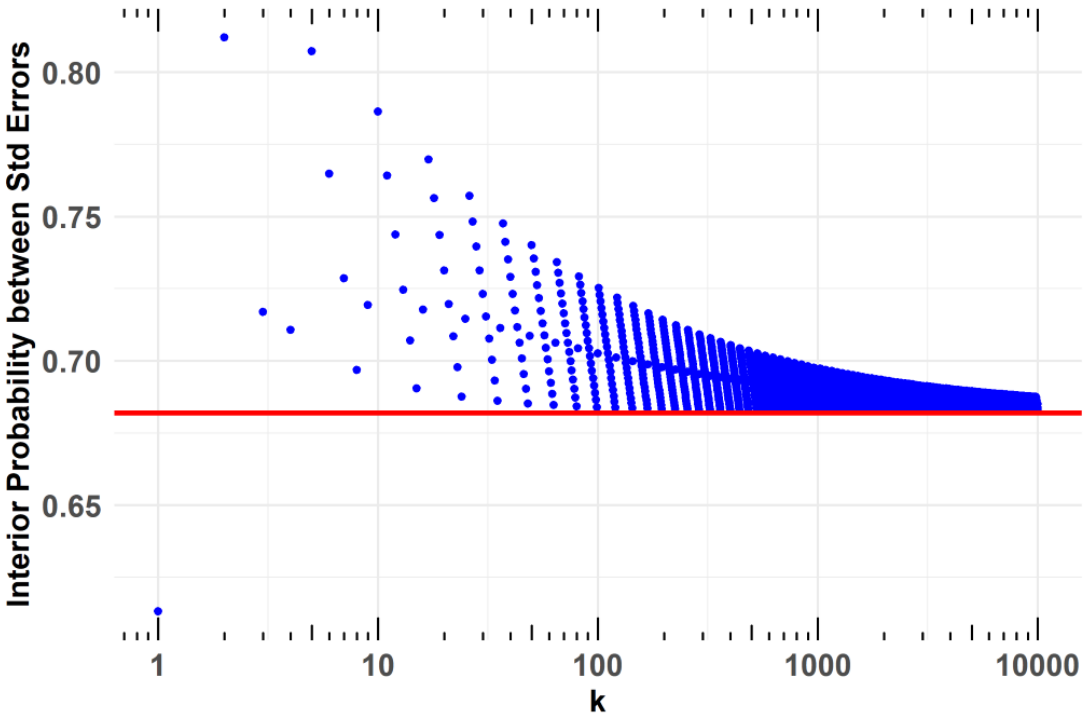

Figure A-3. Interior probabilities between standard errors calculated with an upper limit using $2k + 2$ degrees of freedom.

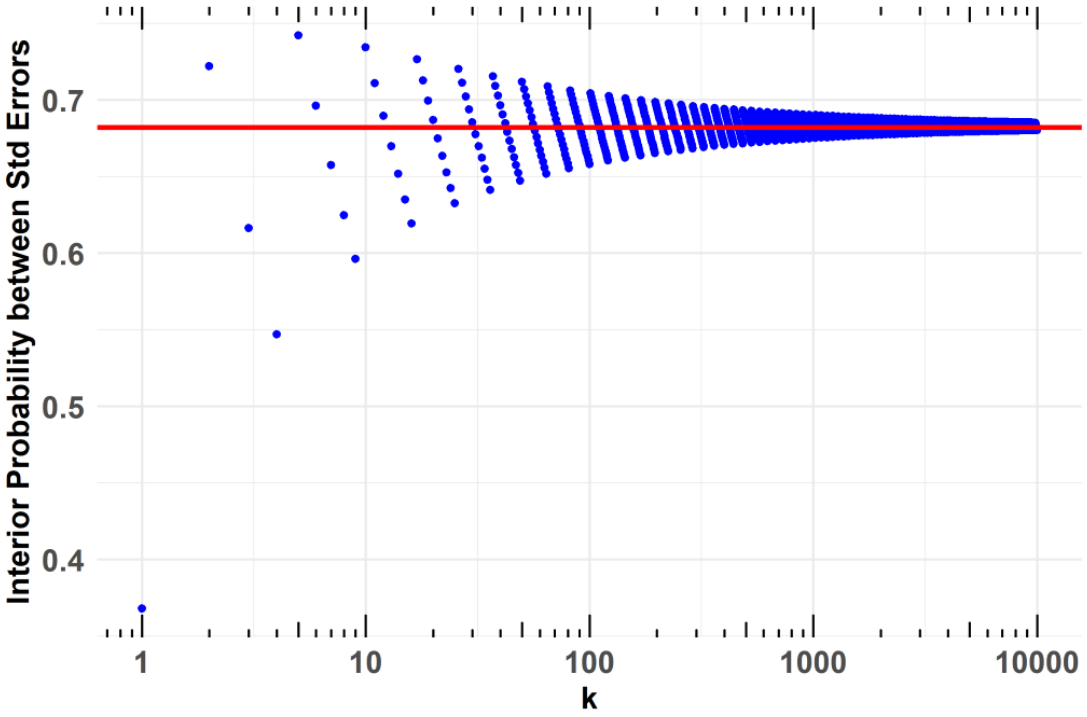

Figure A-4. Interior probabilities between standard errors calculated with an upper limit using $2k$ degrees of freedom.

Appendix B: Total Number of Hours Received from MIT/LL

Table B-1: Data Collection Summary Reflecting the Total Number of Observation Hours Received from MIT/LL

Fiscal Year	75° East	20° South	10° South	Total Received	Total Retained
	Hours of Observation	Hours of Observation	Hours of Observation	Hours of Observation	Hours of Observation
2014	272.5	0.0	67.8	340.3	325.4
2015	468.8	89.6	110.6	669.0	441.7
2016	573.1	142.8	139.8	855.7	740.9
2017	575.7	1.2	0.5	577.4	497.9

Appendix C: HUSIR 75° Elevation, East Pointing

C.1. RANGE VERSUS RANGE-RATE

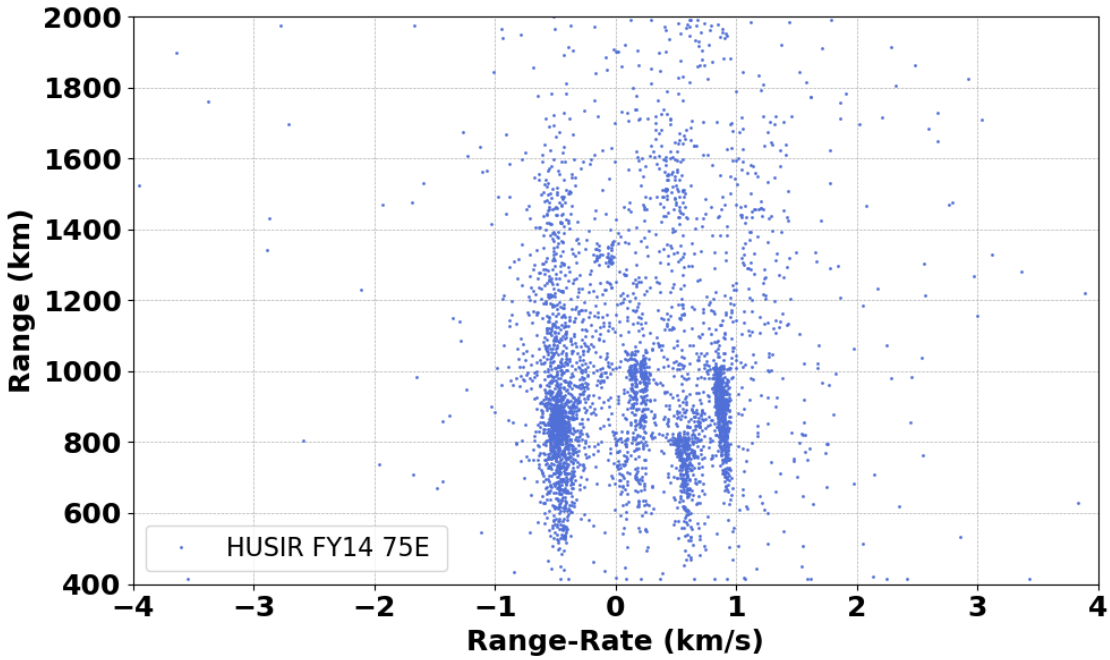

Figure C-1. Range versus Range-Rate, HUSIR 75° east, FY2014.

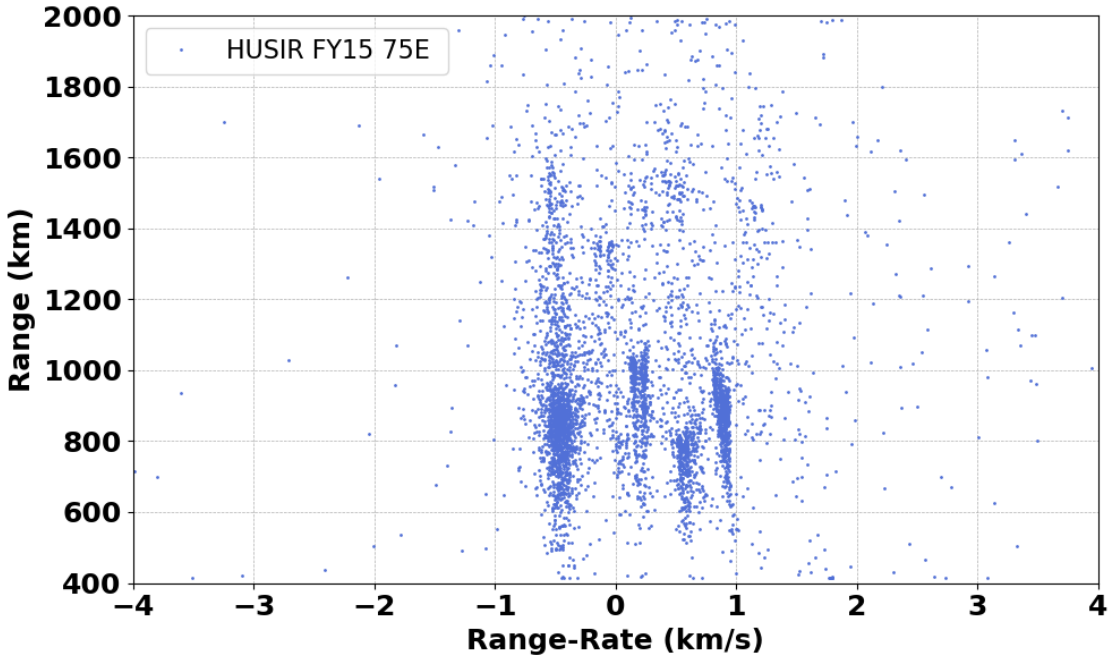

Figure C-2. Range versus Range-Rate, HUSIR 75° east, FY2015.

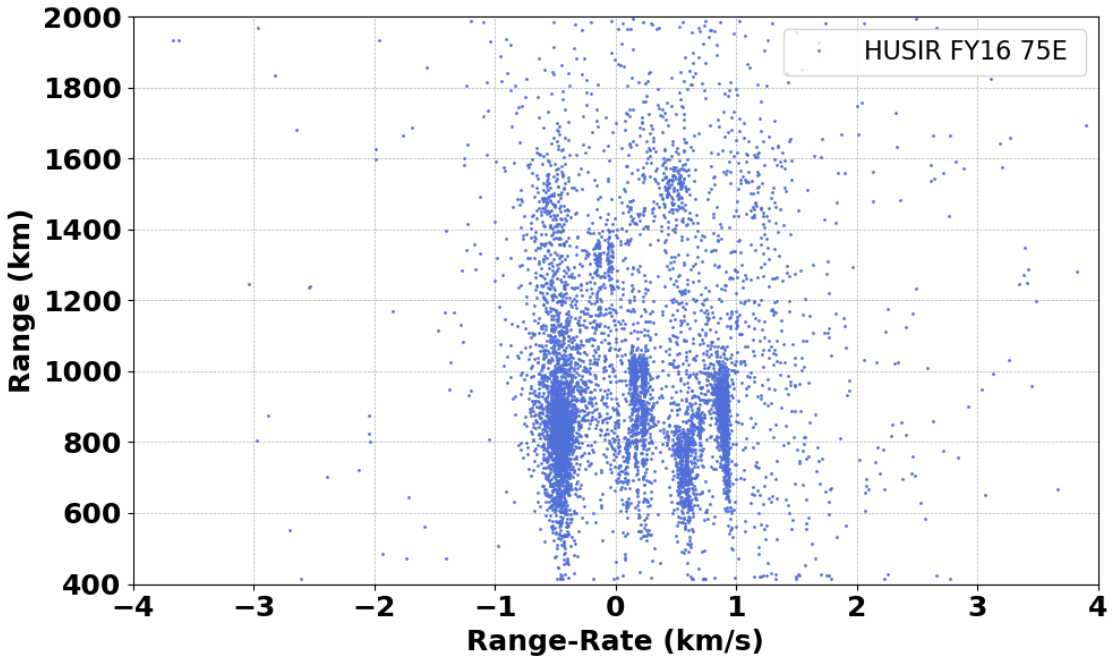

Figure C-3. Range versus Range-Rate, HUSIR 75° east, FY2016.

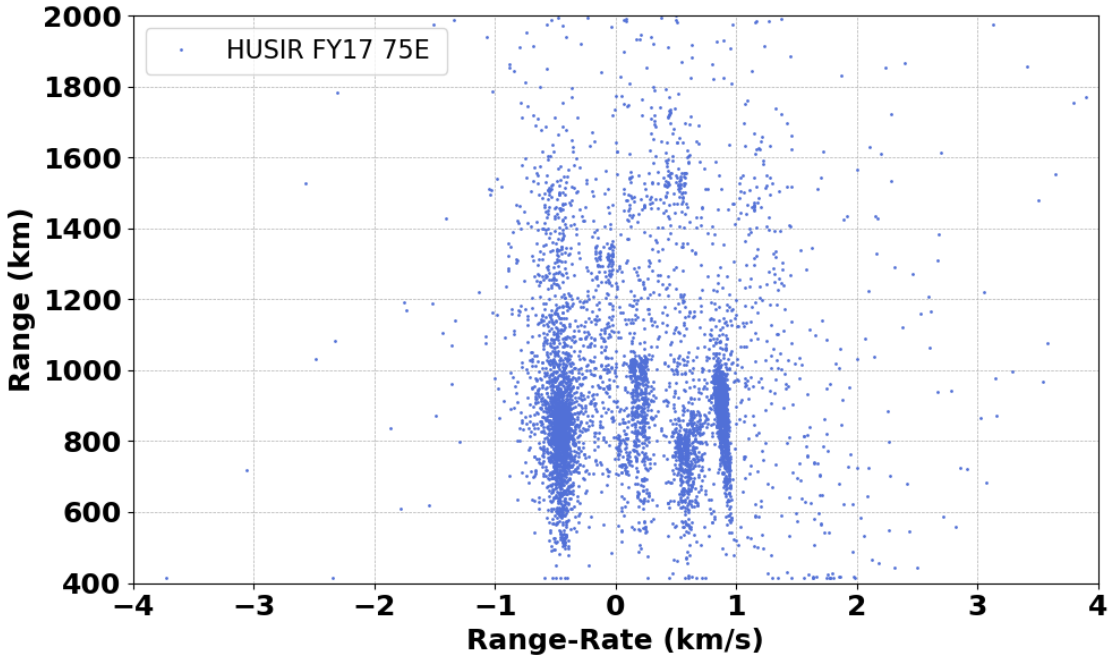

Figure C-4. Range versus Range-Rate, HUSIR 75° east, FY2017.

C.2. ALTITUDE VERSUS INCLINATION

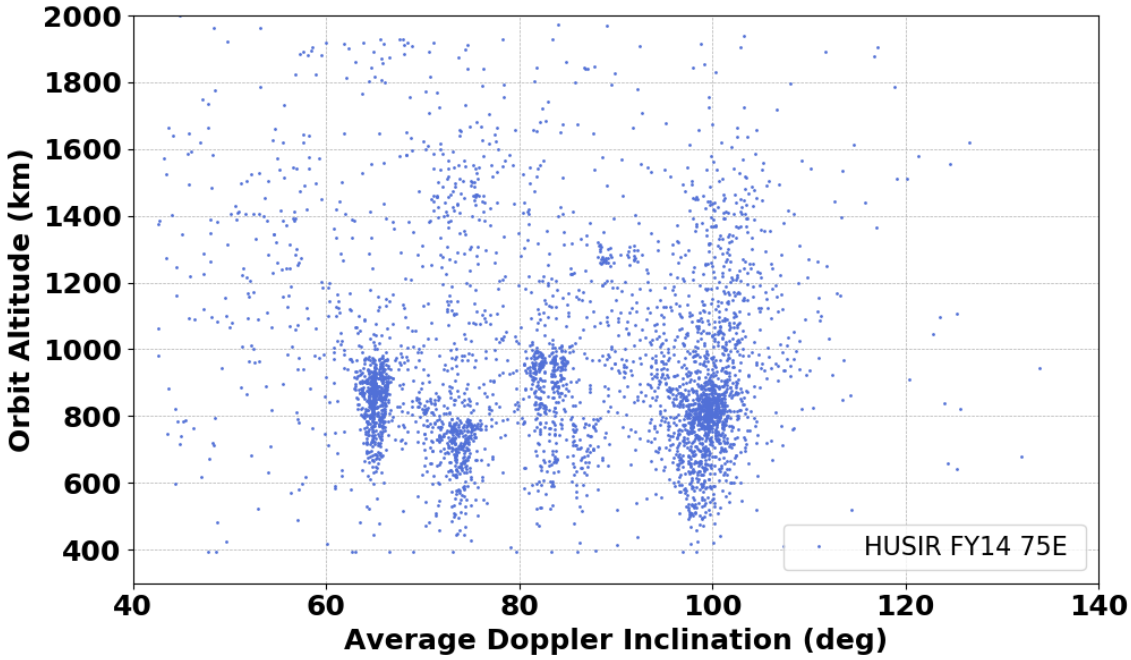

Figure C-5. Altitude versus orbital inclination, HUSIR 75° east, FY2014. Inclination derived from Range-Rate assuming a circular orbit.

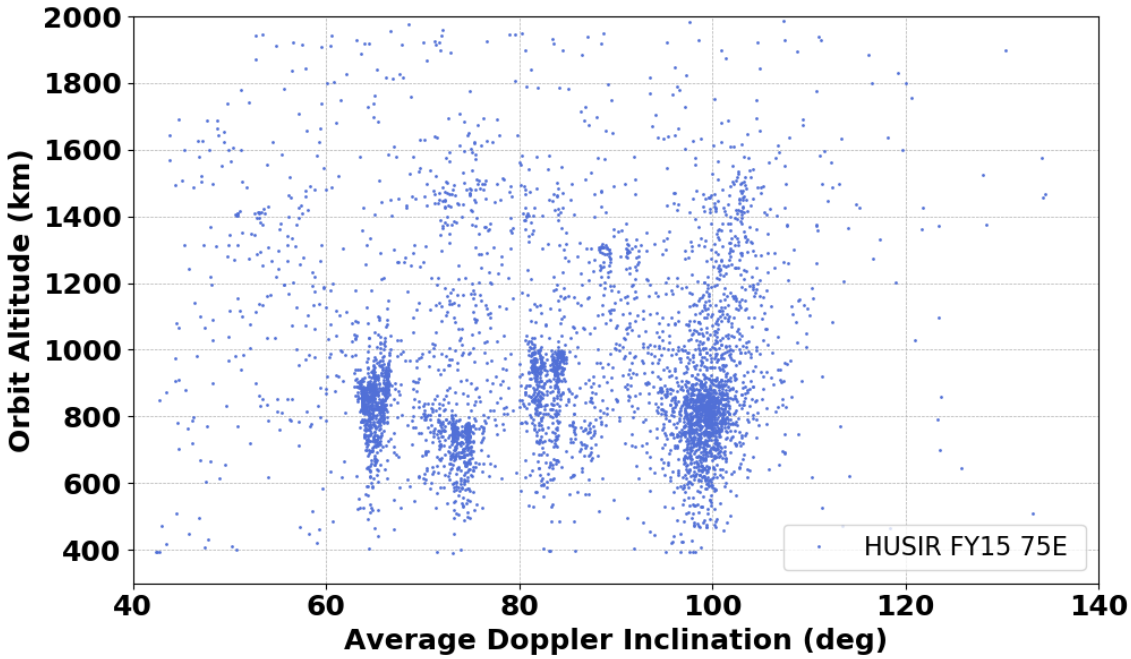

Figure C-6. Altitude versus orbital inclination, HUSIR 75° east, FY2015. Inclination derived from Range-Rate assuming a circular orbit.

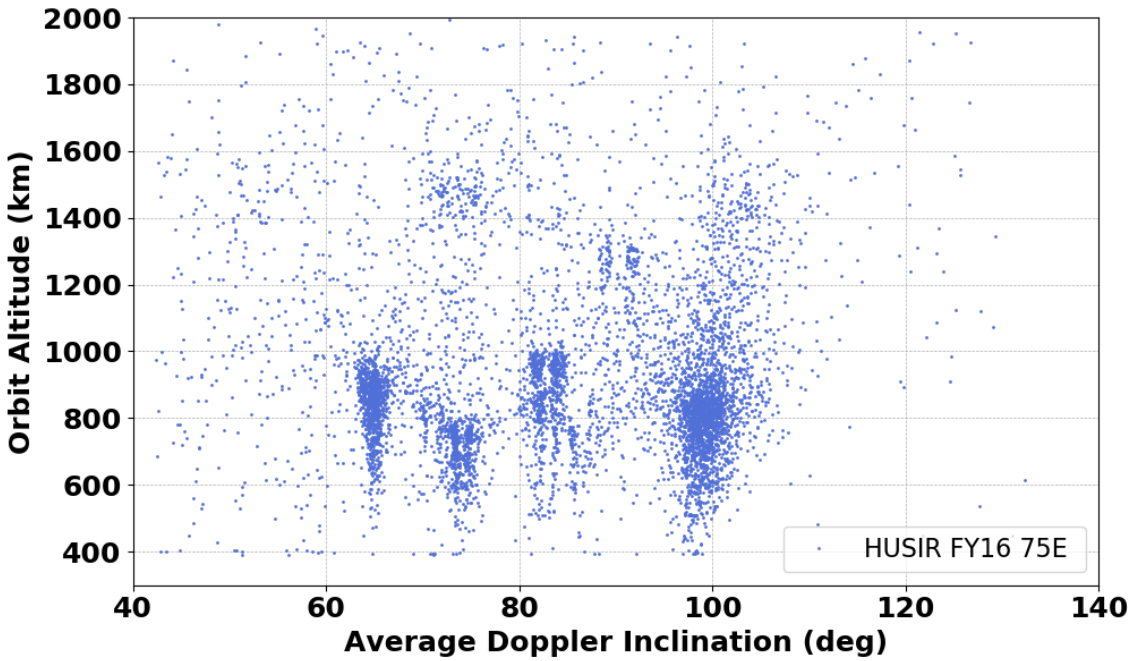

Figure C-7. Altitude versus orbital inclination, HUSIR 75° east, FY2016. Inclination derived from Range-Rate assuming a circular orbit.

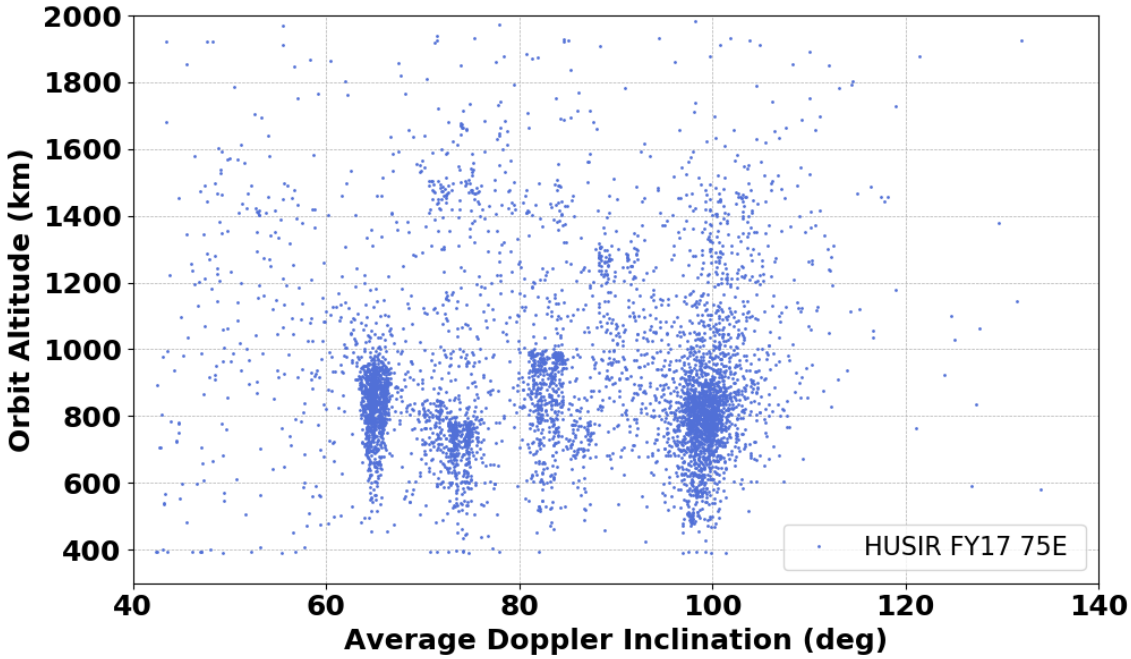

Figure C-8. Altitude versus orbital inclination, HUSIR 75° east, FY2017. Inclination derived from Range-Rate assuming a circular orbit.

C.3. RANGE VERSUS RADAR CROSS SECTION

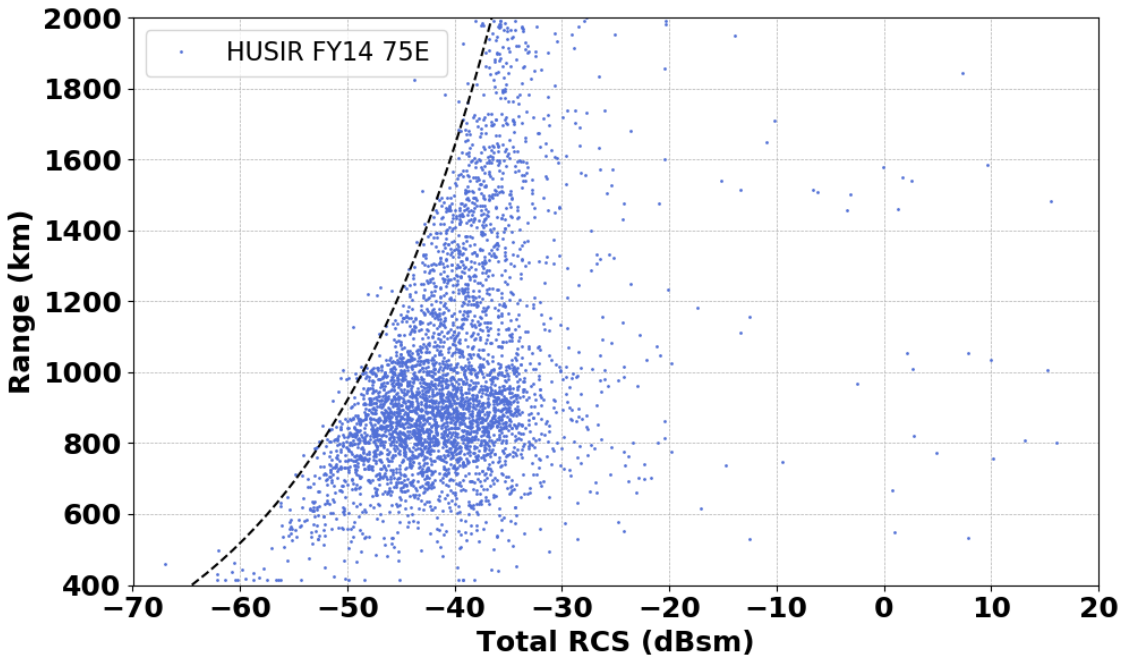

Figure C-9. Range versus Radar Cross Section, HUSIR 75° east, FY2014.

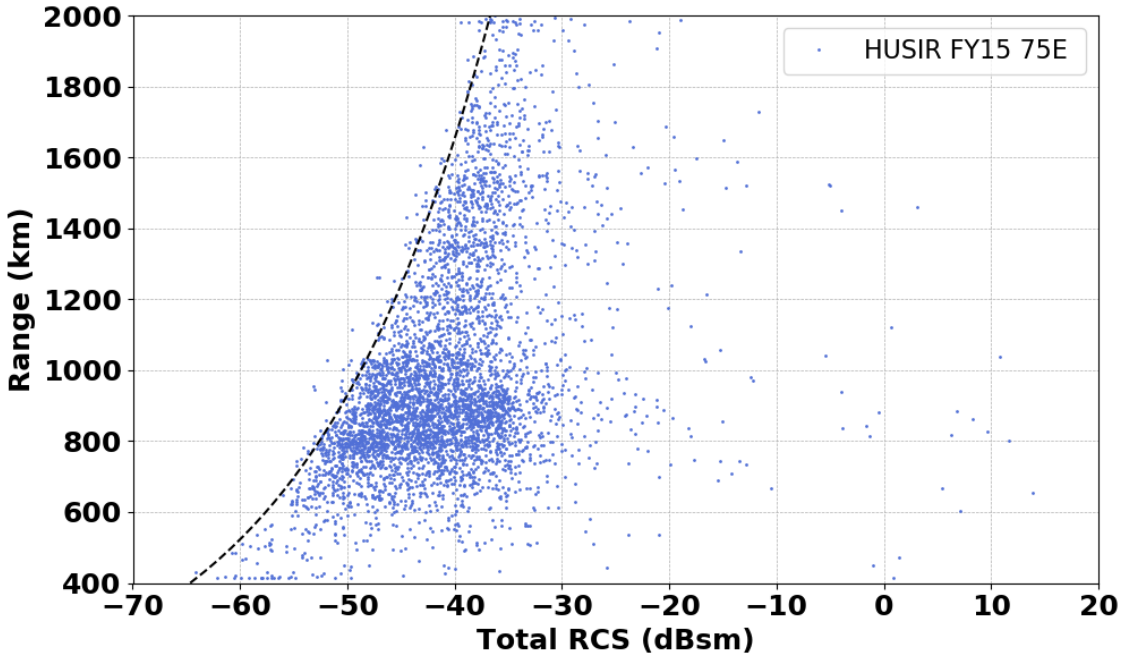

Figure C-10. Range versus Radar Cross Section, HUSIR 75° east, FY2015.

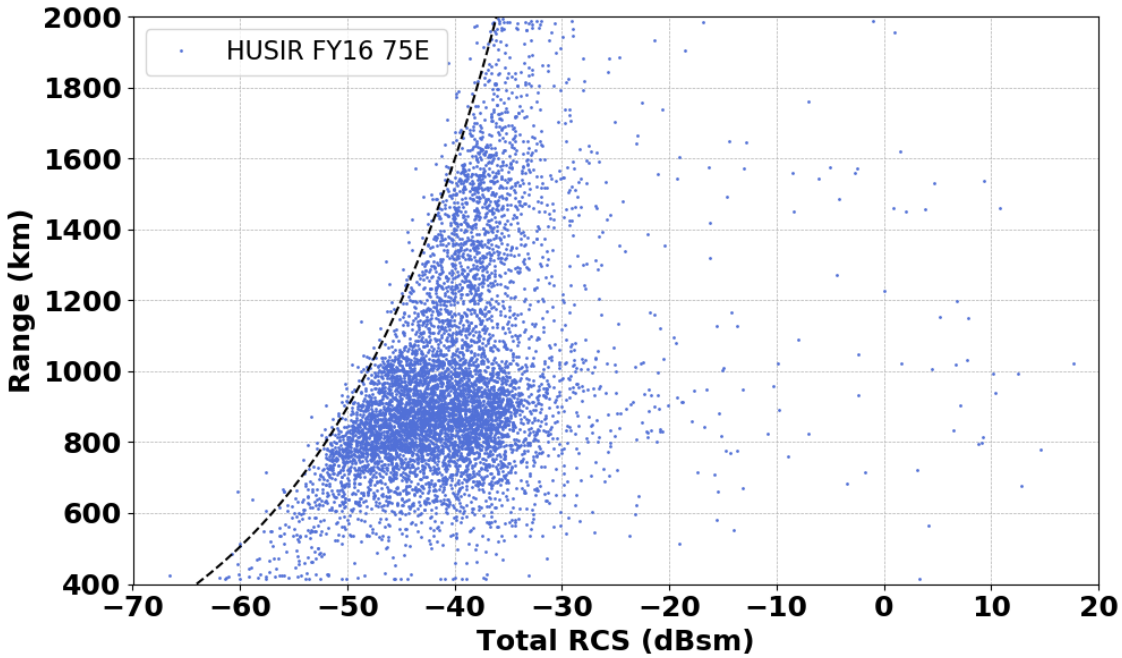

Figure C-11. Range versus Radar Cross Section, HUSIR 75° east, FY2016.

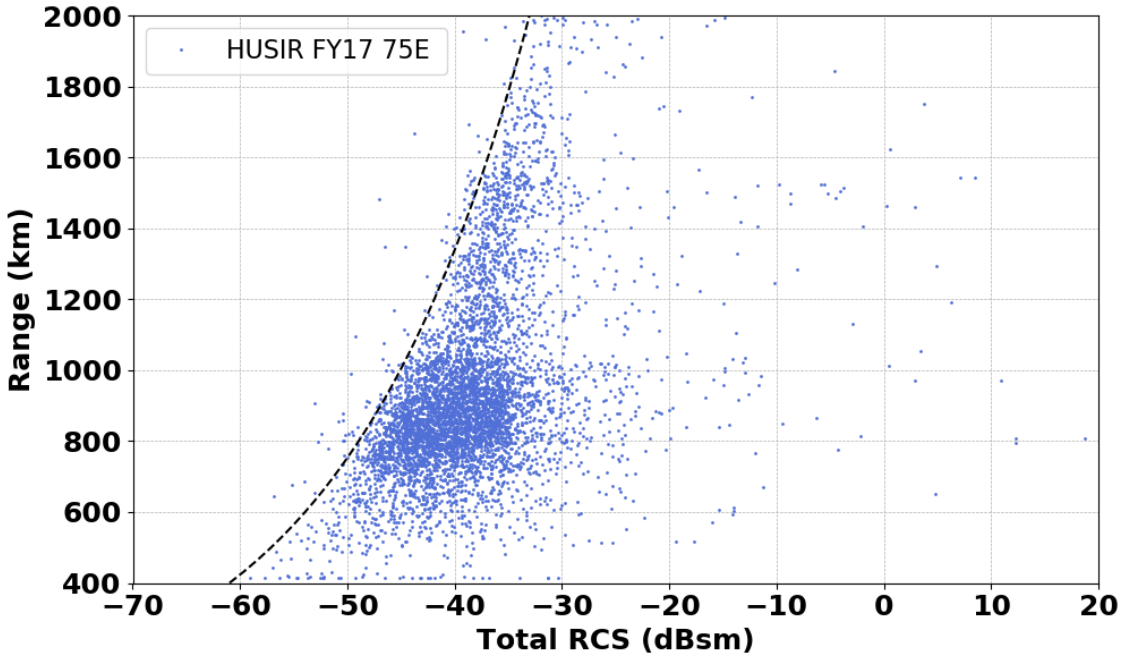

Figure C-12. Range versus Radar Cross Section, HUSIR 75° east, FY2017.

C.4. CUMULATIVE DETECTION RATE VERSUS SEM SIZE

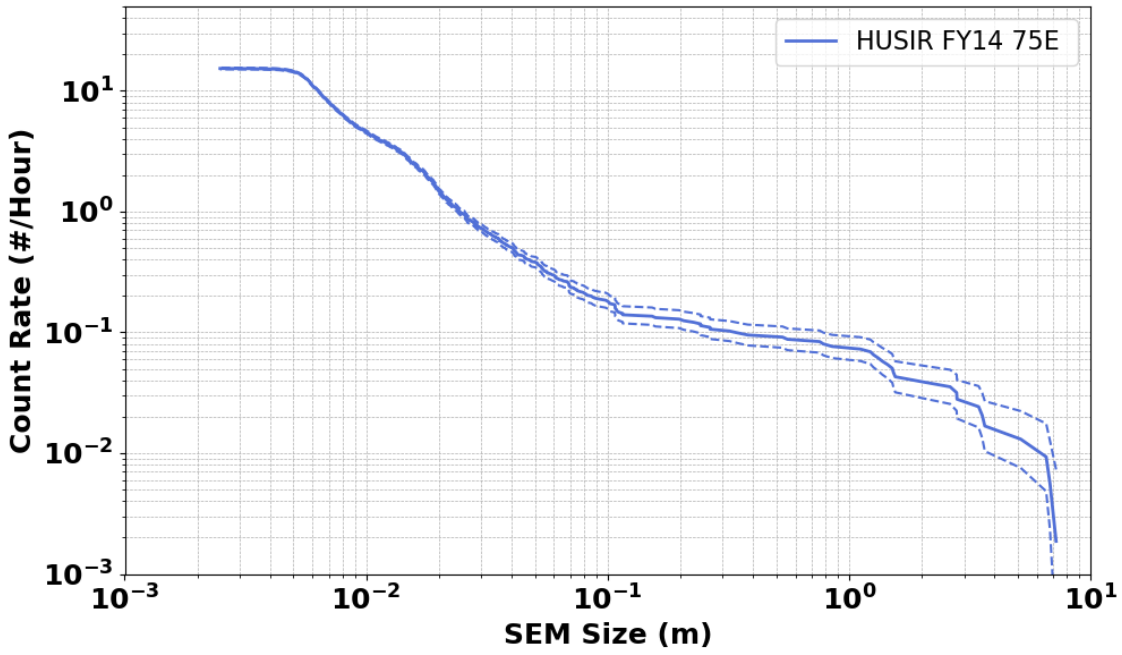

Figure C-13. Cumulative count rate versus SEM Size, HUSIR 75° east, FY2014.

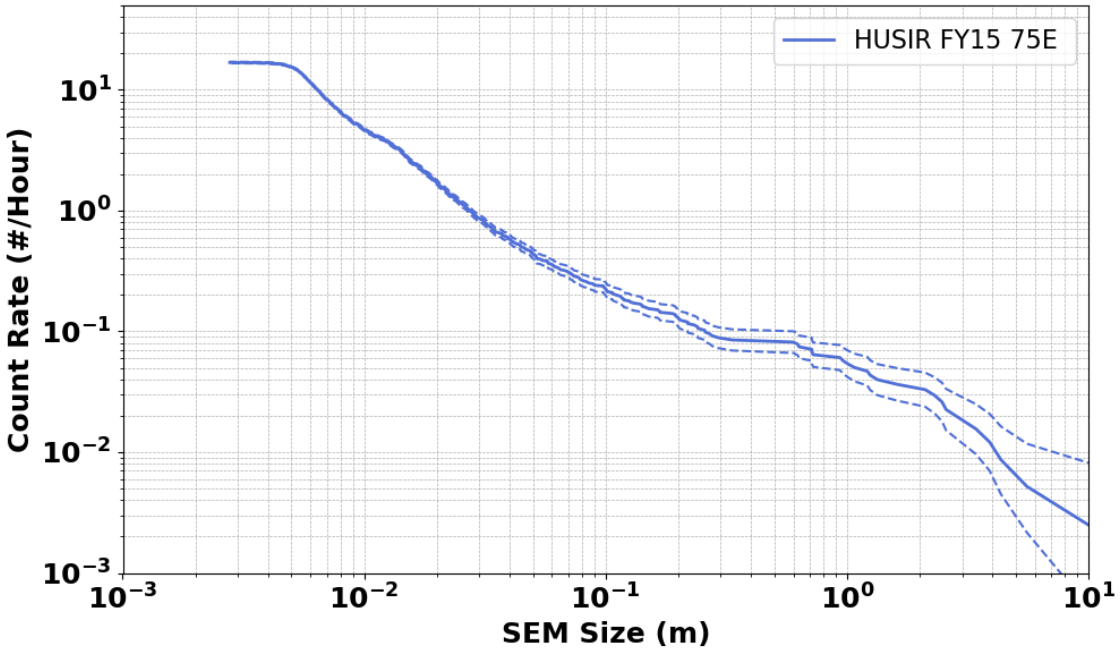

Figure C-14. Cumulative count rate versus SEM size, HUSIR 75° east, FY2015.

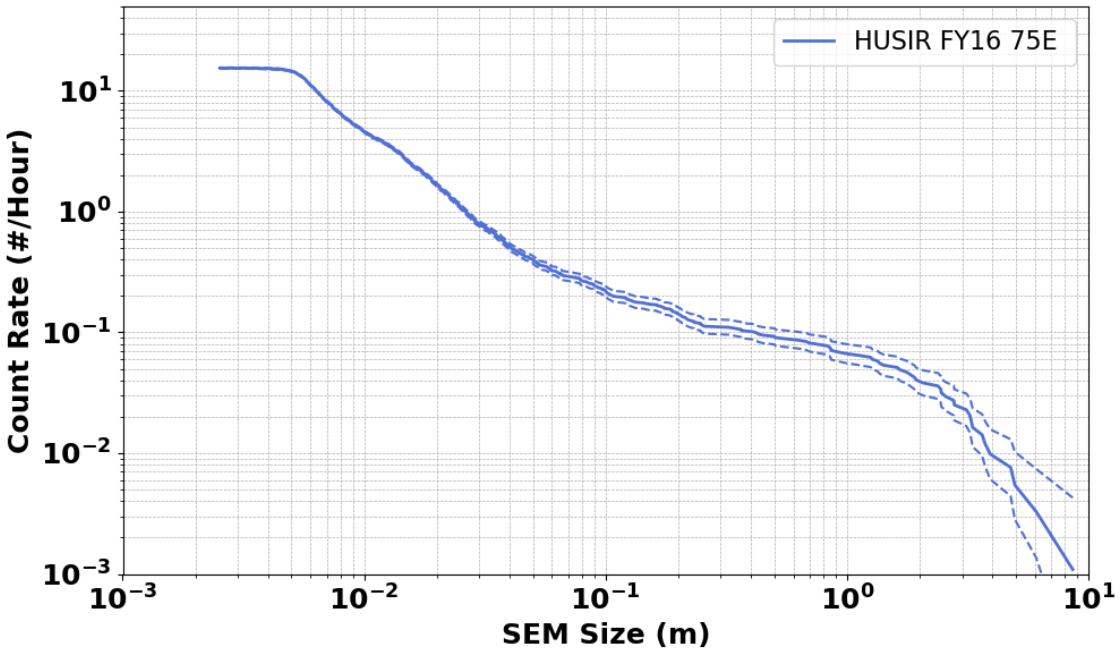

Figure C-15. Cumulative count rate versus SEM size, HUSIR 75° east, FY2016.

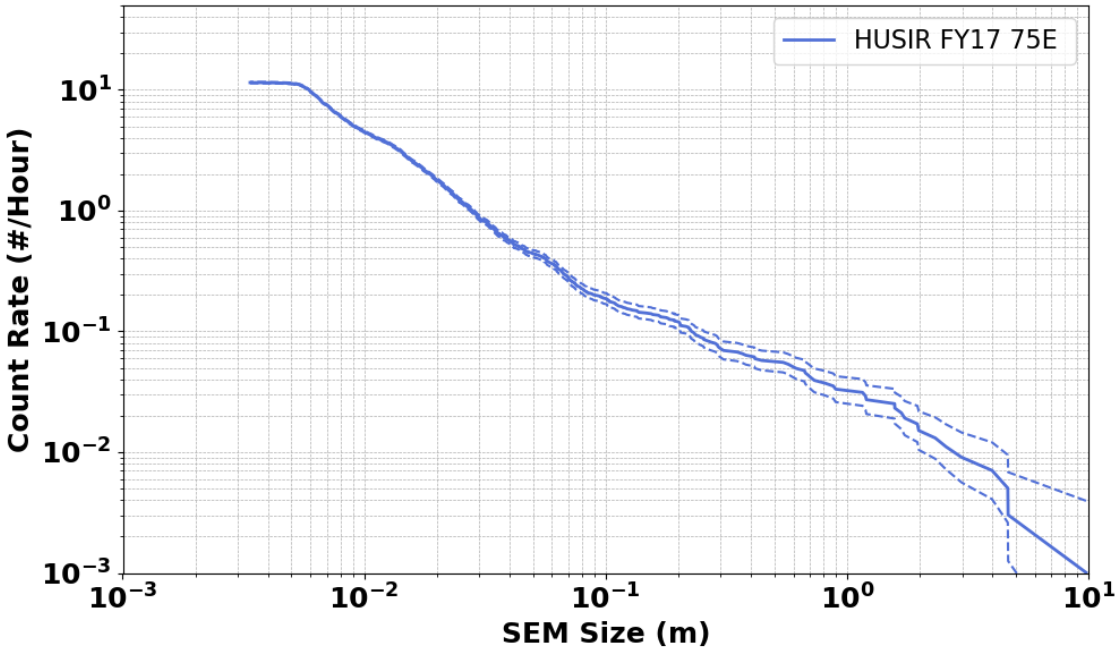

Figure C-16. Cumulative count rate versus SEM size, HUSIR 75° east, FY2017.

C.5. CUMULATIVE DETECTION RATE VERSUS PP SNR

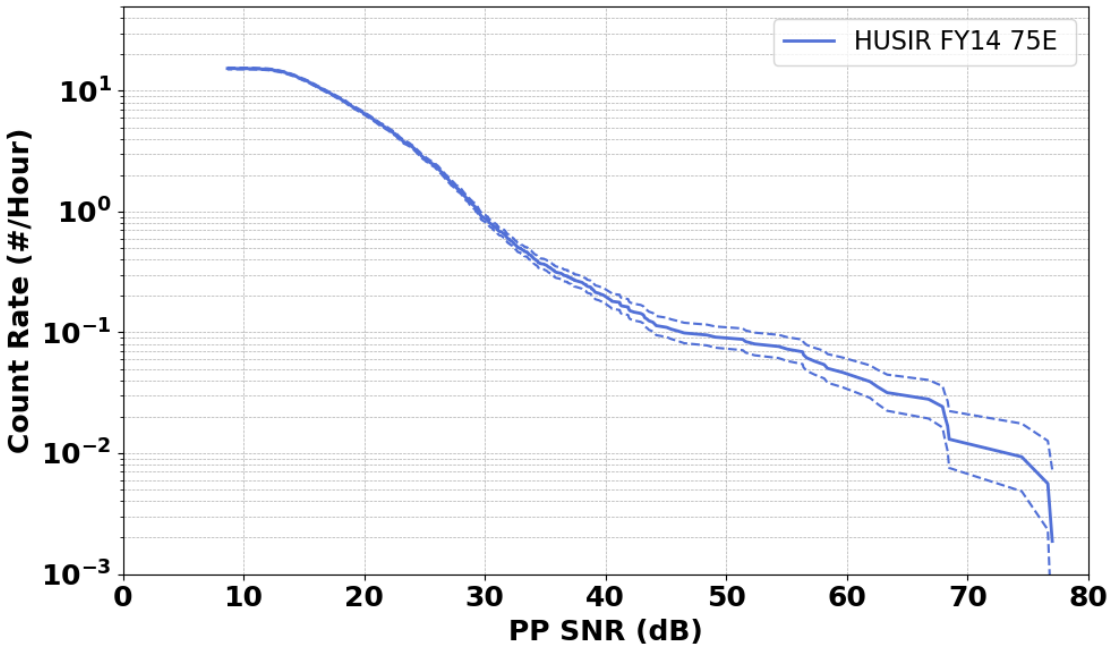

Figure C-17. Cumulative count rate versus detection SNR of the principle polarization, HUSIR 75° east, FY2014.

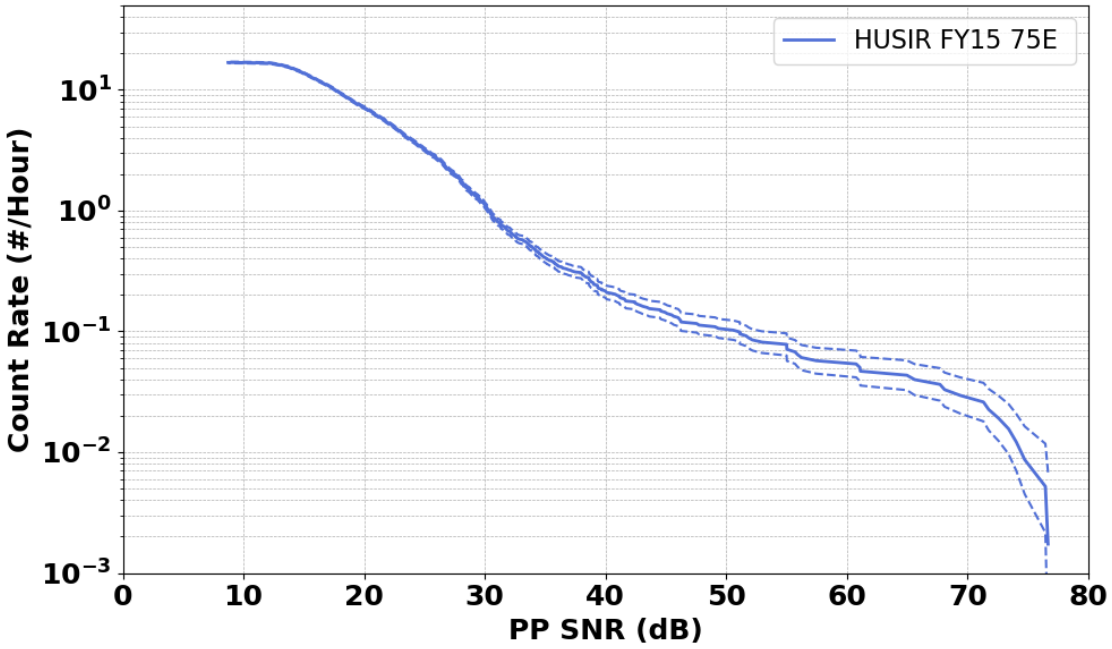

Figure C-18. Cumulative count rate versus detection SNR of the principle polarization, HUSIR 75° east, FY2015.

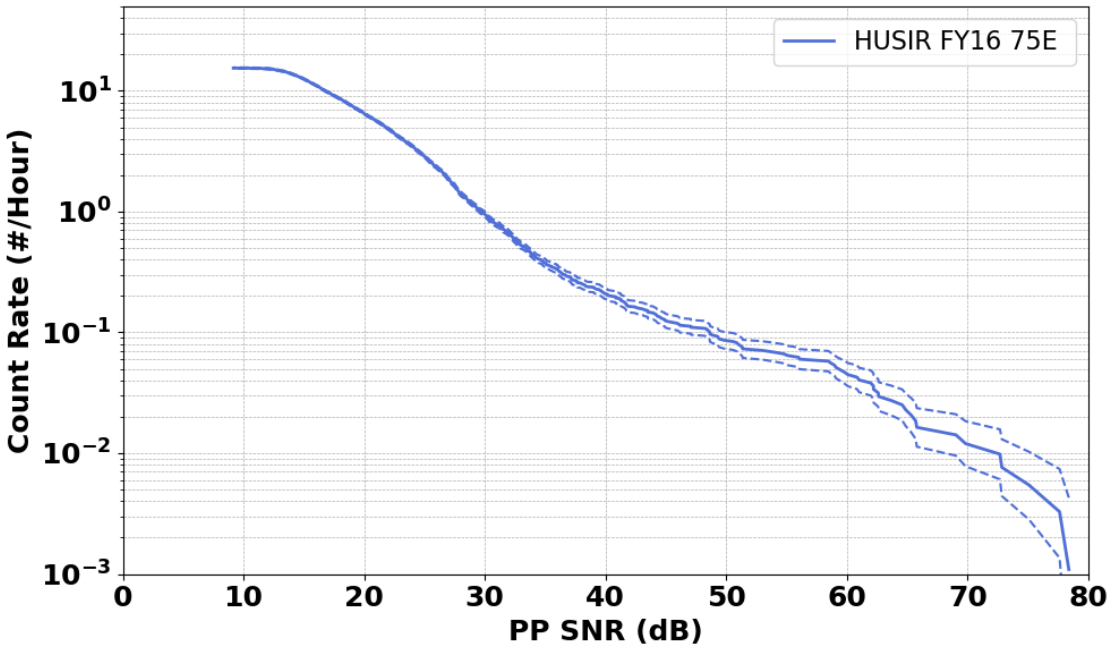

Figure C-19. Cumulative count rate versus detection SNR of the principle polarization, HUSIR 75° east, FY2016.

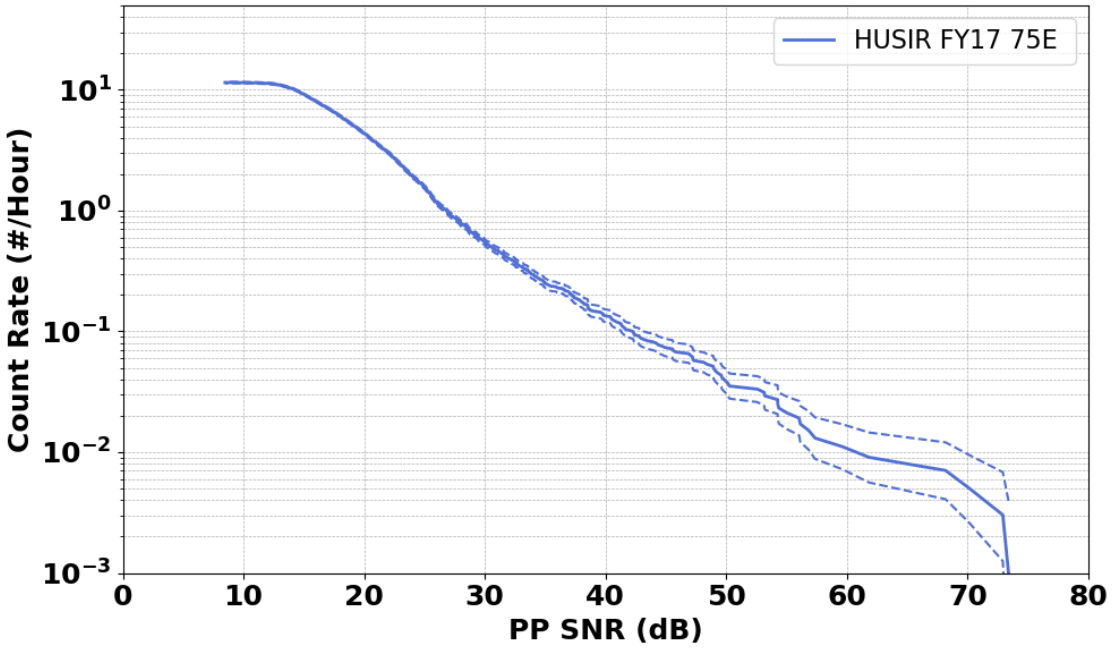

Figure C-20. Cumulative count rate versus detection SNR of the principle polarization, HUSIR 75° east, FY2017.

C.6. CUMULATIVE DETECTION RATE VERSUS RADAR CROSS SECTION

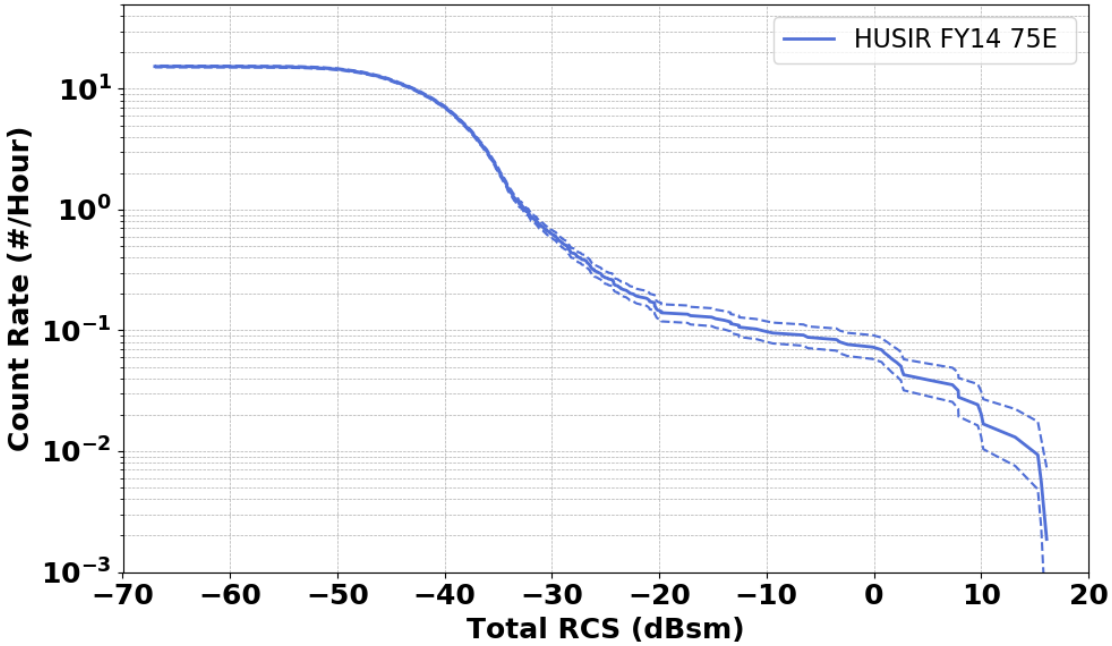

Figure C-21. Cumulative count rate versus Total Radar Cross Section, HUSIR 75° east, FY2014.

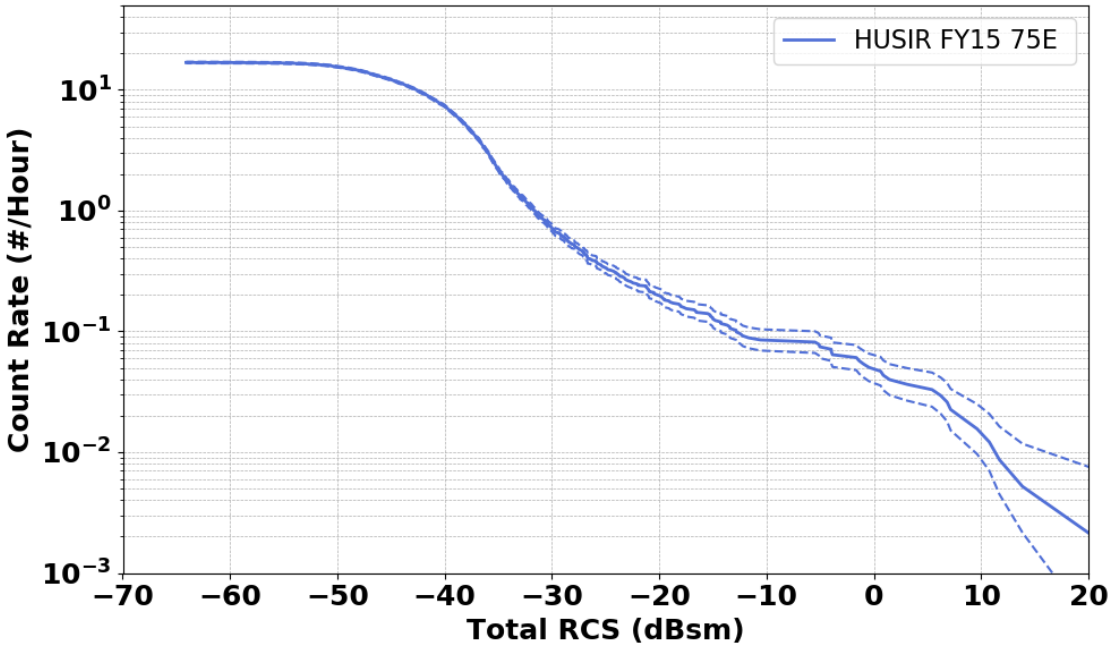

Figure C-22. Cumulative count rate versus Total Radar Cross Section, HUSIR 75° east, FY2015.

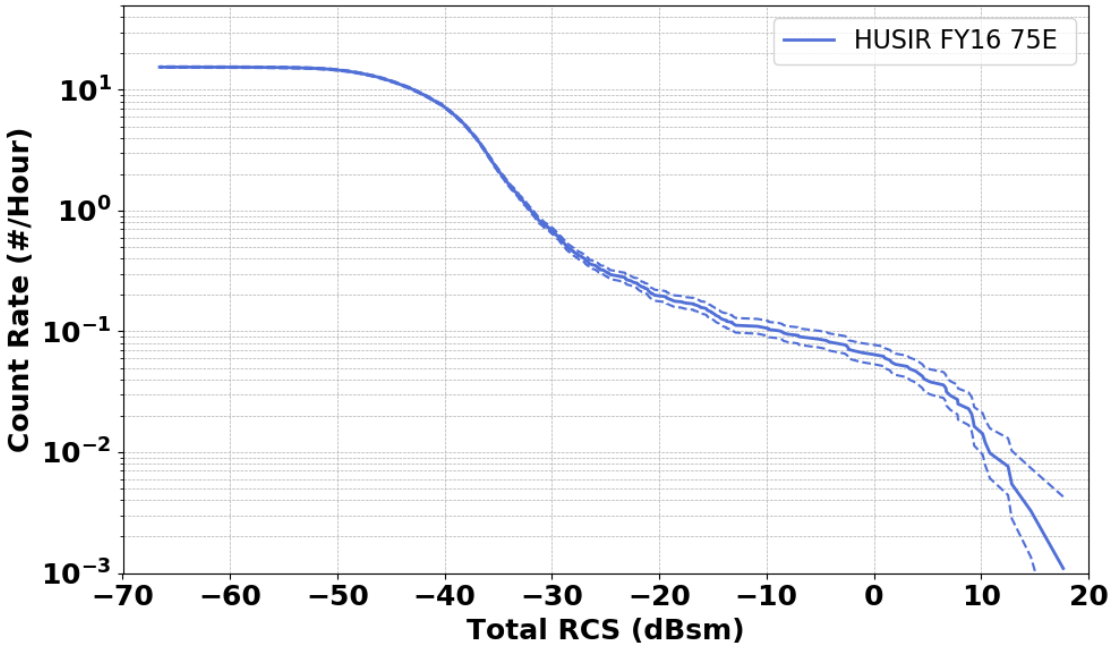

Figure C-23. Cumulative count rate versus Total Radar Cross Section, HUSIR 75° east, FY2016.

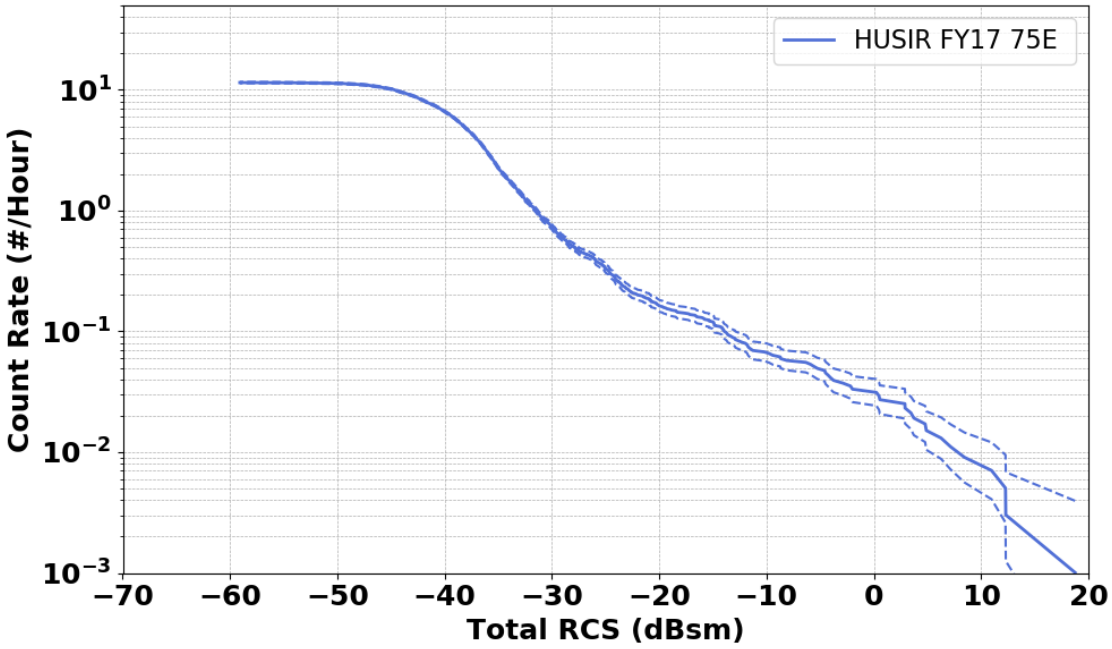

Figure C-24. Cumulative count rate versus Total Radar Cross Section, HUSIR 75° east, FY2017.

C.7. POLARIZATION RATIO DISTRIBUTION

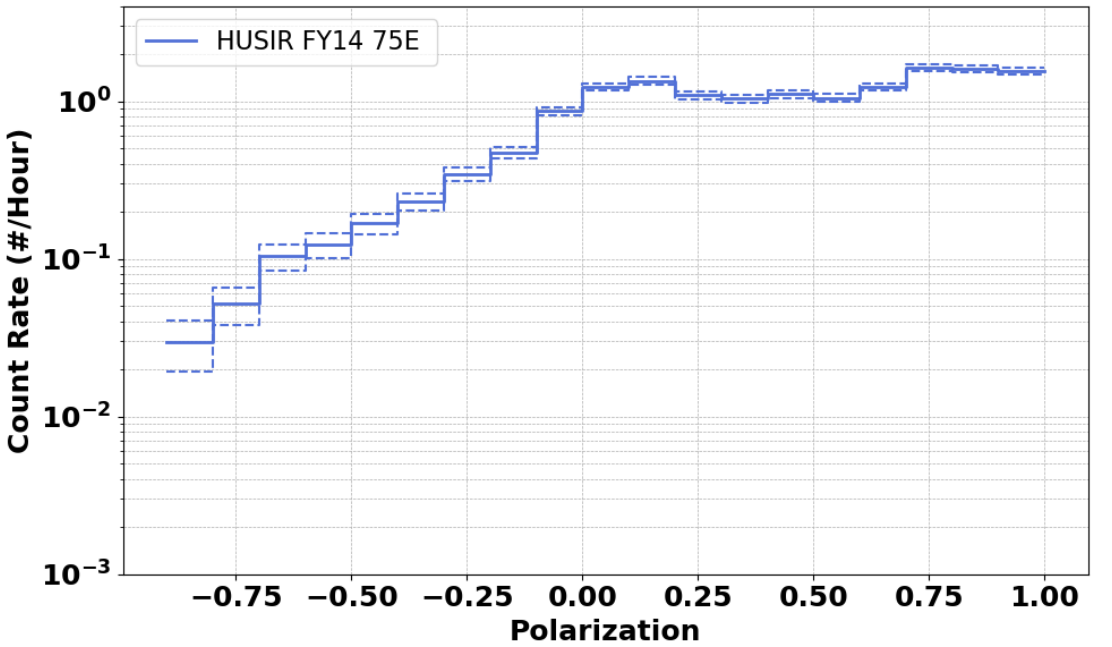

Figure C-25. Count Rate versus polarization ratio, HUSIR 75° east, FY2014.

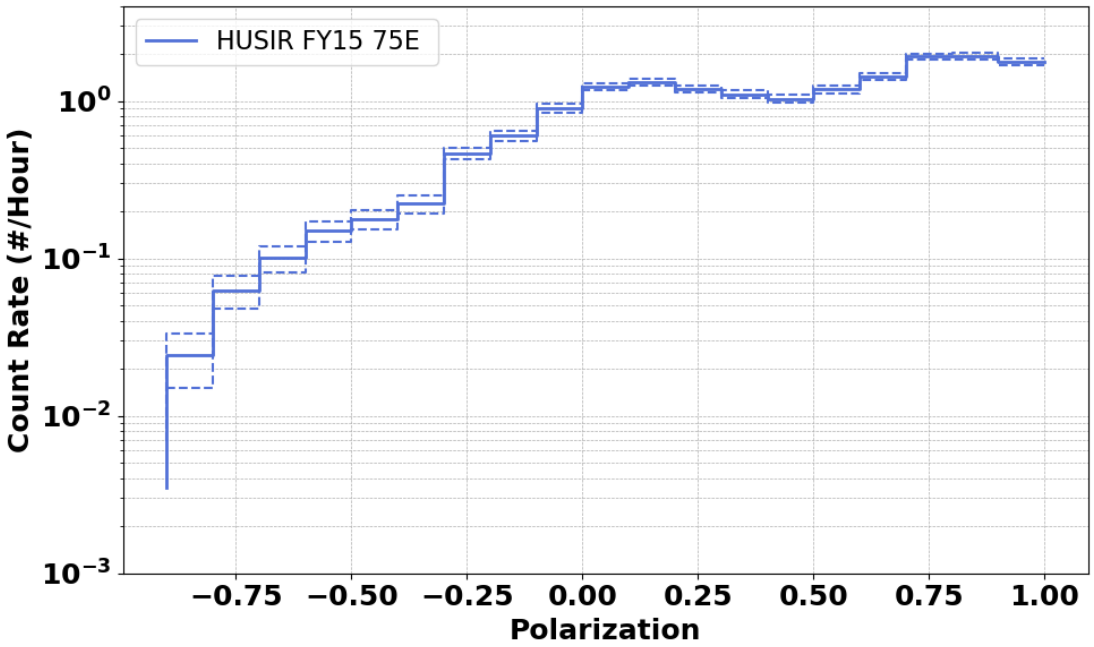

Figure C-26. Count Rate versus polarization ratio, HUSIR 75° east, FY2015.

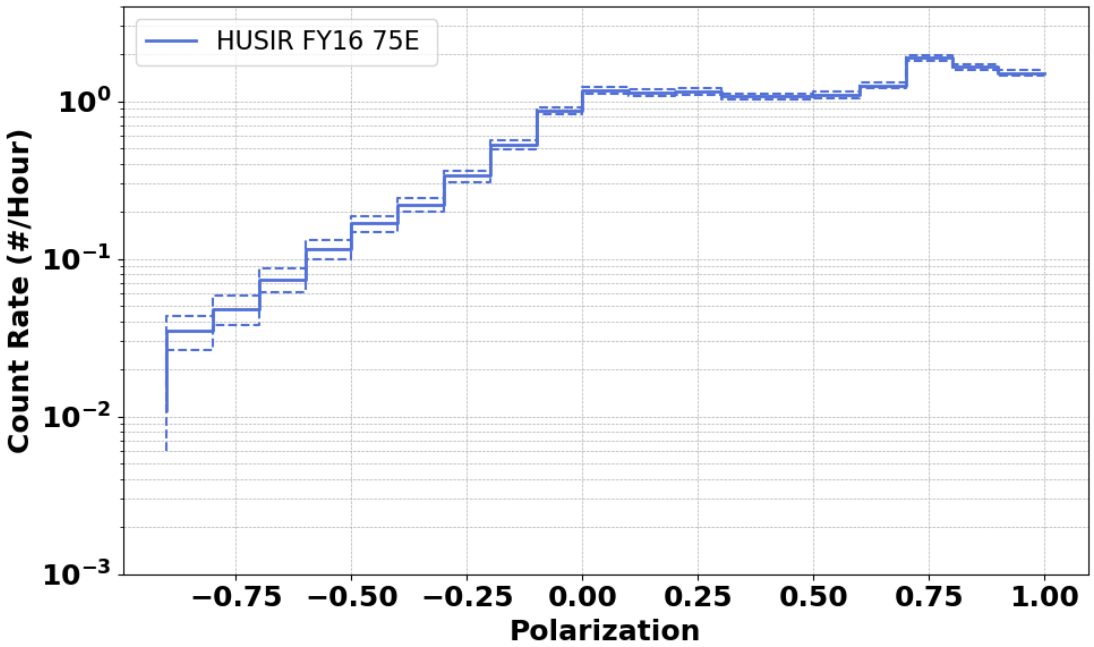

Figure C-27. Count Rate versus polarization ratio, HUSIR 75° east, FY2016.

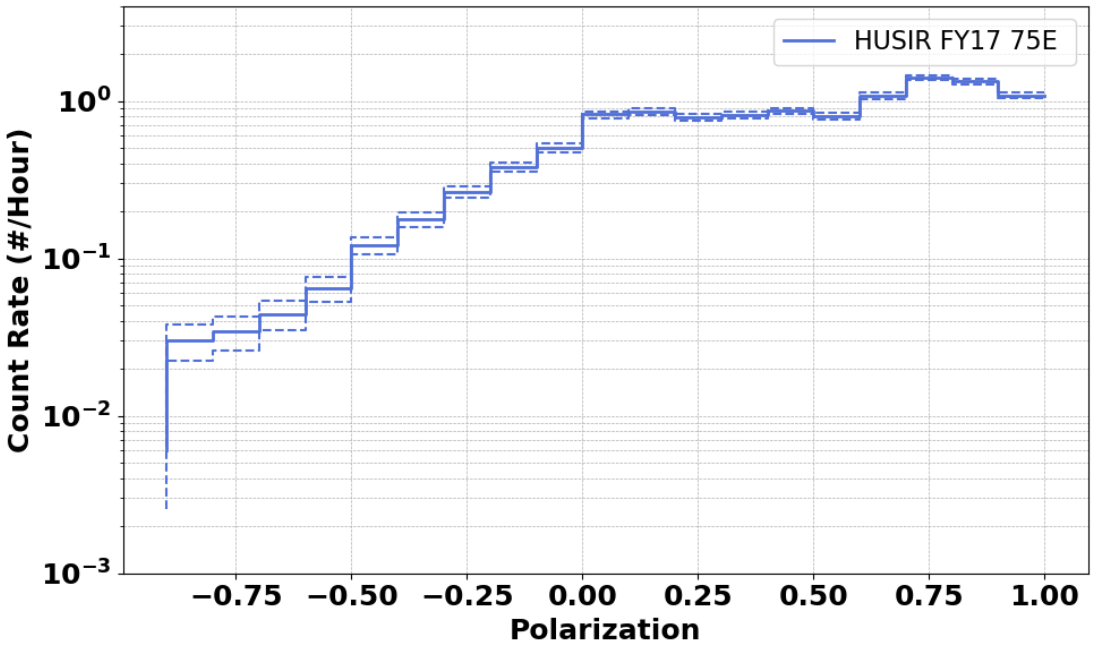

Figure C-28. Count Rate versus polarization ratio, HUSIR 75° east, FY2017.

C.8. TOTAL OBSERVED FLUX VERSUS ALTITUDE

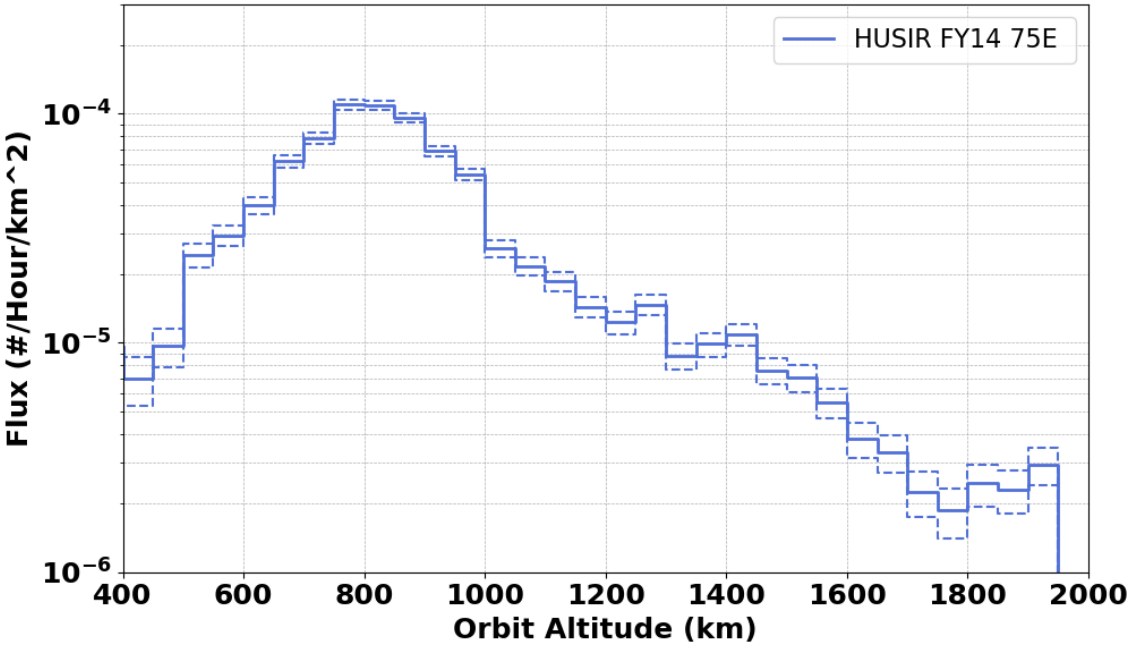

Figure C-29. Flux versus altitude, HUSIR 75° east, FY2014. No size or altitude limits applied.

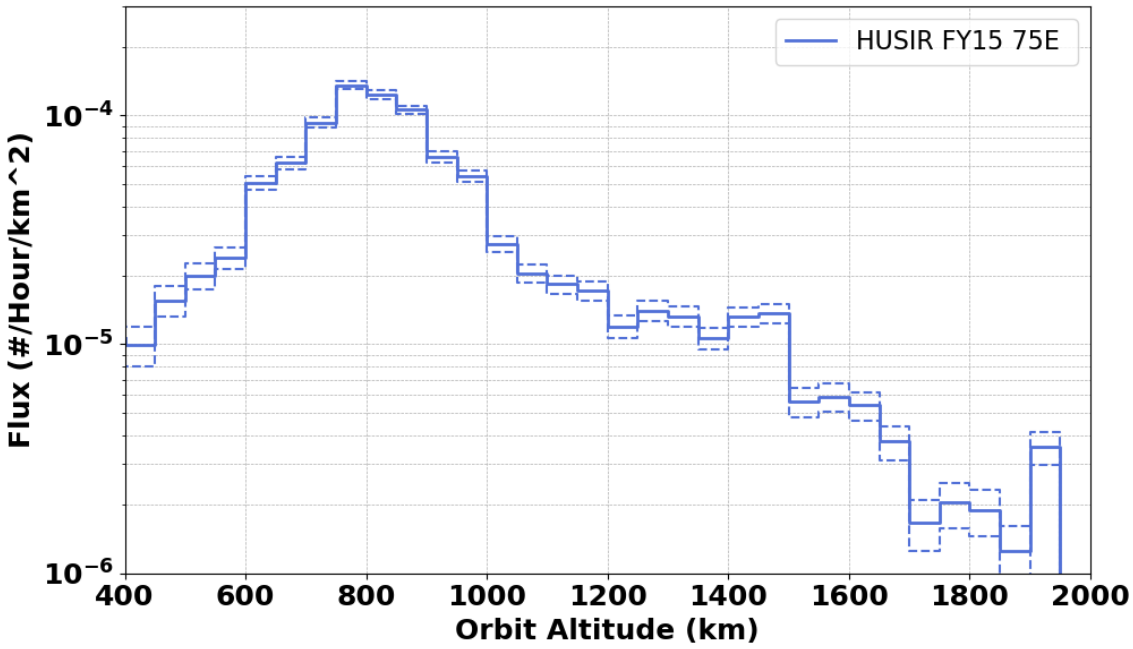

Figure C-30. Flux versus altitude, HUSIR 75° east, FY2015. No size or altitude limits applied.

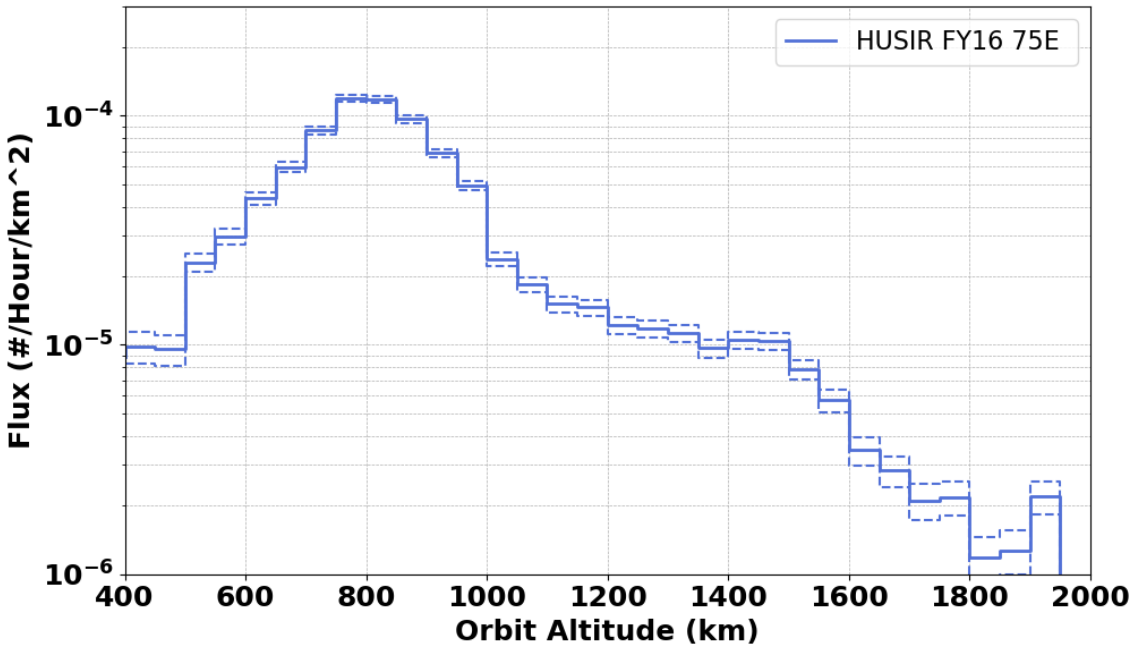

Figure C-31. Flux versus altitude, HUSIR 75° east, FY2016. No size or altitude limits applied.

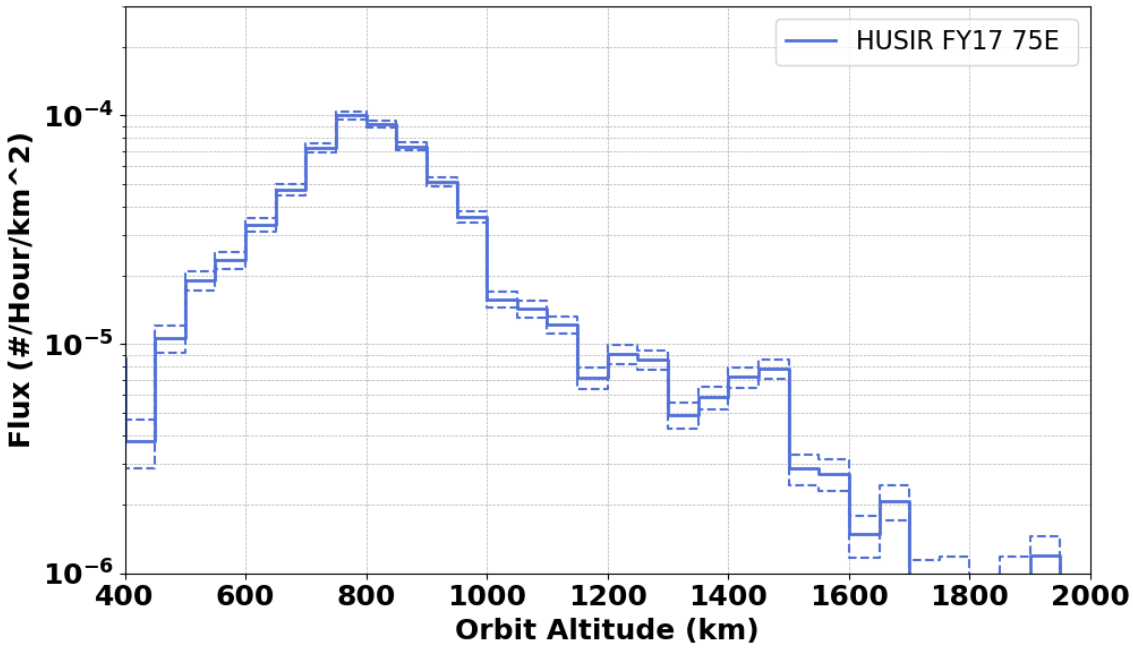

Figure C-32. Flux versus altitude, HUSIR 75° east, FY2017. No size or altitude limits applied.

C.9. TOTAL OBSERVED FLUX VERSUS INCLINATION

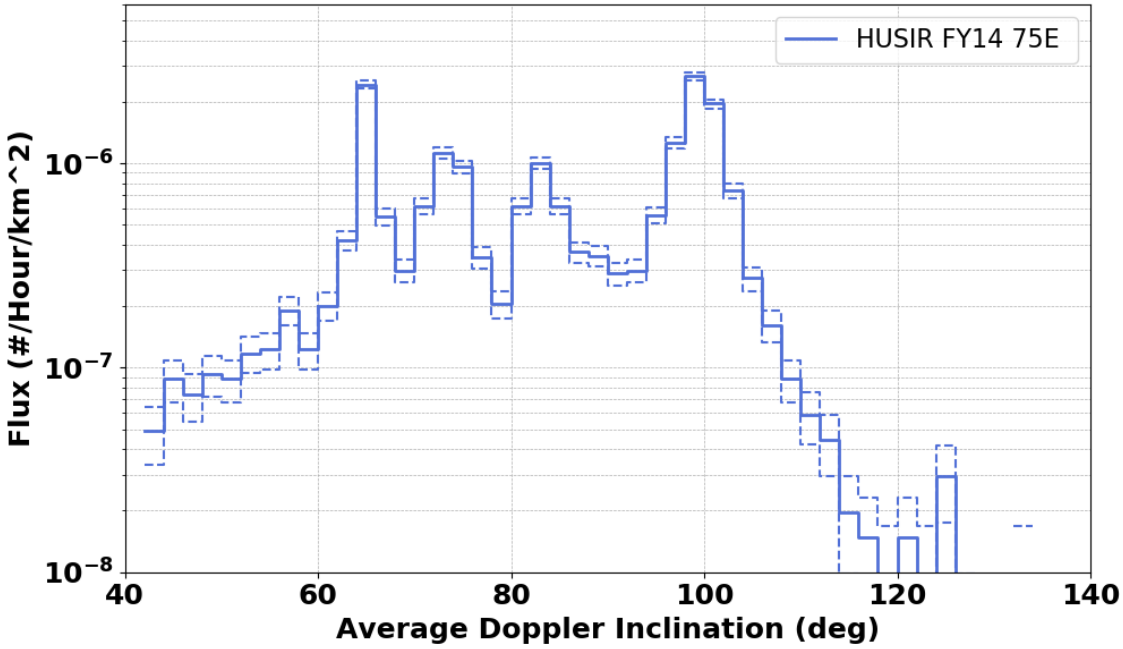

Figure C-33. Flux versus orbital inclination, HUSIR 75° east, FY2014. No size or altitude limits applied.

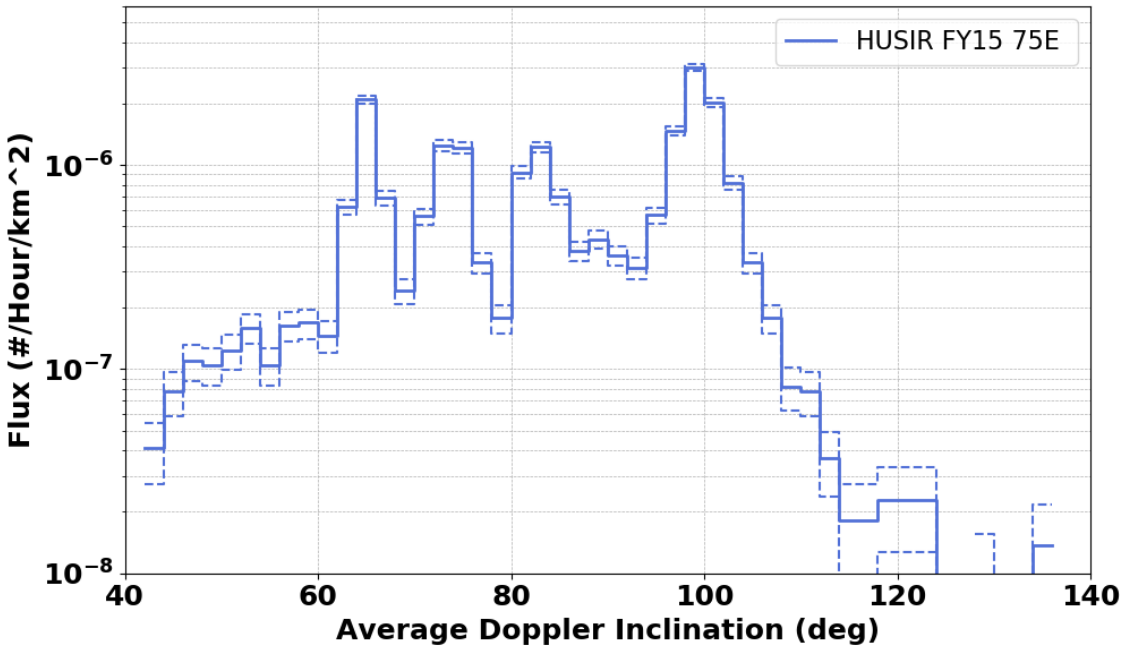

Figure C-34. Flux versus orbital inclination, HUSIR 75° east, FY2015. No size or altitude limits applied.

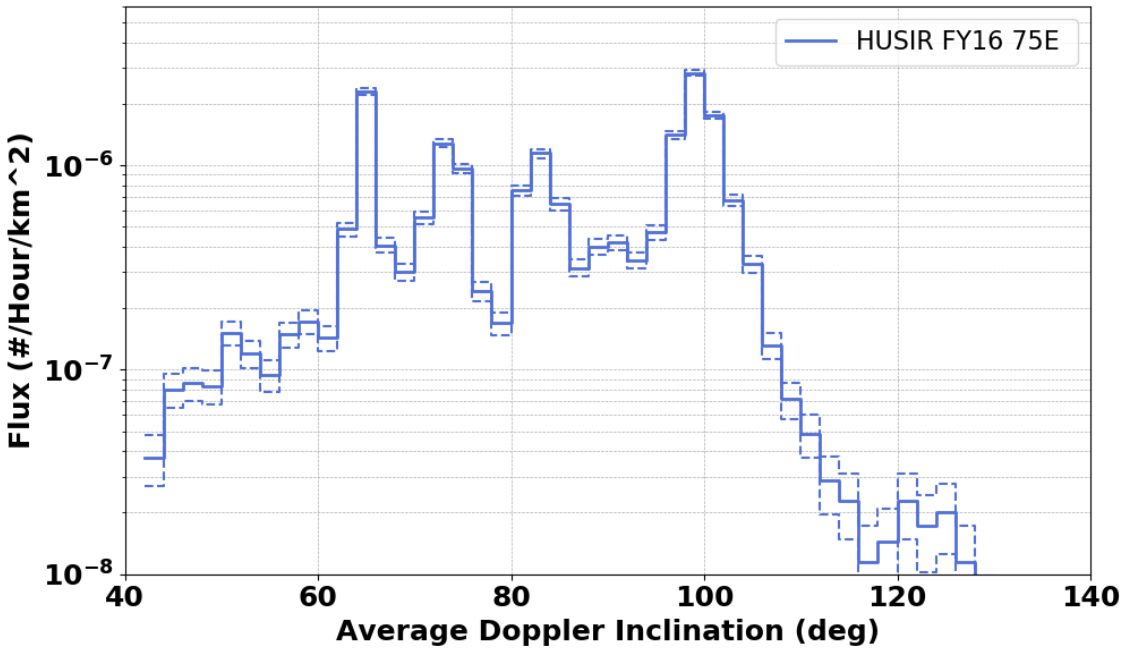

Figure C-35. Flux versus orbital inclination, HUSIR 75° east, FY2016. No size or altitude limits applied.

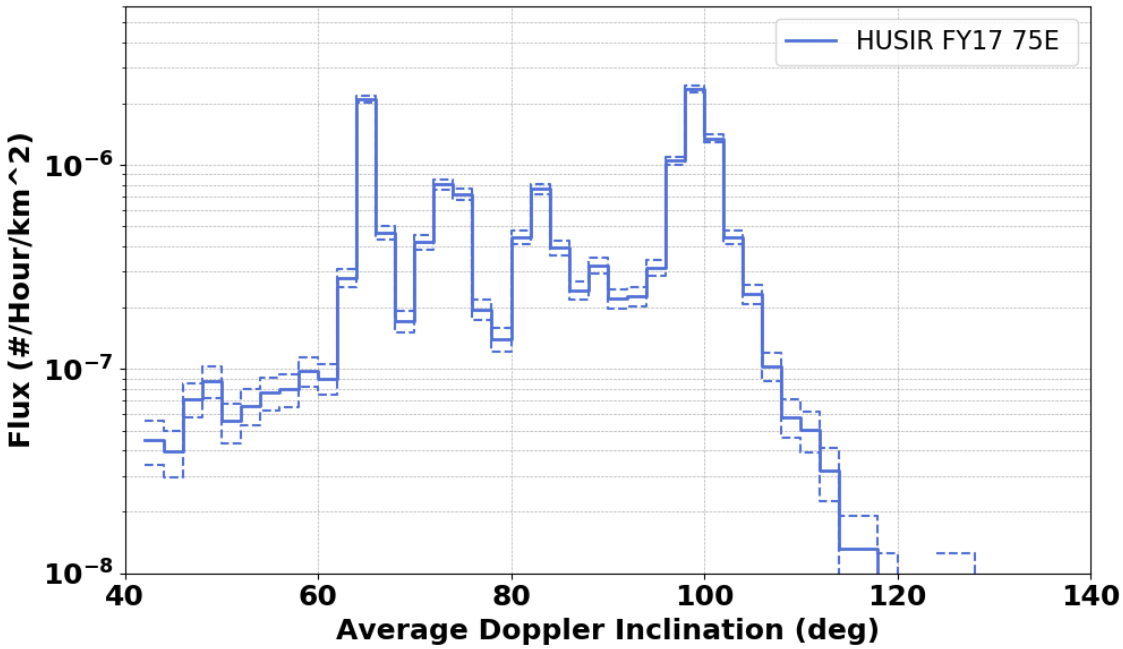

Figure C-36. Flux versus orbital inclination, HUSIR 75° east, FY2017. No size or altitude limits applied.

Appendix D: HUSIR 10° Elevation, South Pointing

D.1. RANGE VERSUS RANGE-RATE

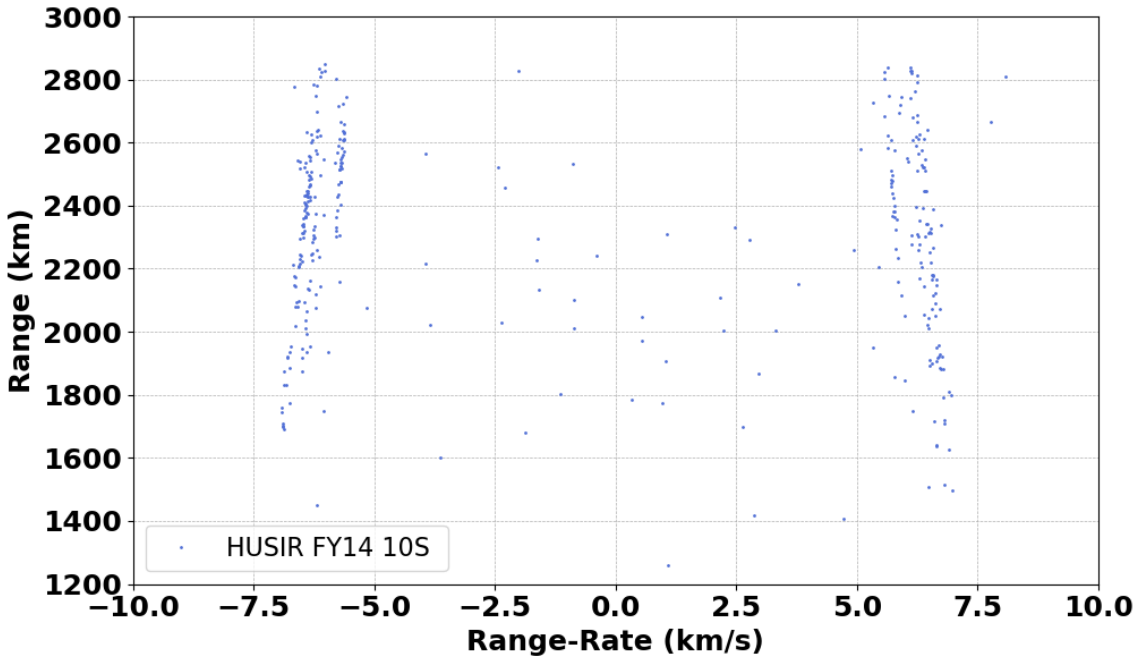

Figure D-1. Range versus Range-Rate, HUSIR 10° south, FY2014.

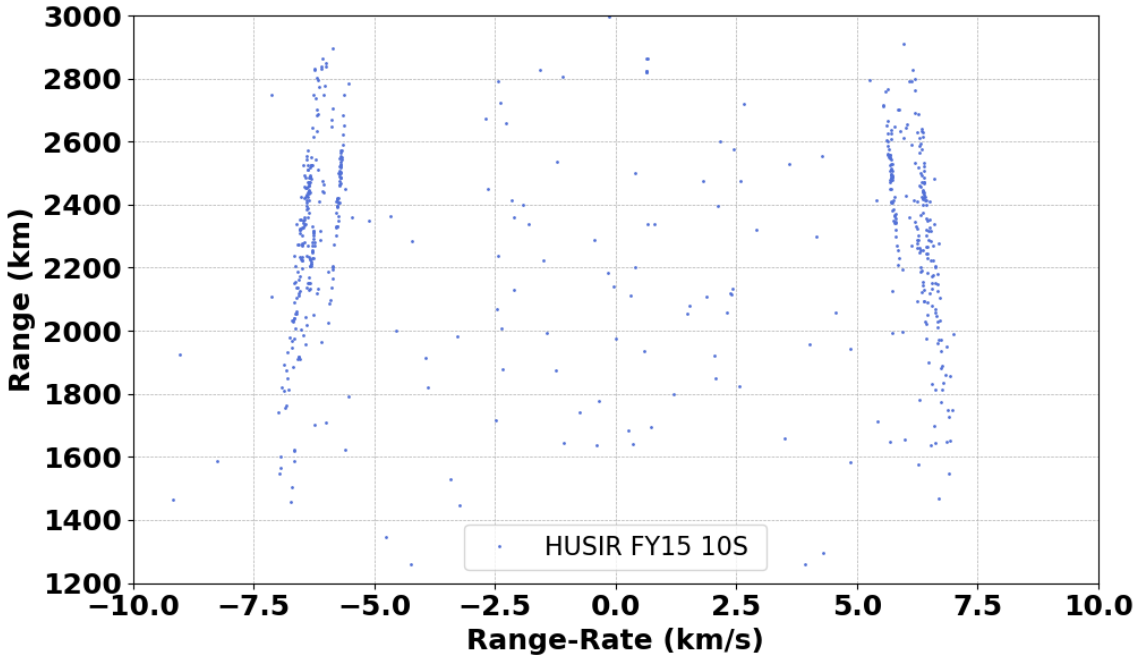

Figure D-2. Range versus Range-Rate, HUSIR 10° south, FY2015.

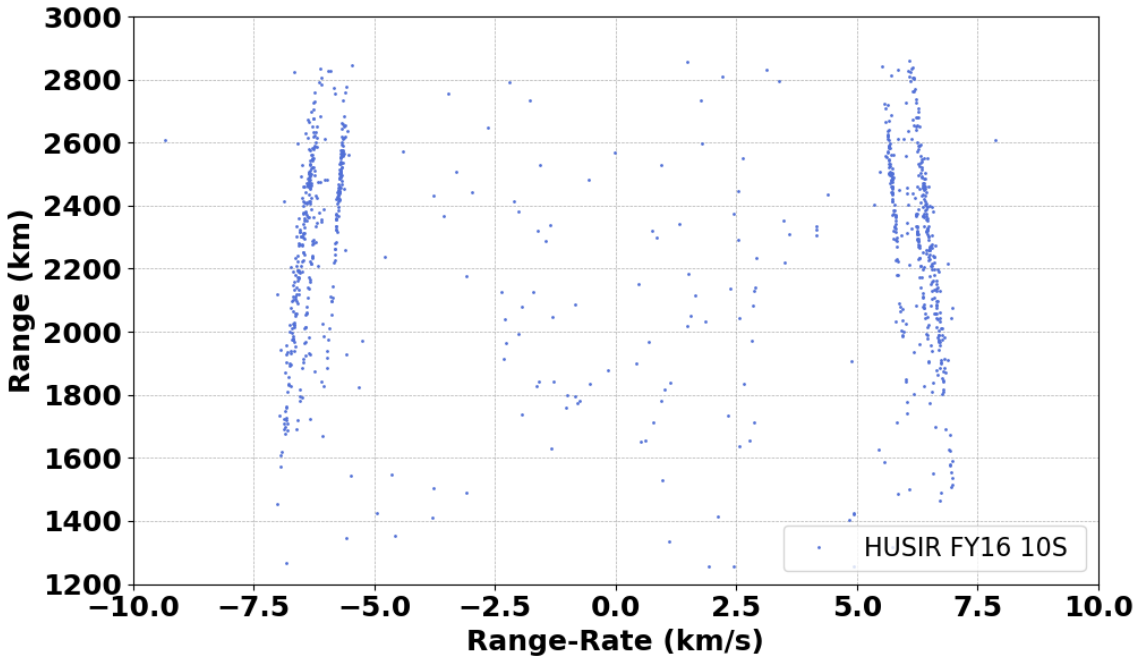

Figure D-3. Range versus Range-Rate, HUSIR 10° south, FY2016.

D.2. ALTITUDE VERSUS INCLINATION

For 75° east-staring data, the difference between the two Doppler inclination estimates is on the order of a degree. Due to the interaction geometry of the HUSIR beam with low Earth orbits in south-staring configurations, the two Doppler inclination estimates are supplemental and as such, always average to 90°. Consequently, the Doppler inclination presented for south-staring data – both 10S and 20S – is the smaller of the two Doppler inclination estimates. Additional analysis is required before drawing conclusions, particularly for inclinations above 80°, where many detections may be associated with the greater than 90° sun-synchronous orbits.

Each plot contains a dashed curve that represents an estimate of the minimum orbital inclination that can be measured as a function of altitude. This estimate is calculated as the sub-satellite latitude of the intersection of the boresight of the radar beam with a line from the center of the earth to the intersection point.

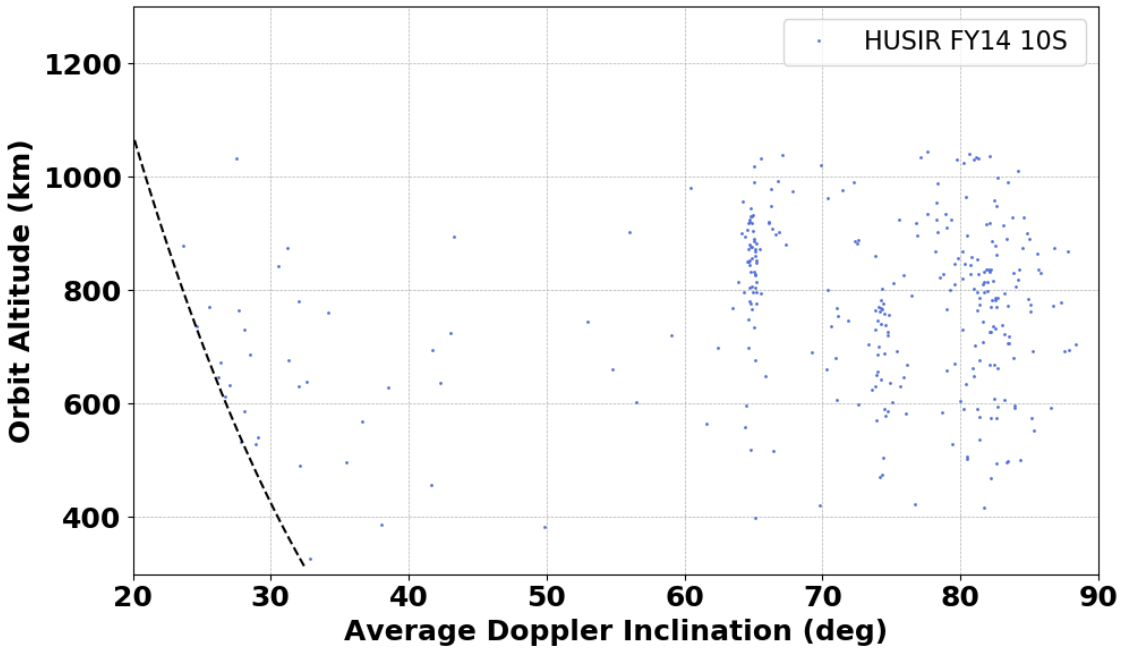

Figure D-4. Altitude versus orbital inclination, HUSIR 10° south, FY2014. Inclination derived from Range-Rate assuming a circular orbit.

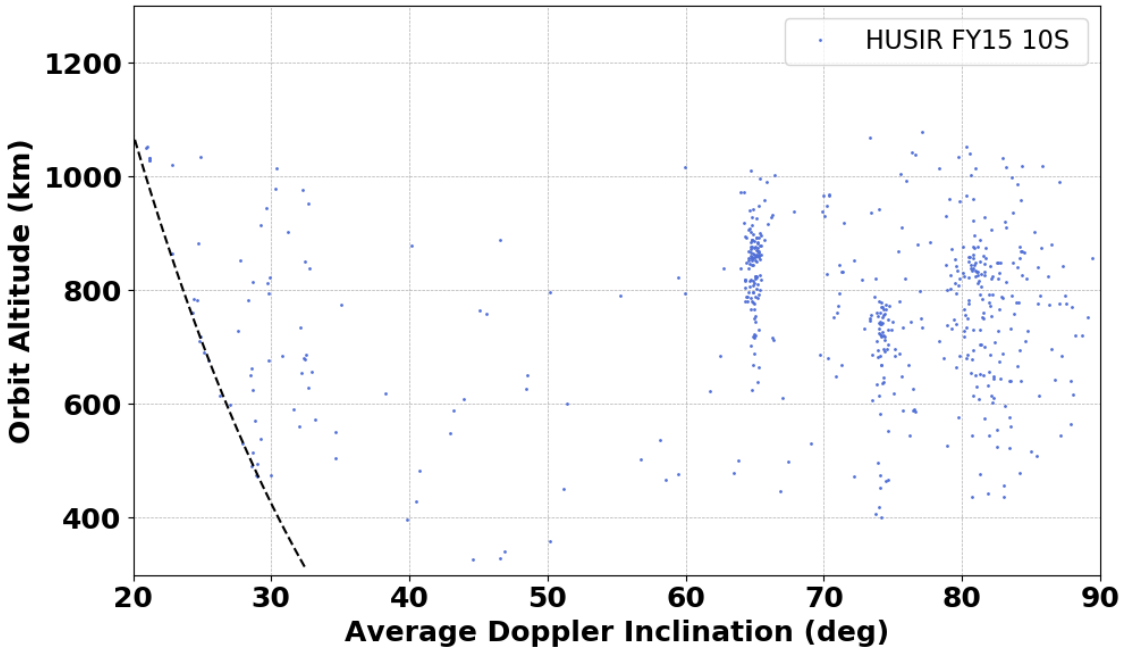

Figure D-5. Altitude versus orbital inclination, HUSIR 10° south, FY2015. Inclination derived from Range-Rate assuming a circular orbit.

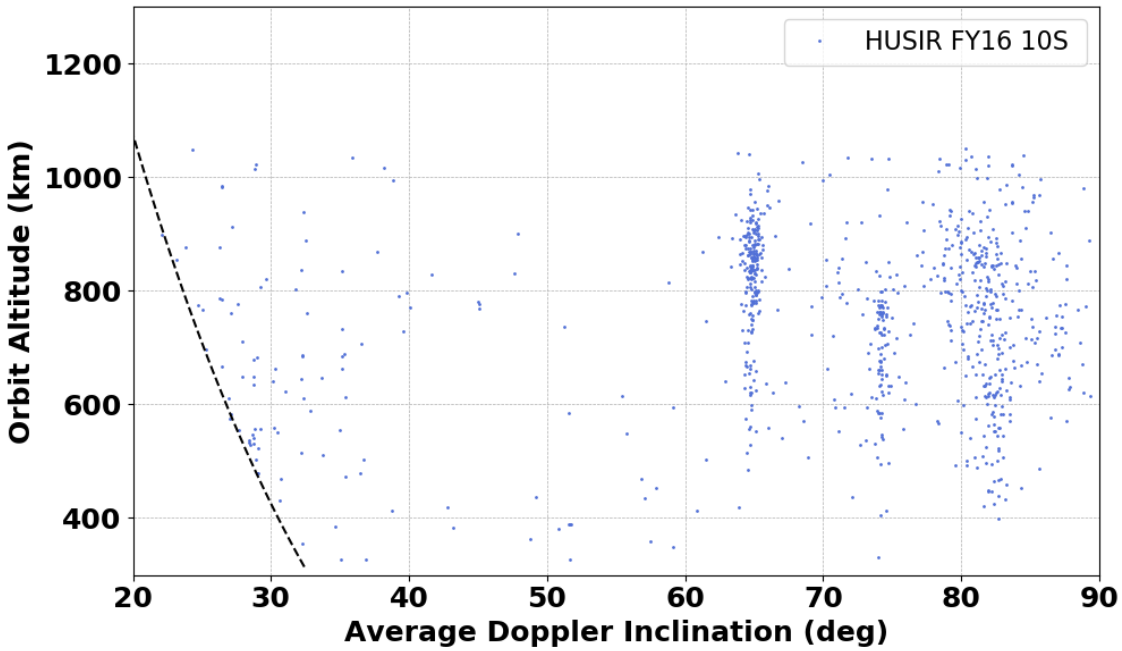

Figure D-6. Altitude versus orbital inclination, HUSIR 10° south, FY2016. Inclination derived from Range-Rate assuming a circular orbit.

D.3. RANGE VERSUS RADAR CROSS SECTION

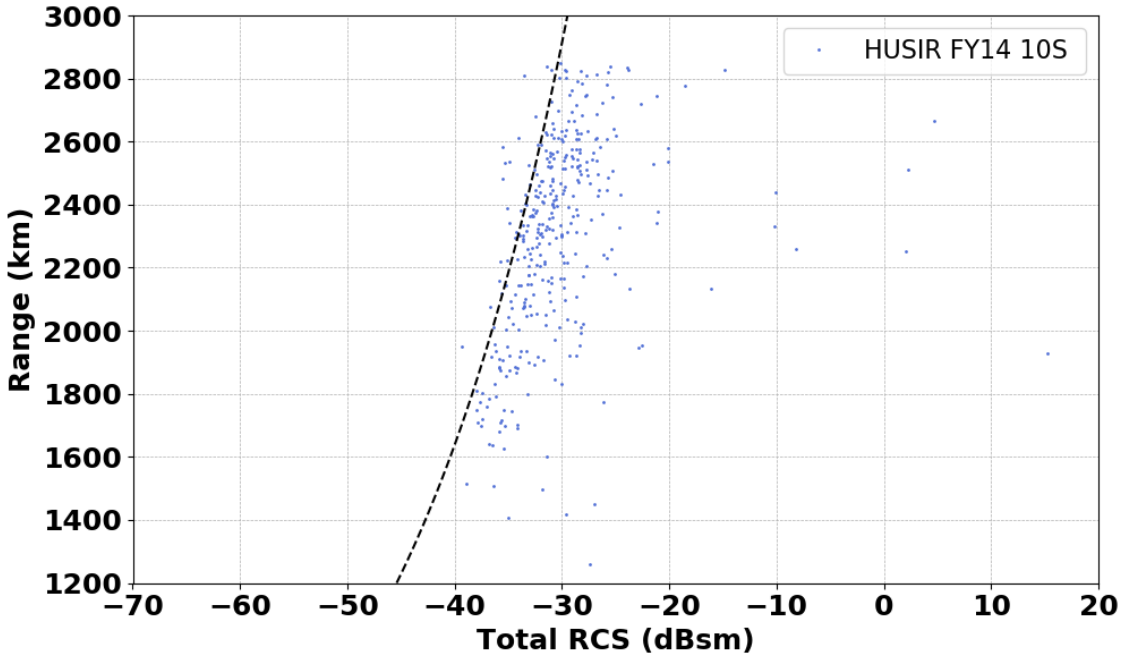

Figure D-7. Range versus Radar Cross Section, HUSIR 10° south, FY2014.

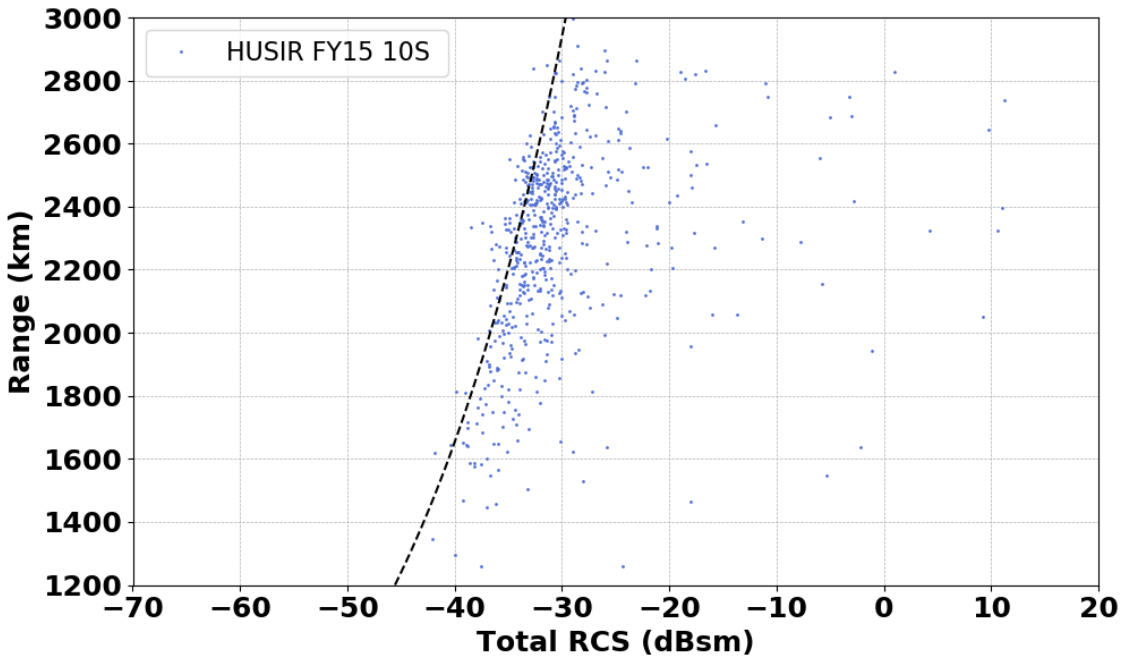

Figure D-8. Range versus Radar Cross Section, HUSIR 10° south, FY2015.

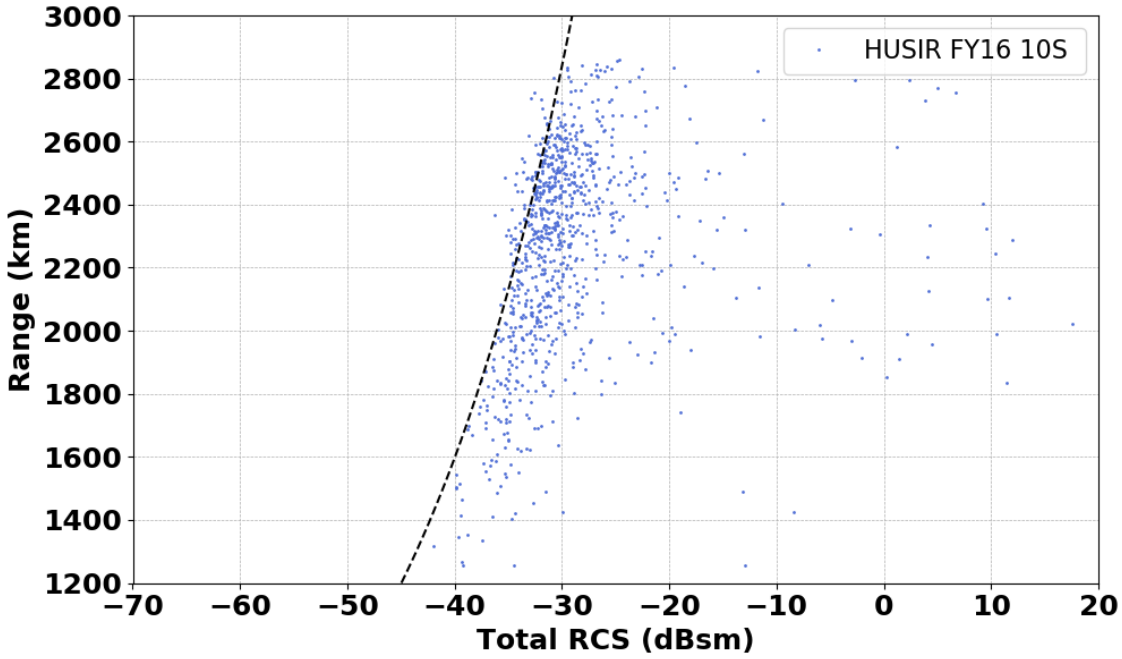

Figure D-9. Range versus Radar Cross Section, HUSIR 10° south, FY2016.

D.4. CUMULATIVE DETECTION RATE VERSUS SEM SIZE

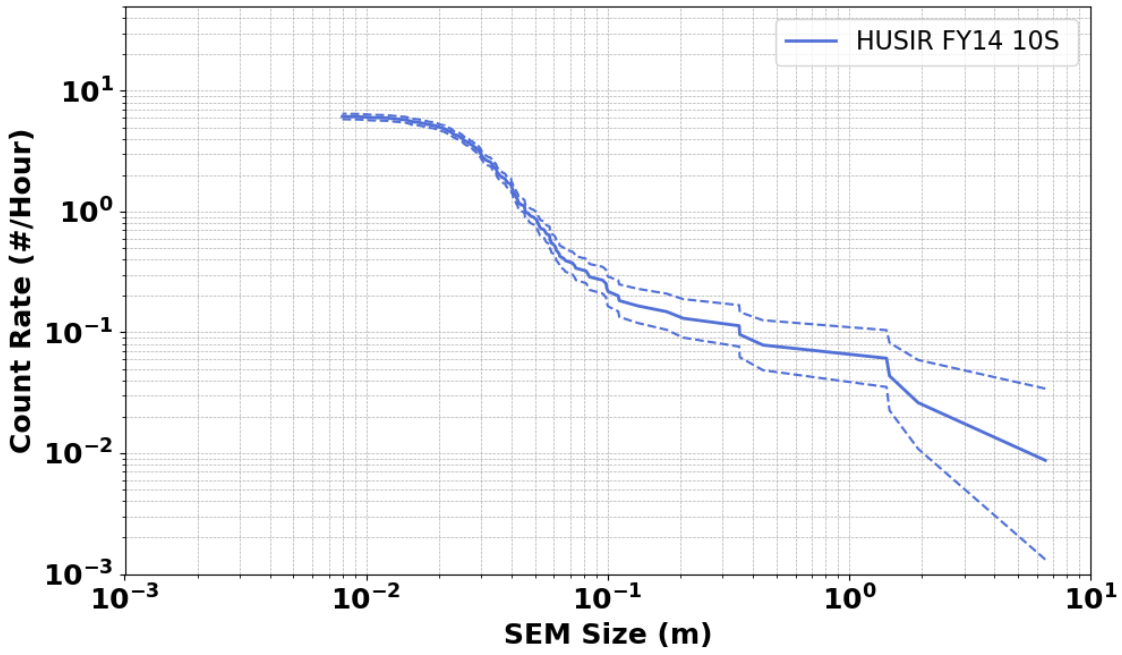

Figure D-10. Cumulative count rate versus SEM size, HUSIR 10° south, FY2014.

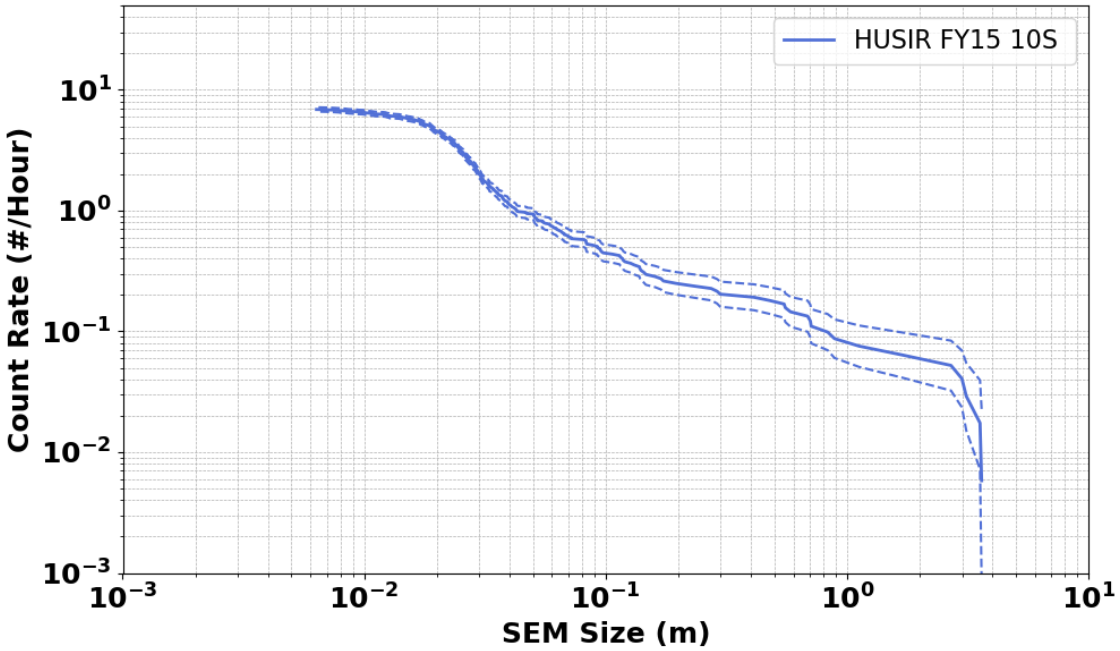

Figure D-11. Cumulative count rate versus SEM size, HUSIR 10° south, FY2015.

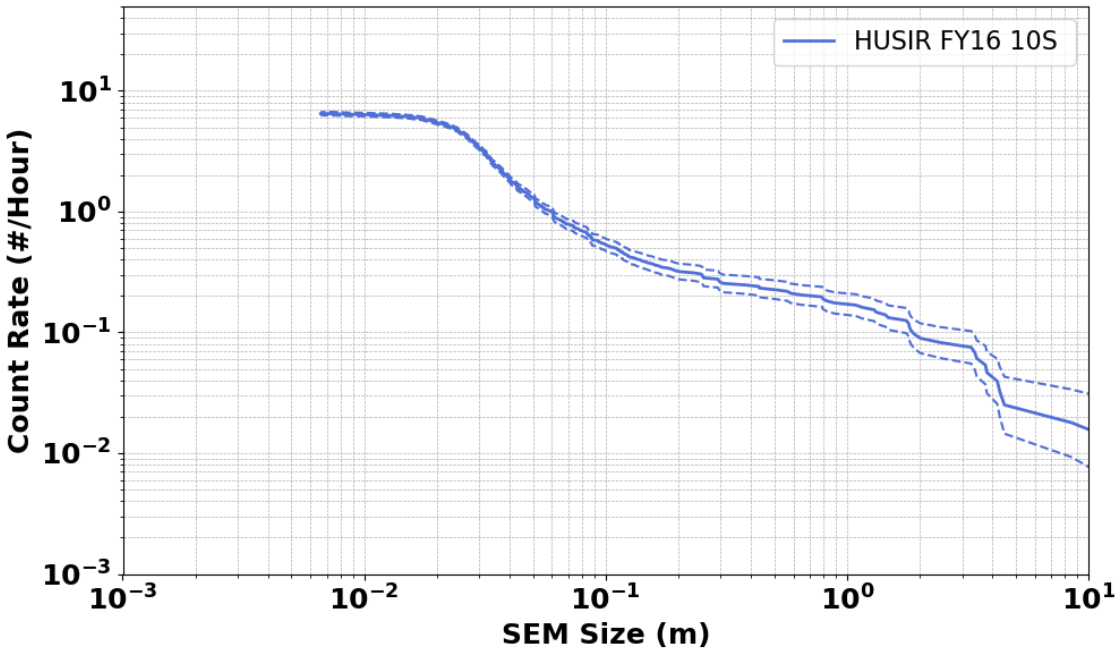

Figure D-12. Cumulative count rate versus SEM size, HUSIR 10° south, FY2016.

D.5. CUMULATIVE DETECTION RATE VERSUS PP SNR

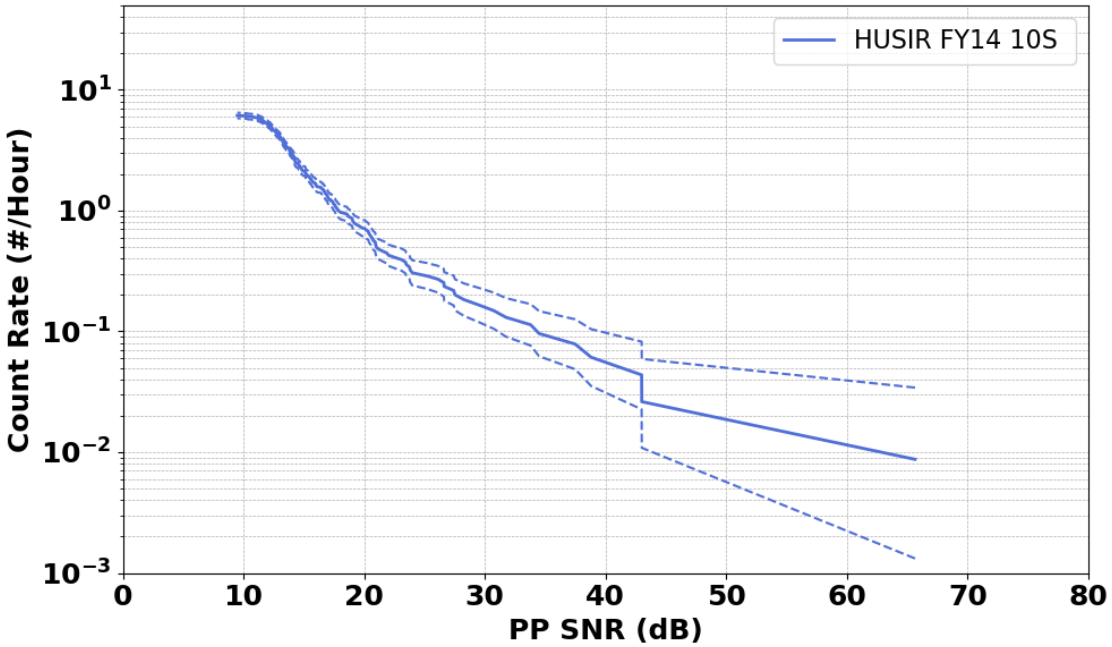

Figure D-13. Cumulative count rate versus detection SNR of the principle polarization, HUSIR 10° south, FY2014.

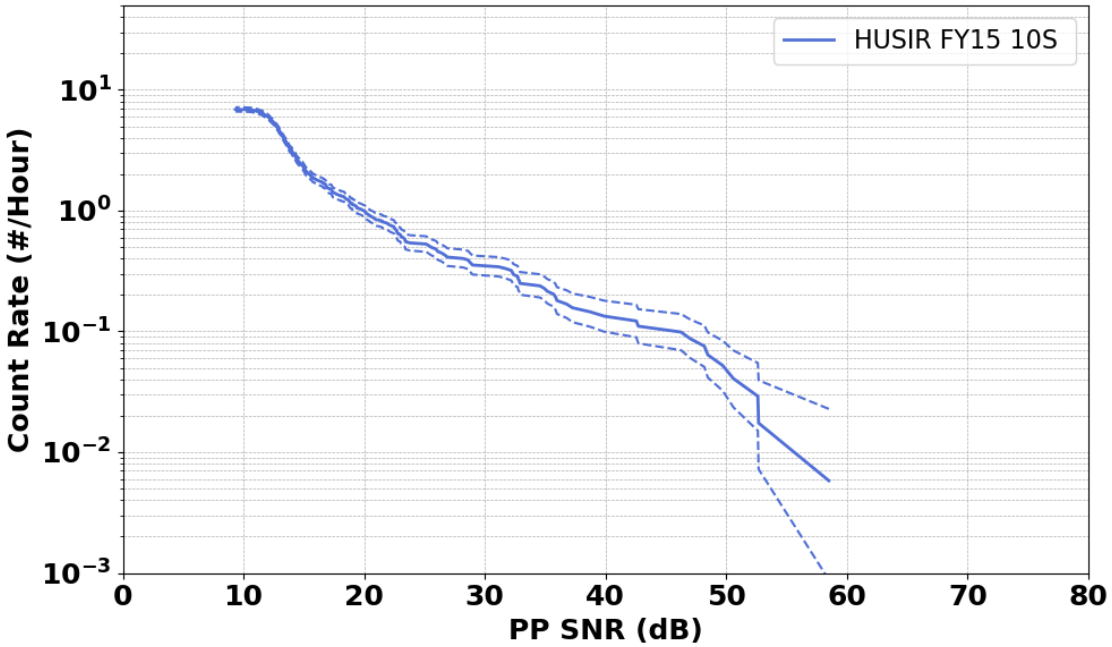

Figure D-14. Cumulative count rate versus detection SNR of the principle polarization, HUSIR 10° south, FY2015.

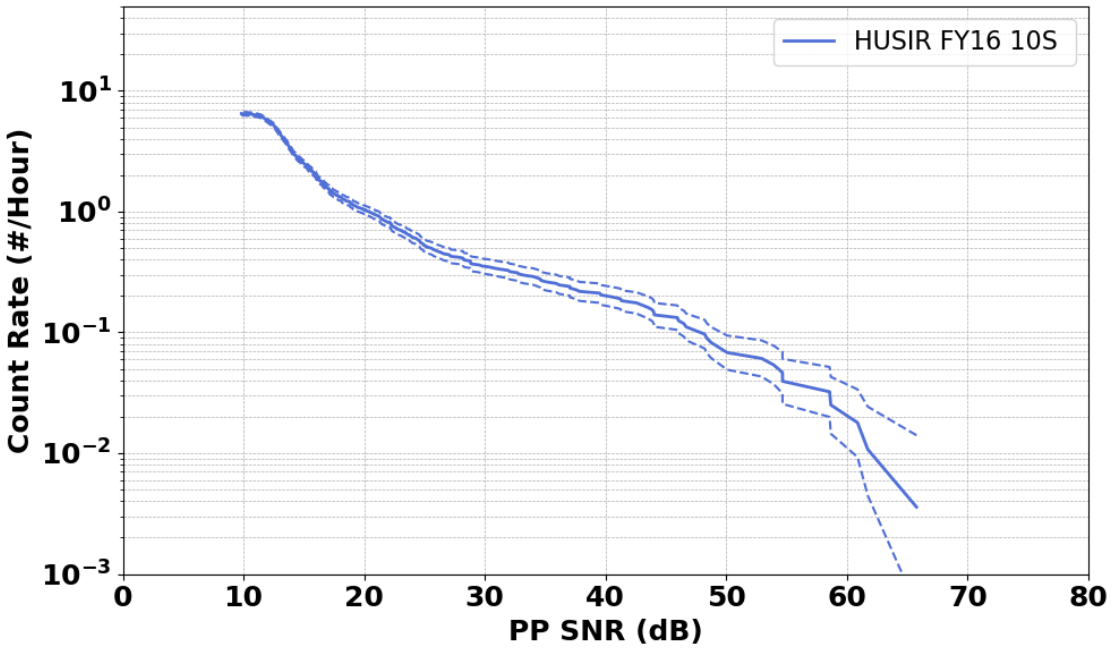

Figure D-15. Cumulative count rate versus detection SNR of the principle polarization, HUSIR 10° south, FY2016.

D.6. CUMULATIVE DETECTION RATE VERSUS RADAR CROSS SECTION

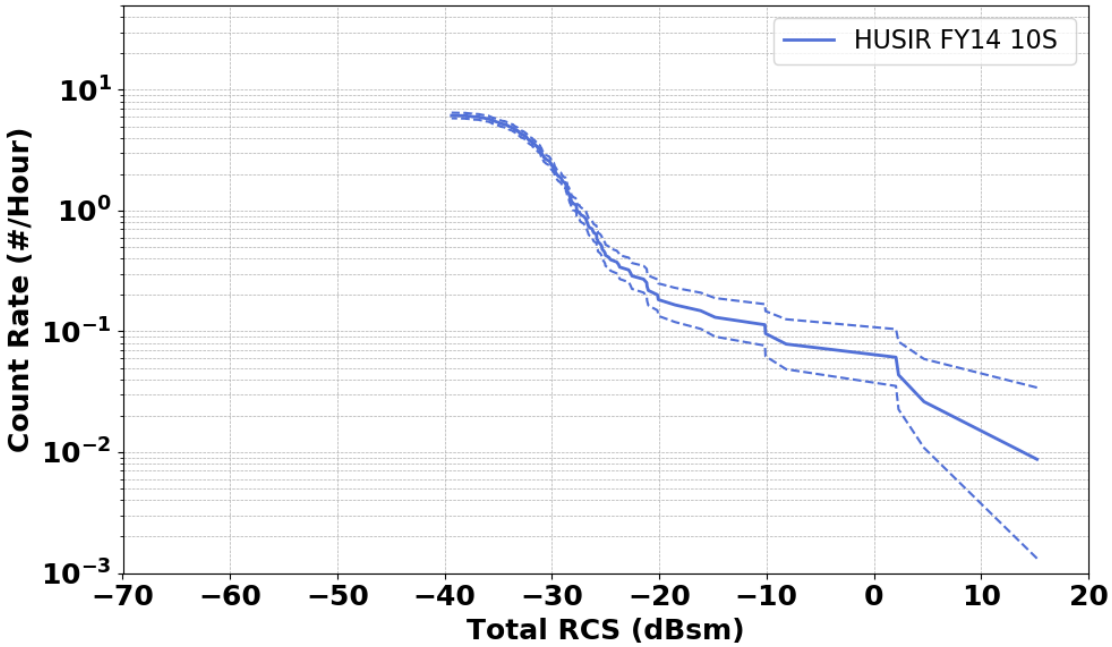

Figure D-16. Cumulative count rate versus Total Radar Cross Section, HUSIR 10° south, FY2014.

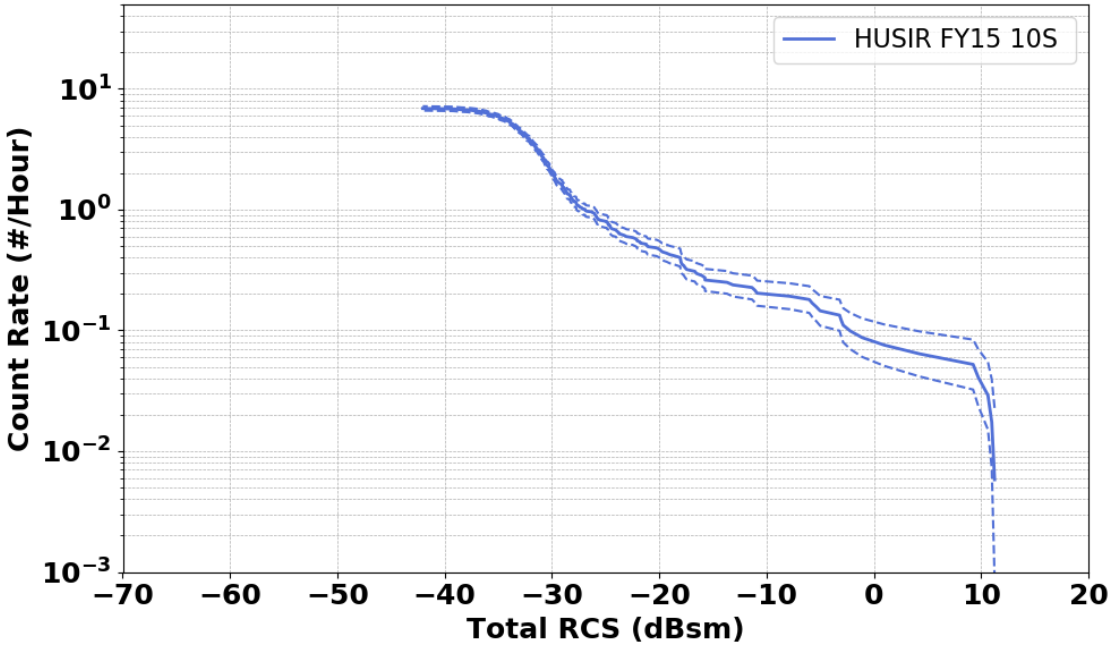

Figure D-17. Cumulative count rate versus Total Radar Cross Section, HUSIR 10° south, FY2015.

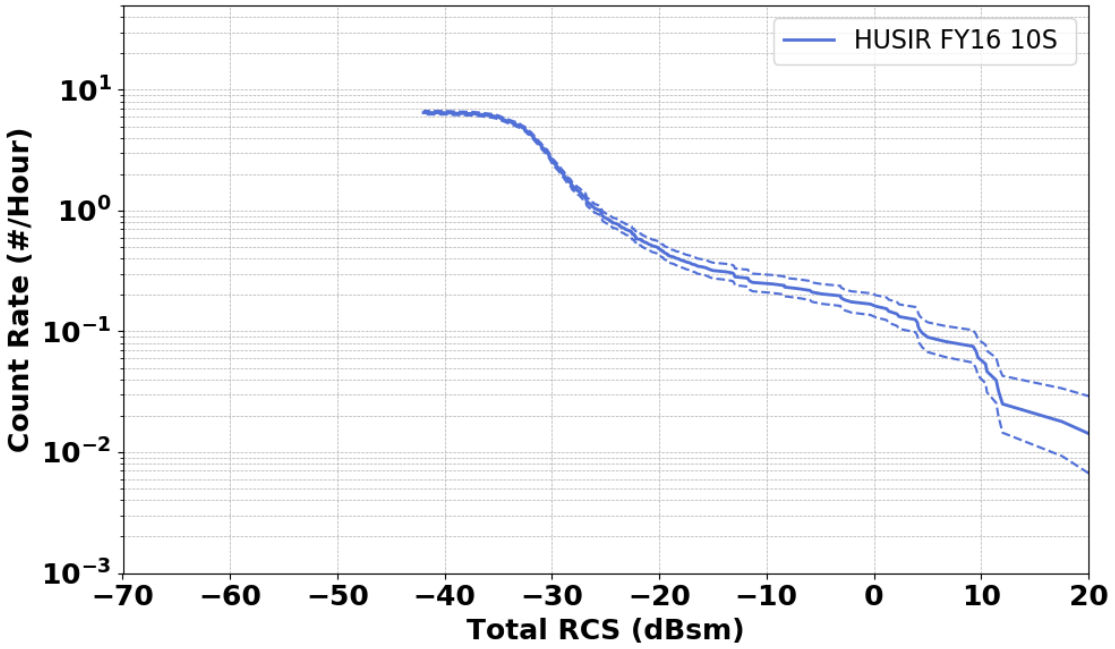

Figure D-18. Cumulative count rate versus Total Radar Cross Section, HUSIR 10° south, FY2016.

D.7. POLARIZATION RATIO DISTRIBUTION

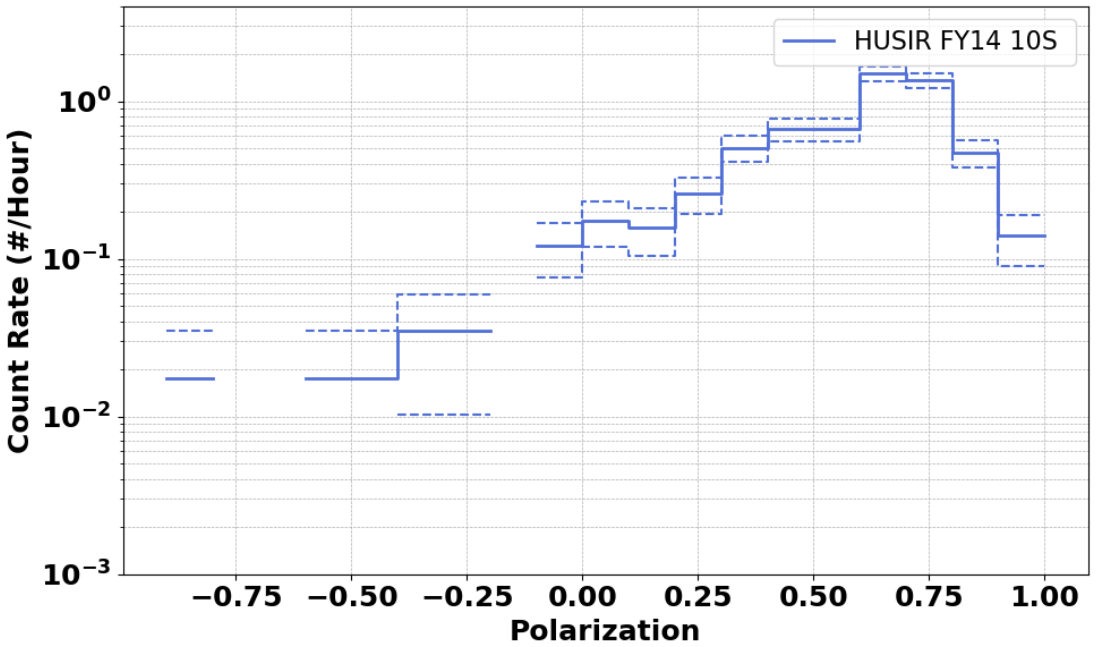

Figure D-19. Count Rate versus polarization ratio, HUSIR 10° south, FY2014.

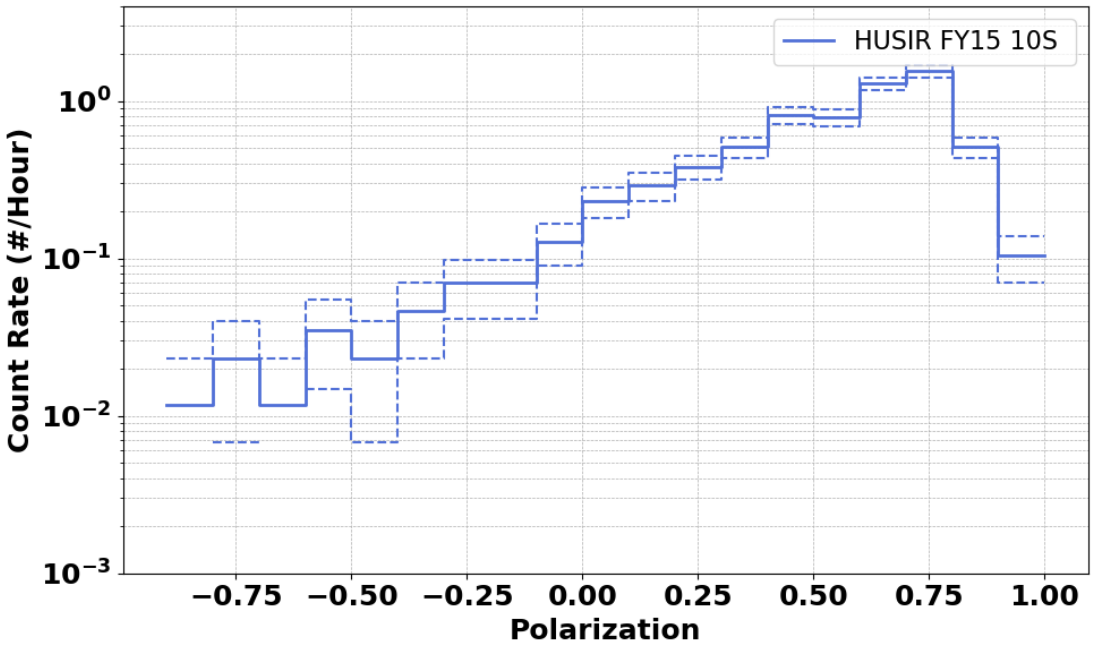

Figure D-20. Count Rate versus polarization ratio, HUSIR 10° south, FY2015.

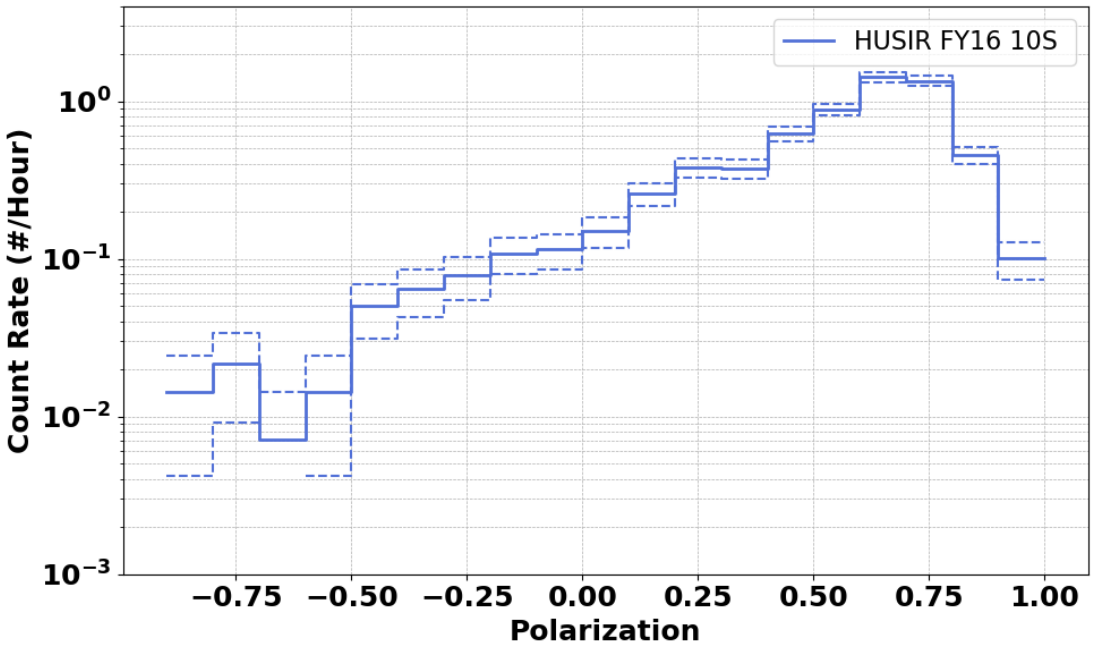

Figure D-21. Count Rate versus polarization ratio, HUSIR 10° south, FY2016.

Appendix E: HUSIR 20° Elevation, South Pointing

E.1. RANGE VERSUS RANGE-RATE

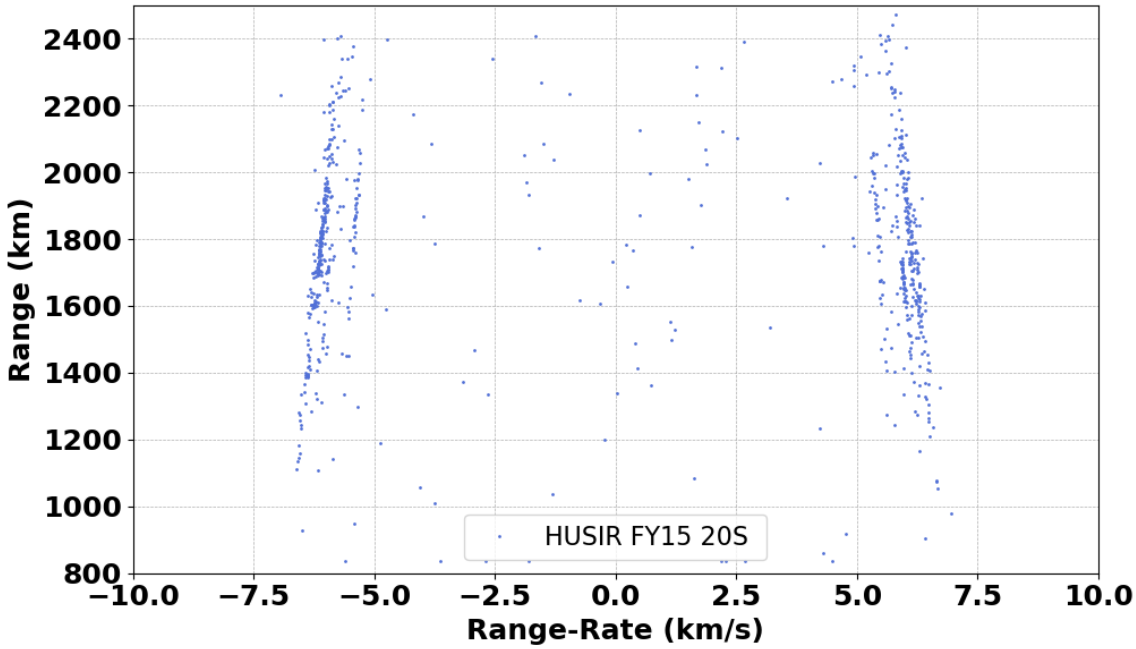

Figure E-1. Range versus Range-Rate, HUSIR 20° south, FY2015.

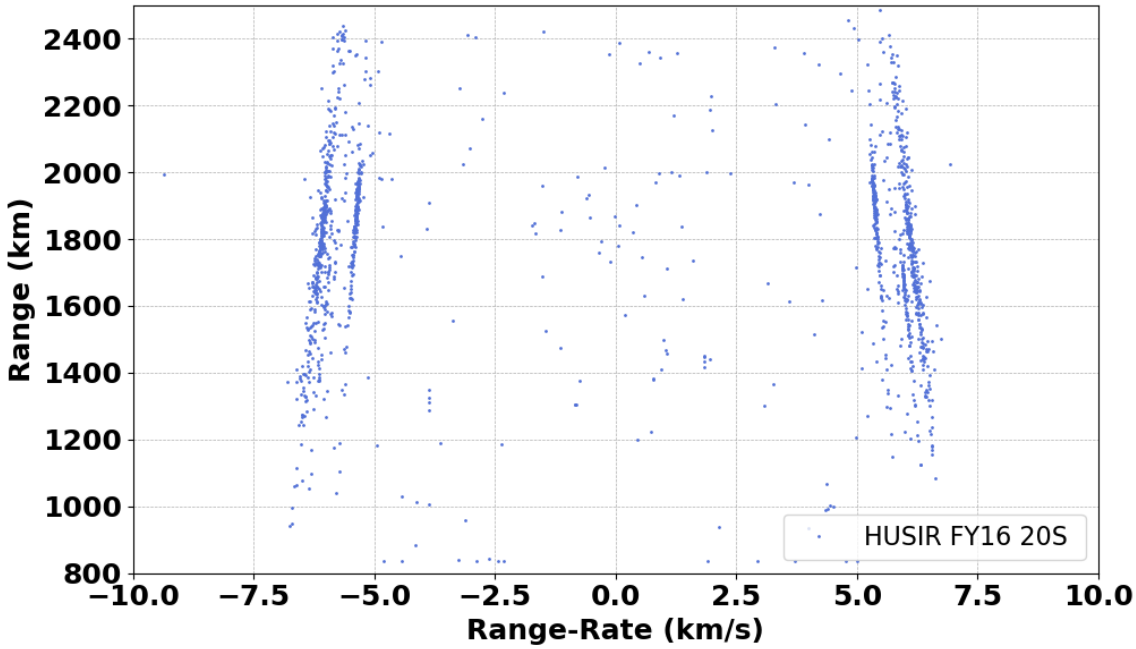

Figure E-2. Range versus Range-Rate, HUSIR 20° south, FY2016.

E.2. ALTITUDE VERSUS INCLINATION

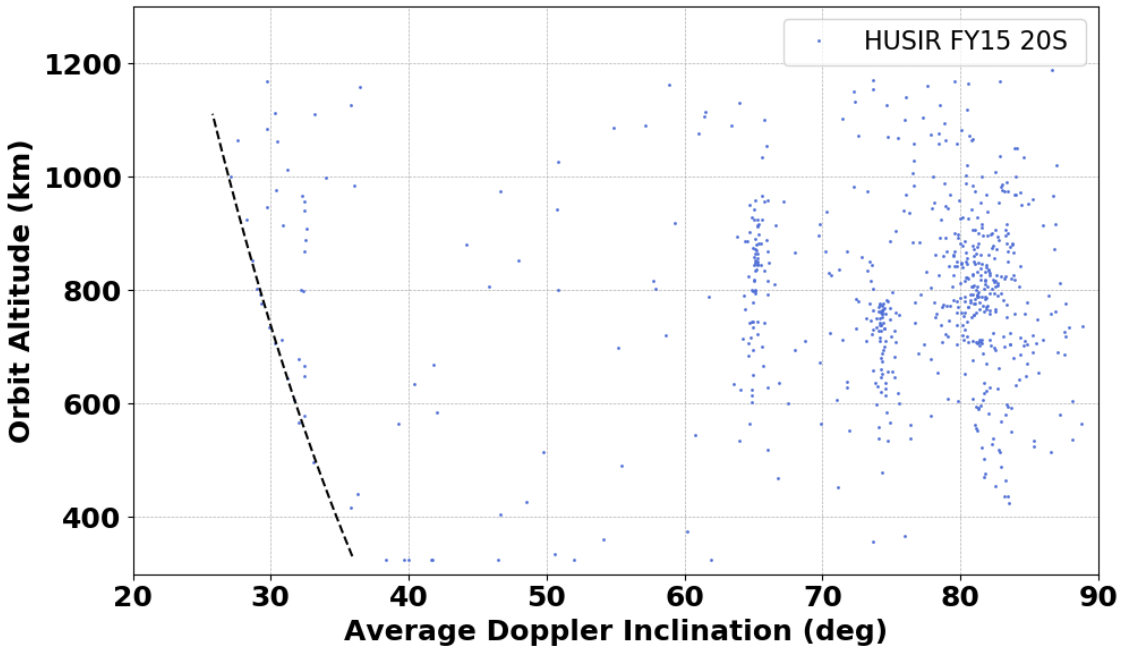

Figure E-3. Altitude versus orbital inclination, HUSIR 20° south, FY2015. Inclination derived from Range-Rate assuming a circular orbit.

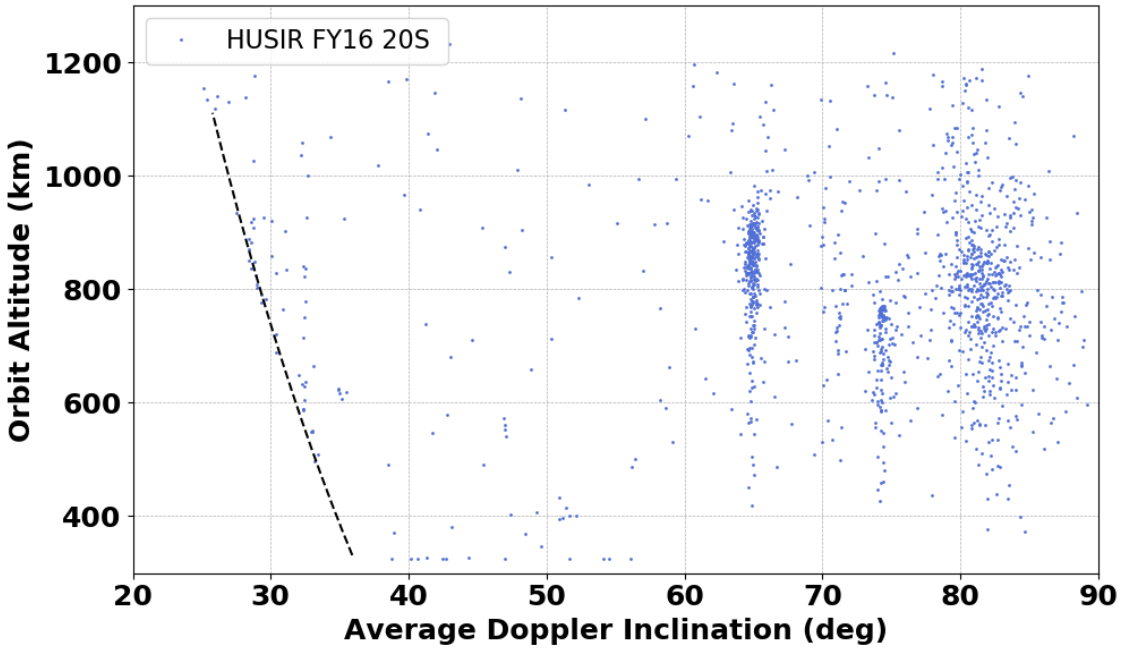

Figure E-4. Altitude versus orbital inclination, HUSIR 20° south, FY2016. Inclination derived from Range-Rate assuming a circular orbit.

E.3. RANGE VERSUS RADAR CROSS SECTION

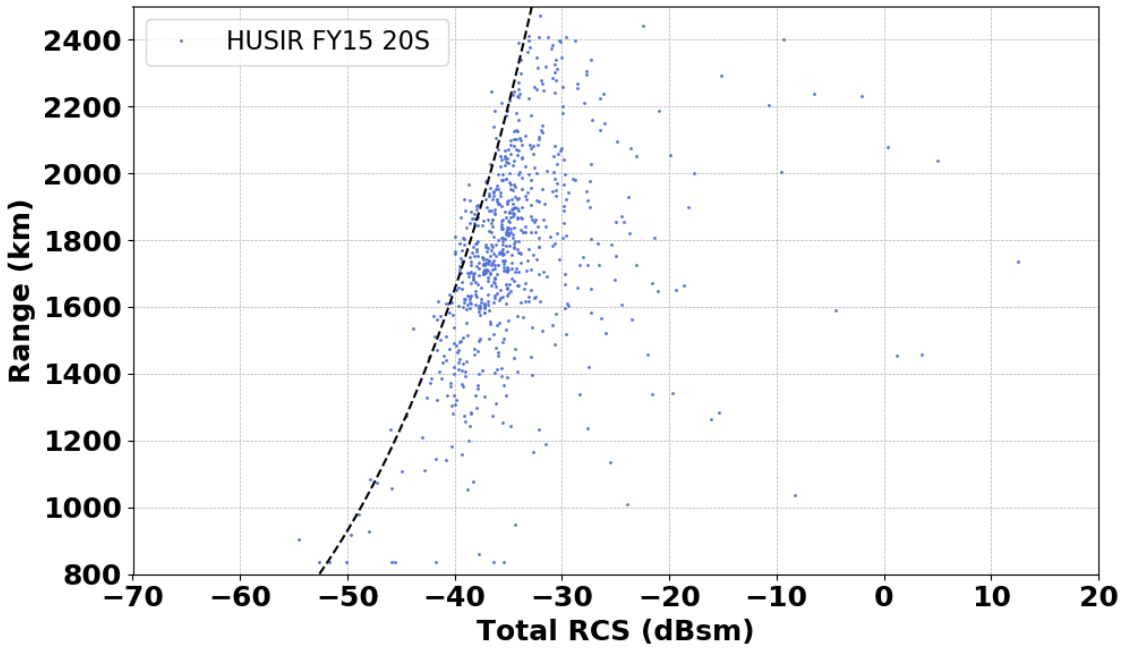

Figure E-5. Range versus Radar Cross Section, HUSIR 20° south, FY2015.

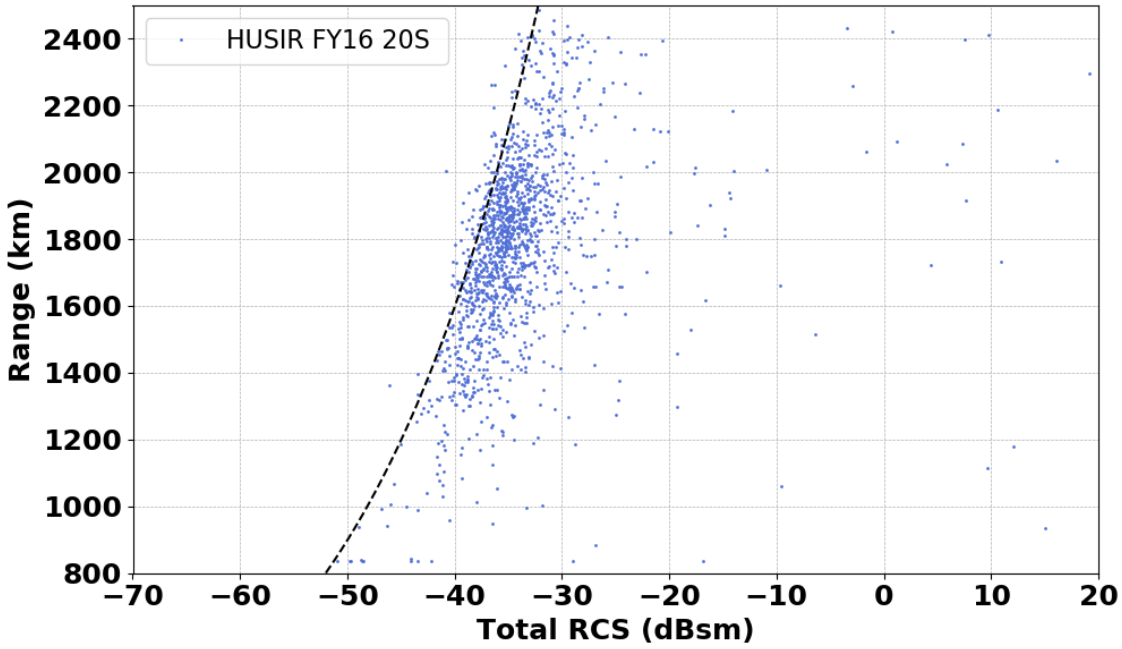

Figure E-6. Range versus Radar Cross Section, HUSIR 20° south, FY2016.

E.4. CUMULATIVE DETECTION RATE VERSUS SEM SIZE

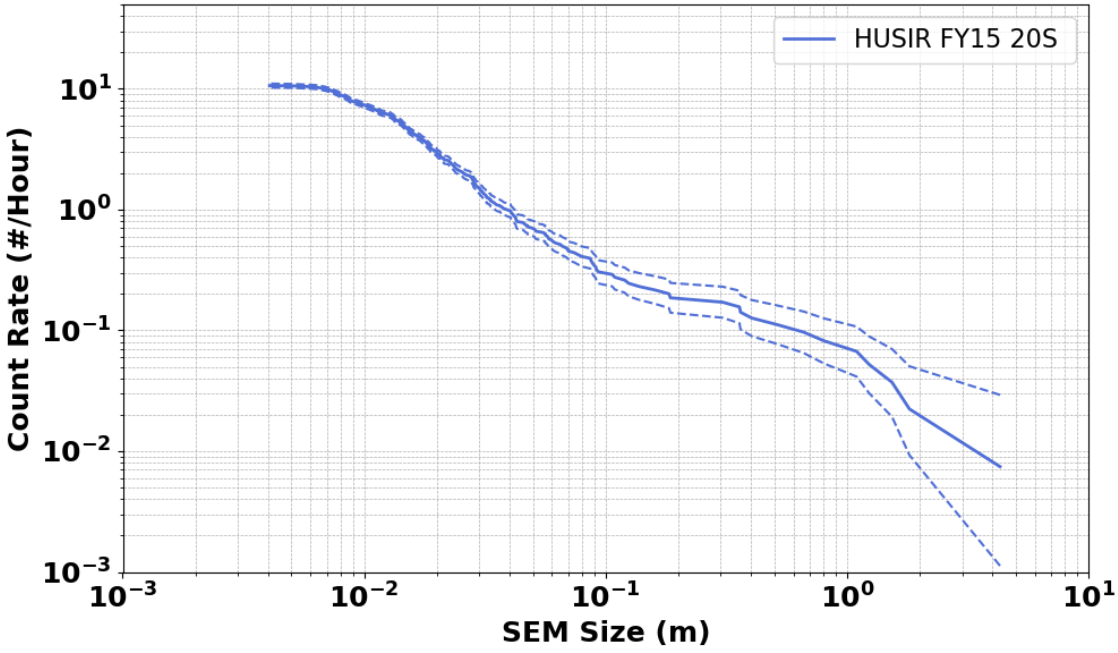

Figure E-7. Cumulative count rate versus SEM size, HUSIR 20° south, FY2015.

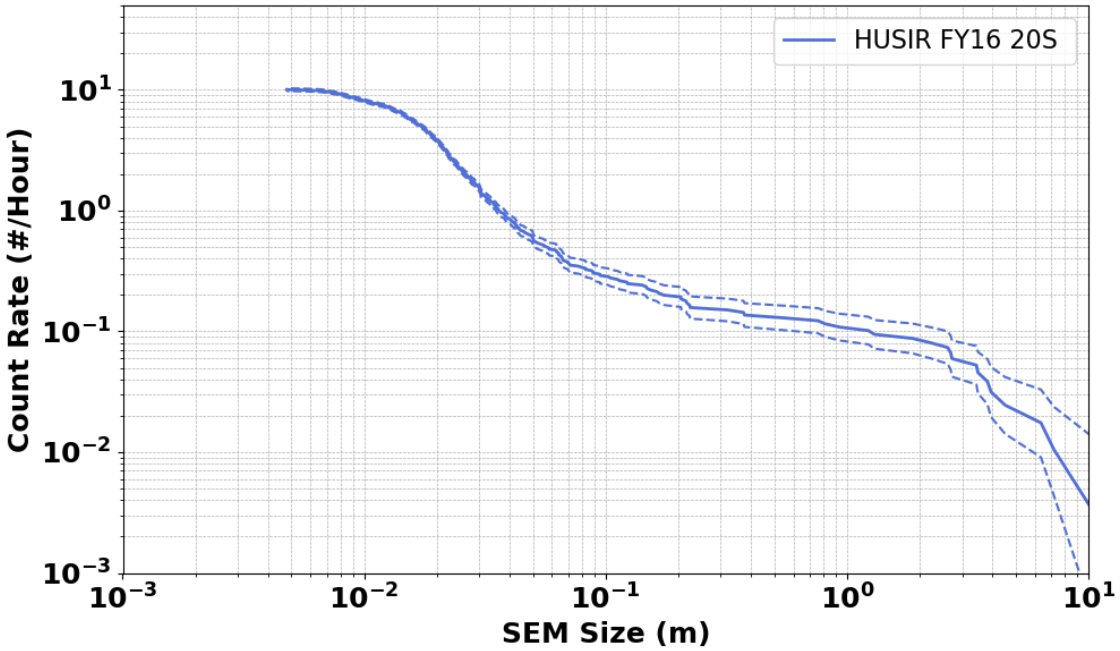

Figure E-8. Cumulative count rate versus SEM size, HUSIR 20° south, FY2016.

E.5. CUMULATIVE DETECTION RATE VERSUS PP SNR

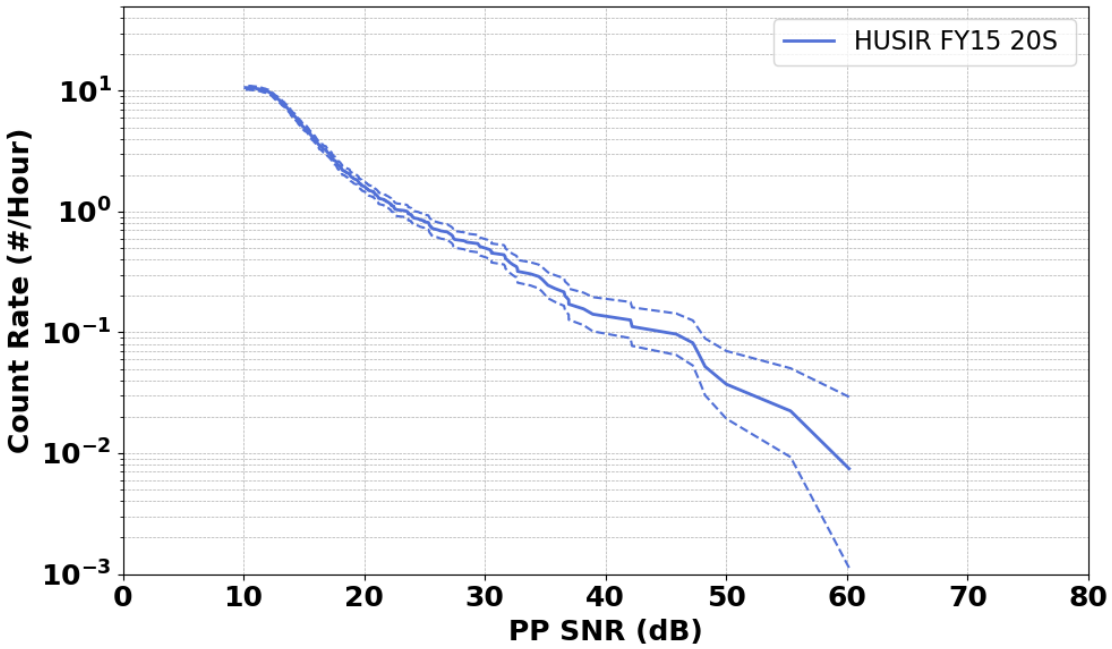

Figure E-9. Cumulative count rate versus detection SNR of the principle polarization, HUSIR 20° south, FY2015.

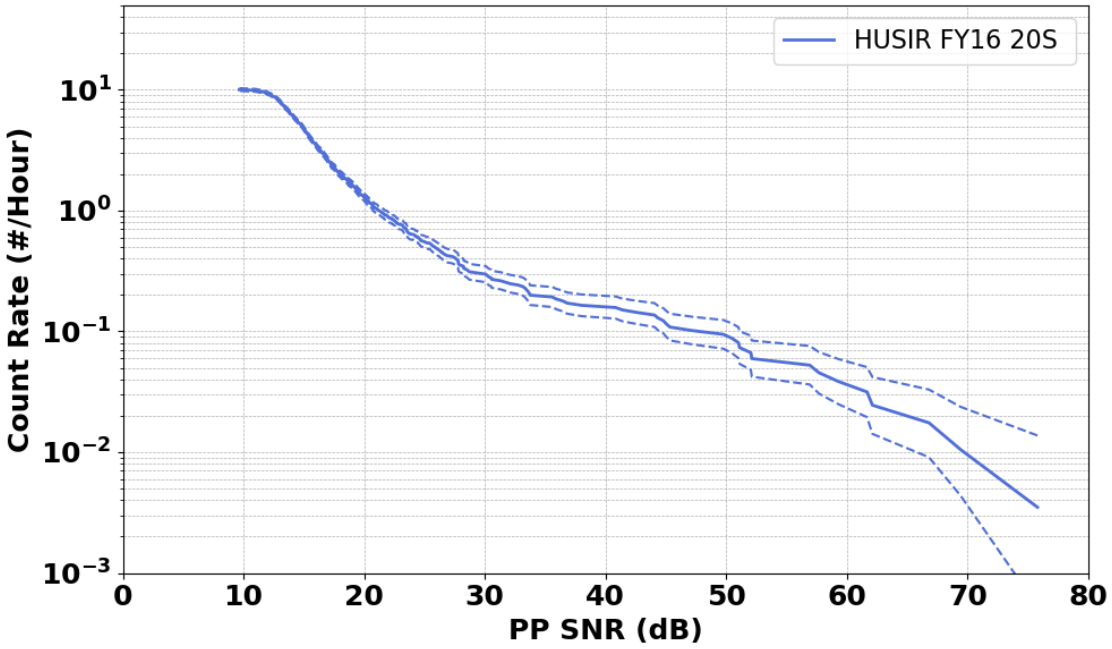

Figure E-10. Cumulative count rate versus detection SNR of the principle polarization, HUSIR 20° south, FY2016.

E.6. CUMULATIVE DETECTION RATE VERSUS RADAR CROSS SECTION

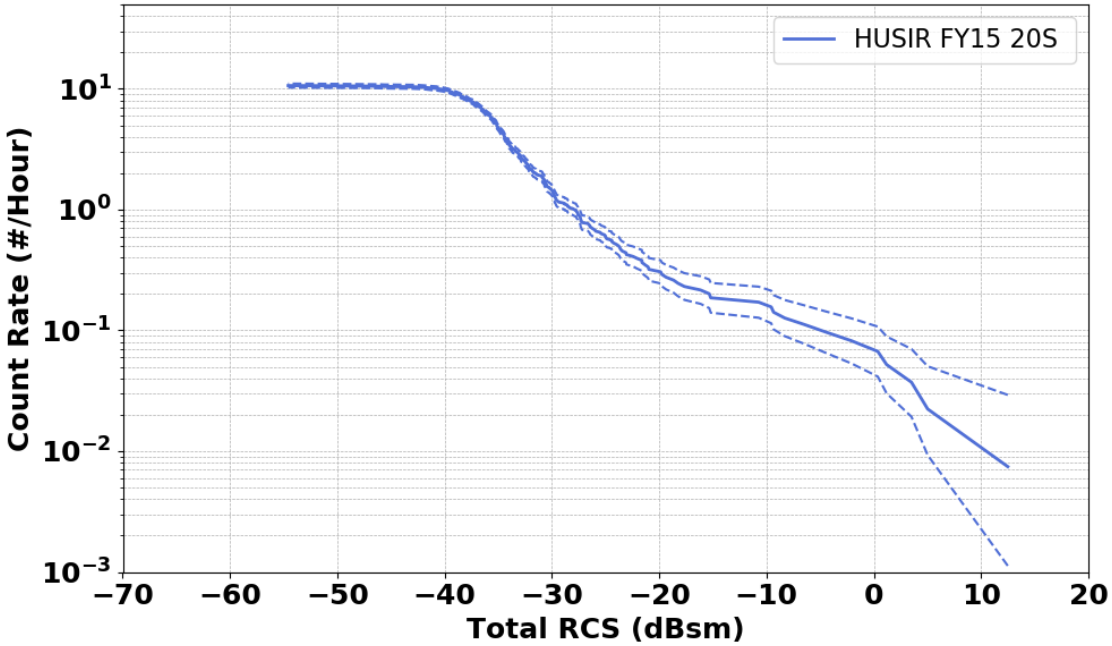

Figure E-11. Cumulative count rate versus Total Radar Cross Section, HUSIR 20° south, FY2015.

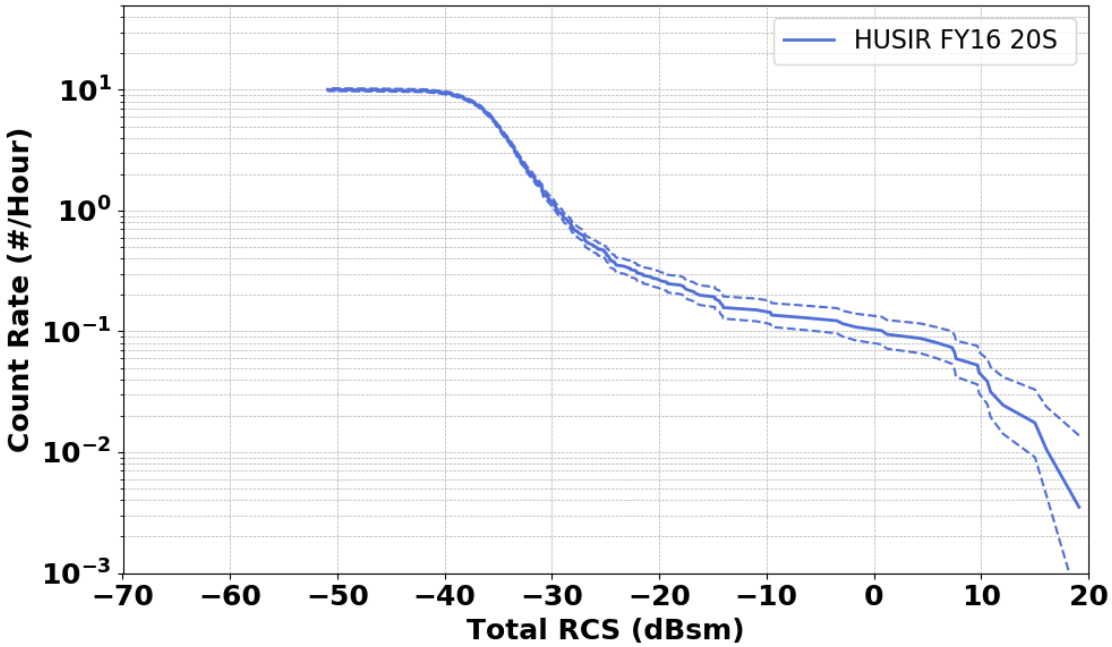

Figure E-12. Cumulative count rate versus Total Radar Cross Section, HUSIR 20° south, FY2016.

E.7. POLARIZATION RATIO DISTRIBUTION

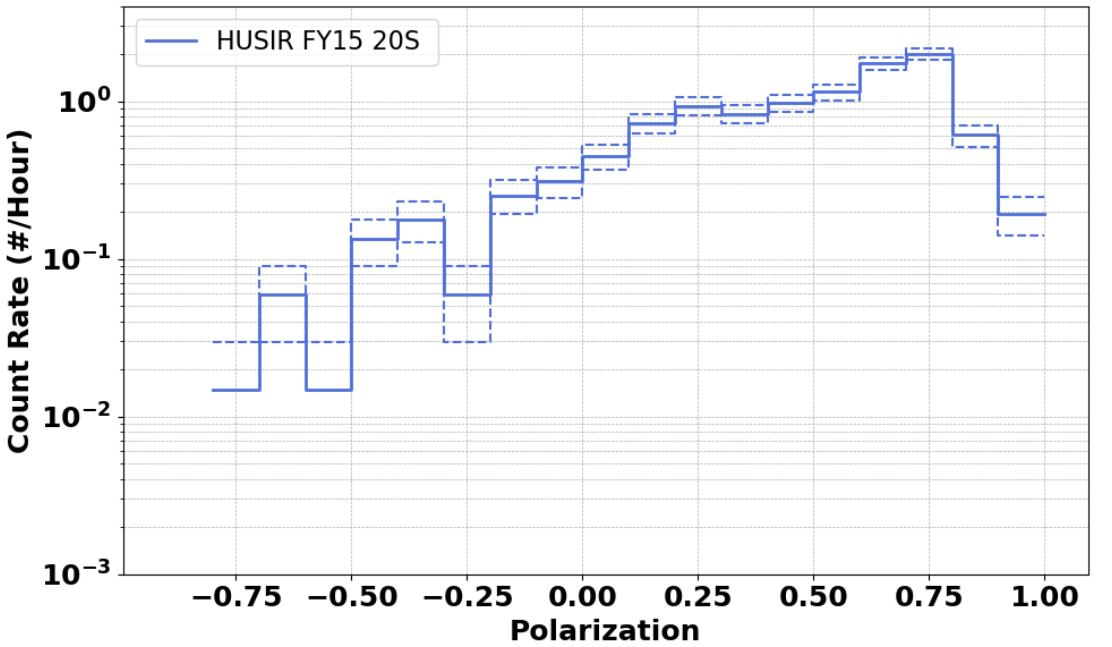

Figure E-13. Count Rate versus polarization ratio, HUSIR 20° south, FY2015.

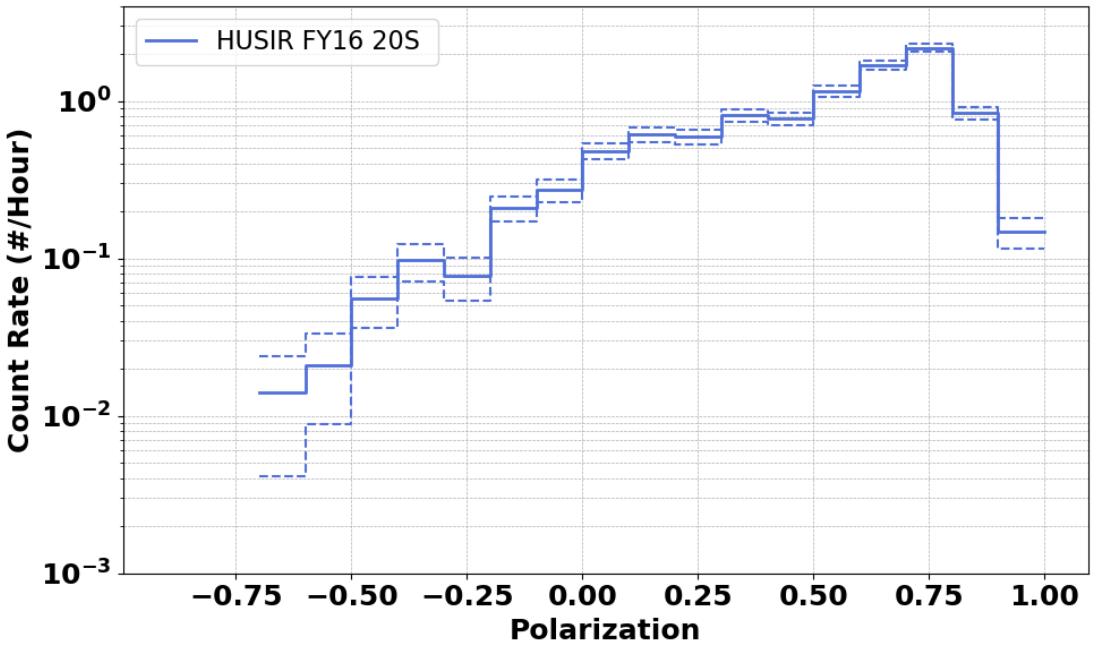

Figure E-14. Count Rate versus polarization ratio, HUSIR 20° south, FY2016.